10-16-2018

Numerical Study of Liquid Atomization and Breakup Using the Volume of Fluid Method in ANSYS Fluent

Sai Saran Kandati
Louisiana State University and Agricultural and Mechanical College

NUMERICAL STUDY OF LIQUID ATOMIZATION PROCESS USING THE VOLUME OF FLUID METHOD IN ANSYS FLUENT

A Thesis

Submitted to the Graduate Faculty of the
Louisiana State University and
Agricultural and Mechanical College
in partial fulfillment of the
requirements for the degree of
Master of Science

in

Mechanical and Industrial Engineering

by
Sai Saran Kandati
BSME, SSNCE, 2015
December 2018

Acknowledgments

Thanks to my thesis adviser, Dr. Dimitris E. Nikitopoulos for his guidance. Thanks to Mohan Durga Prasad for helping me to understand several concepts in my project. Thanks to Deekshith Mandala for helping me in editing my thesis. Thanks to my committee members, Dr. Keith A. Gonthier and Dr. Shengmin Guo, for taking the time to understand and evaluate my work. Thanks to my father Jayarami reddy kandati, my mother Smitha kandati and my sister Sahiti kandati for their support.

Portions of this research were conducted with high-performance computing resources provided by Louisiana State University (http://www.hpc.lsu.edu) and the Louisiana Optical Network Initiative (http://www.loni.org)

Table of Contents

Acknowledgments ….....ii

Nomenclature ….....v

Abstract ….....ix

Chapter
1 Introduction ….....1
1.1.Motivation.....1
1.2.Organization of thesis 2

2 Background and Literature review ….....3
2.1 Atomization of liquids 3
2.2. Types of atomization.....7
2.3. Literature review.....11

3 Mathematical Modeling..... 23
3.1 Conservation equations.....23
3.2. The Volume of Fluid (VOF) method.....26
3.3. Surface tension modeling (CSF model).....27
3.4. Turbulence modeling in multiphase flows.....29

4 Computational Model and Convergence.....41
4.1. Material properties.....41
4.2. Computational domains 42
4.3. Boundary conditions 44
4.4. Spatial discretization for molten slag material.....46
4.5. Settings and solvers.....47
4.6. Convergence study for different materials.....48
4.7. Spatial Convergence for molten slag system 48
4.8. Spatial Convergence study for the aqueous glycerol material.....50
4.9. Time Convergence for molten slag material.....52
4.10. Time Convergence for aqueous glycerol material 53
4.11. Residual Convergence for molten slag material 55
4.12. Residual Convergence study for the aqueous glycerol material.....56

5 Results and observations.....59
5.1. Procedure 59
5.2. Verification with numerical experiments.....63
5.3. Parametric analysis 65
5.4. Correlations.....96

6 Conclusions….....98

Appendix
A Validity of the choice and definition of non-dimensional numbers for the problem…...101

B Velocity distribution for different non-dimensional number combinations.....105

References…..... 108

Vita….....112

Nomenclature

Dimensional Variables

σ	Surface tension
σ_ω	Turbulent Prandtl number
θ	Angle
ρ	Density
ρ_g	Density of gas
ρ_l	Density of liquid
μ	Viscosity of liquid
μ_g	Viscosity of gas
μ_l	Viscosity of liquid
μ_t	Turbulent viscosity
τ	Kolmogorov time scale
τ_{ij}	Stress Tensor
ω	The angular velocity of the spinning disk
A_i	Interfacial area density
B	Damping factor
D	The diameter of the rotating electrode or spinning disk
d	Droplet diameter
d_l	The diameter of the liquid jet
d_p	Particle diameter
d_t	Circular diameter of the tube

d_{vs}	Mean volume surface diameter
D_w	Cross-diffusion term
D_w^+	The positive portion of the cross diffusional term
F_s	External body forces
$\bar{G}_k$	Turbulence kinetic energy generated due to velocity gradients
G_ω	Generation of w
g	Gravity
h	The thickness of the liquid film
I	Turbulent intensity
k	Turbulence kinetic energy
k’	The magnitude of surface tension force
l_n	Length scale
Δn	Grid size
l	Length of ligament
l’	Integral scale
$\vec{n}$	Unit normal vector
P_0	The pressure at free stream conditions
p	Pressure
Q	The volumetric flow rate of the melt
q_{max}	The exponential growth rate of the fastest growing disturbance
R	The radius of the rotating electrode or spinning disk
$R1, R2$	Principal curvature radii in the orthogonal directions
r	The Radius of the disk

r_c	Critical radius
S	Strain rate magnitude
t	Time
t_s	The thickness of the sheet at the breakup point
u	X-velocity component
$\vec{u}$	Velocity Vector
u_i	The separated equation of velocity
$\bar{u}_i$	Average component of velocity
u'_i	Fluctuating component of velocity
u_r	Radial velocity
u_t	Turbulent velocity
u_θ	Tangential velocity
u_{avg}	Mean velocity of the flow field
v	Y-velocity component
v’	The kinematic viscosity of the melt
w	The rate of dissipation of eddies
We	Weber number
x_i, x_j	Co-ordinates
Y_k	Dissipation due to turbulence
Y_ω	Dissipation of w
y_p	The distance between the cell centroids of grid and wall
z	Z-velocity component

Non-dimensional Variables

α	Volume fraction	
δ_{ij}	Kronecker delta	
d^*	Non-dimensional droplet diameter	$\frac{d}{D}$
d_{32}	Sauter mean diameter	
D_{32}^*	Non-dimensional Sauter mean diameter	d_{32}/D
Ek	Ekman number	$\frac{\mu_l}{\omega \rho_l D^2}$
F_1, F_2	Blending functions	
L^*	Non-Dimensional ligament length	$\frac{l}{D}$
Oh	Ohnesorge number	$\frac{\mu_l}{\sqrt{\rho_l \sigma D}}$
Re	Reynolds number	$\frac{Q}{\Pi \vartheta_l h}$
S_ω	User-defined source term	
u^+	Dimensionless velocity	
y^+	Dimensionless distance from the wall	

Abstract

The spherical metal particles produced from the centrifugal atomization process have been the topic of numerous theoretical, experimental and numerical studies from the past few years. This atomization process uses centrifugal force to break-up molten material into spherical droplets, which are quenched into solidified granules by the flow of cold air on the spherical droplets. In the present work, a transient three-dimensional multiphase CFD model is applied to three different materials: Molten slag, aqueous glycerol solution, and molten Ni-Nb to study the influence of the dimensionless parameters on the centrifugal atomization outcome.

Results from numerical experiments indicated that the droplet size, ligament length of a slag material increases with an increase in Ekman number while keeping the other two parameters effectively unaltered. The observed increase of the droplet size with increase in Ekman number is due to the decrease of applied atomization energy on the thin liquid film at the edge of the spinning disk. The droplet size, ligament length also increases by decreasing the Ohnesorge number due to a higher resistance offered by surface tension forces to the liquid disintegration process. The droplet size, ligament length values also increased as the Reynolds number was increased.

.

Chapter 1
Introduction

1.1. Motivation

Centrifugal atomization process involves complex multi-phase physics. A complete understanding of this complicated physics is required to explain the droplet breakup phenomenon in centrifugal atomization process. Detail study on the interfacial flow physics helps in identifying key parameters, which can determine the effect of centrifugal force on droplet formation mode and droplet size. The critical metrics that are in association with the atomization process are liquid Reynolds number, Ekman number, and Ohnesorge number.

Droplet breakup phenomenon in any atomization process is a complicated multi-parameter problem. The importance of understanding the ligament mode breakup process in several atomization techniques is becoming very important, especially in centrifugal atomization mechanism, which utilizes all the rotational work to directly break up the thin liquid film into spherical powder particles. Study of such complicated multi-phase flow near the rotating disk (wall) is very challenging. In this thesis, the Primary focal point is on understanding the effects of critical parameters on ligament mode breakup process for different materials in the centrifugal atomization process.

The best tool to simulate ligament mode breakup phenomenon is Computational Fluid Dynamics (CFD). Computational fluid dynamics can be used to capture several complex flow phenomena in the droplet breakup process. From literature is found that turbulence plays a vital role in the droplet breakup phenomenon, several turbulence-modeling approaches are used to include the effects of turbulence in the system of equations, and finally, parametric studies are performed using commercial computational fluid dynamics software called ANSYS-FLUENT to understand the impact of critical parameters on the atomization process.

1.2. Organization of thesis

Chapter 1 introduces the motivation for the research work.

Chapter 2 is devoted to the literature studies of theoretical, numerical and experimental findings related to thin film formation on spinning disk and droplet formation mechanism at the edge of the spinning disk.

Chapter 3 presents the continuity and momentum equations. This chapter also explains the Volume of Fluid method (VOF) and surface tension modeling method (CSF). Finally, this chapter closes by discussing the equations necessary to model turbulence effects in the multiphase environment.

Chapter 4 gives a complete description of a numerical model which includes a computational grid, the relevant boundary conditions, the solvers and settings, the temporal and spatial discretization schemes and the converge criteria.

Chapter 5 presents the results of the centrifugal atomization of different materials explored through various numerical algorithms.

Chapter 6 concludes the research work.

Chapter 2
Background and Literature Review

2.1 Atomization of Liquids

In many industrial applications such as metal powder manufacturing, combustion or spraying atomization of liquid is an important phenomenon. Several types of atomizing techniques were developed to satisfy various needs of industrial requirements.

In the centrifugal atomization process, the role of the atomizer is to break the thin film flowing on spinning disk into tiny droplets. To produce sprays with desired droplet sizes a complete understanding of liquid breakup process during atomization process is required. The atomization process of liquid films and jets are affected by several factors such as liquid properties, ambient conditions, and other operating parameters.

Generally, atomization processes are divided into two types depending upon different fragmentation mechanisms. The two types are the primary atomization and secondary atomization process. In the primary atomization process, the liquid is fragmented or disrupted into small structures due to the formation of instabilities. These instabilities are due to the action of cohesive and disruptive forces. Different types of primary atomization process are jet, sheet, film, prompt and discrete parcel. In secondary atomization process, the liquid is fragmented or disrupted into much smaller sized droplets due to the aerodynamic interactions between liquid droplets and ambient gas. An excellent example for secondary atomization process is discrete parcel atomization process.

In most of the industrial applications, primary and secondary atomization process is a consequence of the disturbance formation and disturbance breakdown on the liquid surface [1]. Disturbances are due to several reasons such as hydrodynamic instabilities, pressure fluctuations,

and wall effects. Disturbance formation process is always followed by the disturbance breakdown process, which occurs due to different actions such as instability, surface perforation, and stripping [1]. Depending upon the shape and geometric features of the bulk liquids, the liquid breakup process is classified into three types: liquid dripping, liquid jet breakup, and liquid sheet breakup.

2.1.1. Liquid dripping mechanism

This mechanism occurs widely in nature. The droplet formation mechanism occurs due to balance between gravitational force and surface tension force. The production of droplets happens when gravitational forces overcome the surface tension forces. Figure.2.illustrates the liquid dripping mechanism. The droplet diameter is shown in equation.2.1 [2]

$$D = \left(\frac{6d_t\sigma}{\rho_l g}\right)^{\frac{1}{3}} \tag{2.1}$$

Figure 2.1. Dripping mode droplet breakup process [2]

2.1.2. Liquid Jet breakup

In this process, the perturbations responsible for the disintegration of the liquid jet are due to the force balance between cohesive and disruptive forces. The length of the jet and size of the droplets are essential characteristics in jet disintegration process.

Many researchers studied the liquid jet disintegration process. Rayleigh [3] performed an extensive analysis on non-viscous liquid jet disintegration process. From his research, the author has concluded that the wavelengths of disturbances play an essential role in droplet breakup process. The exponential growth rate of the fastest growing disturbance (q_{max}) is expressed as follows

$$q_{max} = 0.97 * \left(\frac{\sigma}{\rho_l {d_l}^3}\right)^{0.5} \tag{2.2}$$

The optimum wavelength is described by

$$\lambda = 4.51 d_l \tag{2.3}$$

d_l is the diameter of the liquid jet.

Figure.2.2 shows the idealized Rayleigh jet droplet breakup process. Rayleigh studies neglect Turbulence and viscous effects.

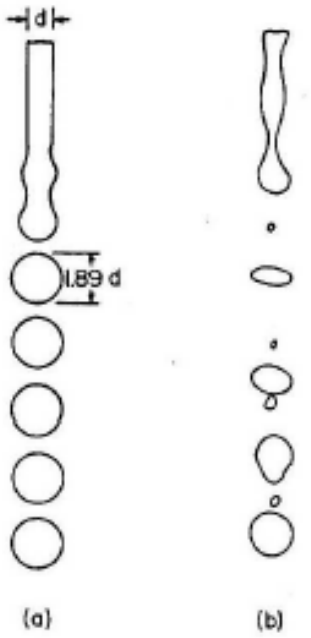

Figure 2.2. (a) Ideal jet breakup (b) actual breakup [4]

2.1.3. Liquid sheet breakup

Formation of thin flat liquid sheets is due to the impingement of liquid at the center of a rotating disk or cup. The disintegration of flat sheets depends on several factors such as liquid properties, ambient gas properties, and discharge velocity. Liquid ribbons are formed at the leading edge of the thin liquid sheet when the waves produced due to centrifugal force reaches critical amplitude [5]. Ultimately, these liquid ribbons contract into ligaments due to surface tension forces.

$$D_l = \left(\frac{2}{\pi}\lambda_{opt} w_s\right)^{0.5} \tag{2.4}$$

The resulting droplet size is given by

$$D = const\left(\lambda_{opt} t_s\right)^{0.5} \tag{2.5}$$

Where t_s is the thickness of the sheet at the breakup point.

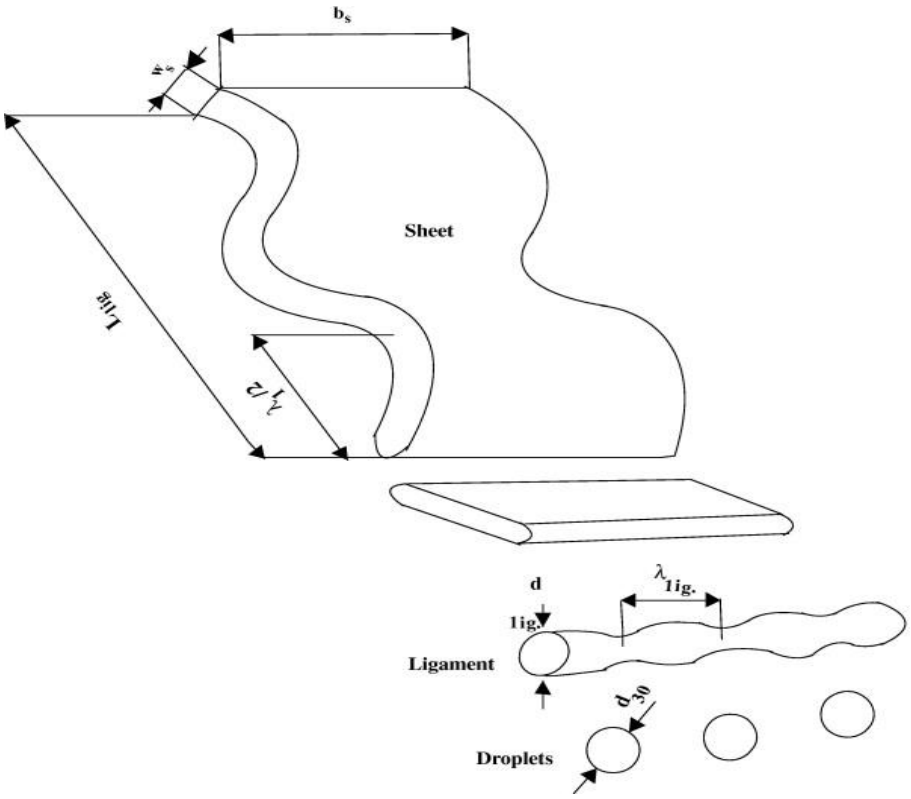

Figure 2.3. Sheet disintegration process [5]

2.2. Types of atomization

Various atomization devices with several capabilities are developed to transform thin liquid films into discreet droplets. Formation of Spray occurs when high-velocity liquid diskharges into slow moving gas or high-velocity gas discharge is on to slow moving liquid. Among all atomization, techniques gas atomization, water atomization and centrifugal atomization techniques are the most practical atomizers.

2.2.1. Gas atomization

In this atomization process, Formation of tiny particles is due to the interaction between the molten metal stream and a gas jet. The tiny spherical droplets produced due to these interactions are solidified during flight. Two types of gas atomization techniques exist: close couple gas atomization and free fall atomization [6].

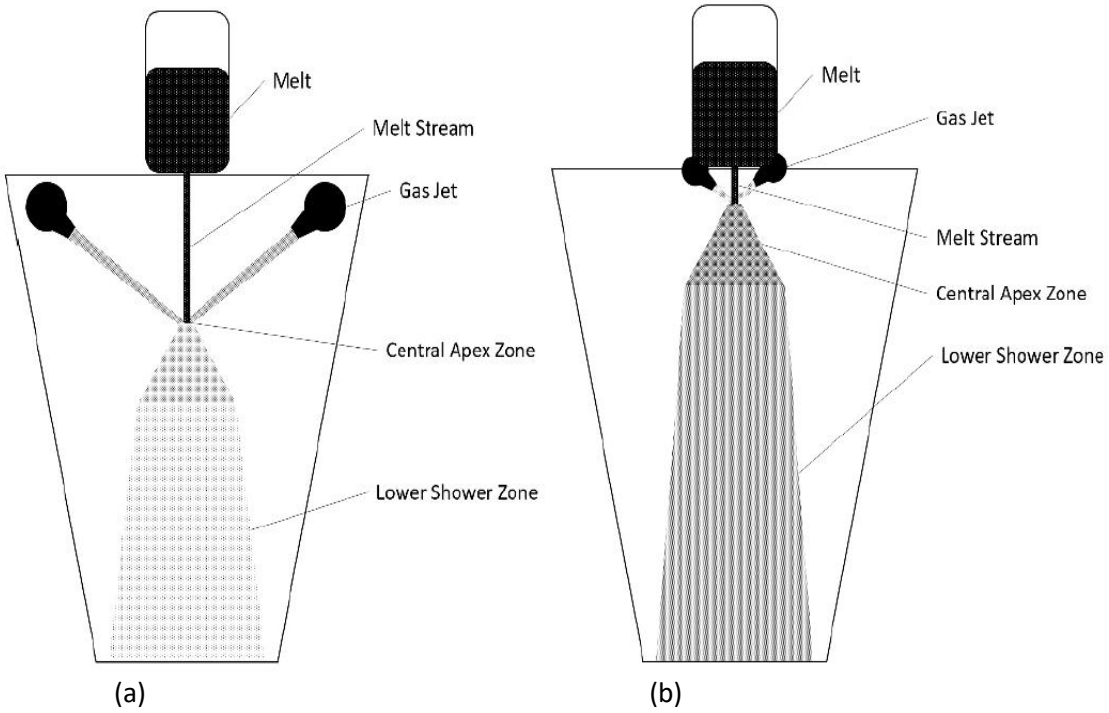

Figure 2.4. (a) Free fall gas atomization (b) Close-couple gas atomization [7]

In any atomization process, operating parameters play an important role in determining the size of solidified particles [8]. In the gas atomization process, the operating parameters to control the particle size in this process are metal feed rate, gas properties, melt properties and nozzle design.

2.2.2. Water atomization

It is commonly accepted and widely used atomization process. In this atomization process, the formation of tiny particles is due to the interactions between the molten metal stream and water jet [7]. The quality of the product is often affected by the oxidation and irregular shapes. Figure 2.5 shows a schematic representation of the water atomization.

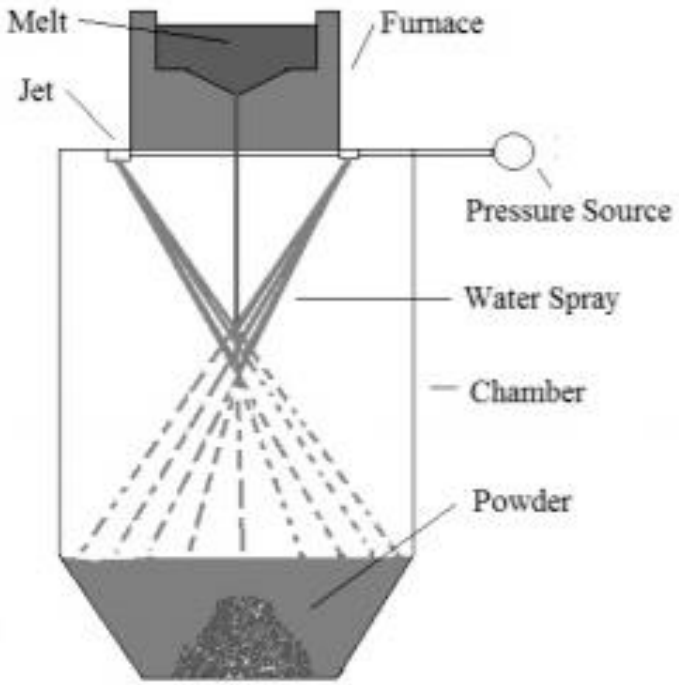

Figure 2.5. Water atomization process [7]

2.2.3. Centrifugal atomization

This atomization mechanism is commonly used to produce powders of alloys and refractory metals. This process will be covered in detail in this thesis. The detailed explanation of the centrifugal atomization mechanism gives the necessary background information to understand the physics of centrifugal atomization process.

In this atomization process, centrifugal forces are used to break up the thin molten film. The first type of atomization process based on centrifugal atomization technique is Rotating electrode process better known as REP process. In the REP process, a rotating spindle is used to spin consumable electrode at high speeds by fixing one of its ends to the rotating spindle, and a stationary tungsten electrode is used to melt the other end of the consumable electrode. In this process, the formation of tiny droplet particles occurs due to the action of surface tension and centrifugal forces [9]. Figure 2.6 gives a schematic representation of the REP process

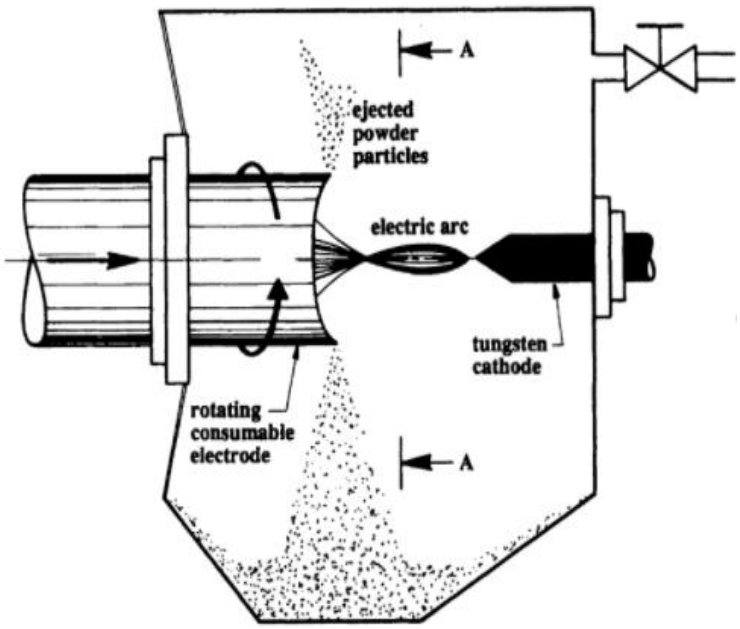

Figure 2.6. Schematic of rotating electrode atomization process [9]

Compared to gas and water atomization techniques, rotating electrode process produce a coarse particle size of 150 to 250 μm because of which this process is used to produce powders of refractory materials. The second type of atomization process based on centrifugal atomization technique is a spinning disk atomization process. Atomization of metallic melts using spinning disk finds extreme importance in many industrial applications. In this process, molten metal flows from a nozzle to the center of the spinning disk. Due to the action of large centrifugal forces, molten metal quickly moves to the edge of the rotating disk where the melt flies off the disk, and formation of tiny droplets occurs due to the interaction between the melt and ambient gas. Figure 2.7 shows a schematic representation of a spinning disk atomization process.

Figure 2.7. Schematic of spinning disk atomization [9]

2.3. Literature review

2.3.1. Theoretical and Numerical investigations of film thickness

Previous studies prove that the size of the metal powders or slag granules are affected by three mechanisms: thickness of the molten film formed on the spinning disk, Ligament or sheet formation mechanism at the edge of the disk and the droplet breakup process from sheet or ligaments. Literature also suggests that the performance of a centrifugal atomization process primarily depends on the thickness of the film formed at the edge of the disk [10]. Emslie et al. [11] performed extensive theoretical analysis on the equations describing fluid flow on a spinning disk to construct characteristic curves at consecutive times for any given initial fluid distribution. From their studies, the authors developed a correlation to determine the thickness of the liquid film on the spinning disk at a particular radius(R) by balancing viscous drag force with centrifugal force. The expression 2.6 gives the thickness of the film formed at a particular distance on a spinning disk.

$$h = \left(\frac{3Qv}{2\pi r^2 \omega^2}\right)^{\frac{1}{3}} \tag{2.6}$$

Where v is the kinematic viscosity of the melt, Q is the volumetric flow rate, r is the radius of the disk and ω is the angular velocity of the spinning disk.

Rauscher et al. [12] theoretically determined the thickness of the film at the edge of the spinning disk by neglecting Coriolis forces. Later on, Lepehin et al. [13] investigated the effects of Coriolis forces on the thickness of the film and equation 2.7 shows the correlation to determine the thickness of the film.

$$h = 0.886 Q^{0.348} v^{0.328} \omega^{-0.676} r^{-0.7} \tag{2.7}$$

Where v is the kinematic viscosity of the melt, Q is the volumetric flow rate, r is the radius of the disk and ω is the angular velocity of the spinning disk.

Zhao et al. [14] developed a numerical model to predict the thickness of the melt and the tangential and radial velocities of the melt on a rotating disk as a function of hydraulic jump location. The authors compared the obtained results with existing analytical solutions and had determined that the developed model give more accurate results than the previously existing analytical solutions. Equations 2.8 and 2.9 gives a representation of the correlations to determine the thickness of the film after the hydraulic jump

$$r < r_c; h = \frac{v}{0.4534205\omega} \frac{r_{in}}{r} \tag{2.8}$$

$$r > r_c; h = -\frac{1}{0.702} \sqrt{\frac{v}{\omega}} \ln\left(1 - \sqrt{\frac{0.702Q}{0.739\pi\sqrt{vQ}}} \frac{1}{r}\right) \tag{2.9}$$

Where

$$r_c = \sqrt{\frac{0.702Q}{0.739\pi\sqrt{vQ}}} \tag{2.10}$$

Where r_c is the critical radius where hydraulic jump occurs, ν is the kinematic viscosity of the melt, Q is the volumetric flow rate, r is the radius of the disk and ω is the angular velocity of the spinning disk.

Woods et al. [15] experimentally studied the presence of wavy regimes formed across the radius of the disk. Whereas, Burns et al. [16] found that the Nusselt theory model is not appropriate for sizeable inertial flow conditions.

Rice et al. [17] solved the Navier-stokes equation numerically to compute fluid flow characteristics on the rotating disk. The authors have used VOF, CSF methodologies and rectangular grid to predict the thickness of the film on a rotating disk. Pan et al. [18] have performed extensive two-dimensional numerical analysis using Ansys Fluent to determine the effects of operating parameters on the thickness of the film formed on the spinning disk. They assumed that the flow on the spinning disk is turbulent. Similar to Rice et al. [17], the authors used Volume of Fluid methodology (VOF) methods to model multiphase physics. From their studies, authors observed that surface tension has no effects on the thickness of the film and gave correlations to determine the thickness of the film on a spinning disk for several operating parameters.

Bhatelia et al. [19] conducted both 2D and 3D CFD analysis to determine the film thickness using the VOF approach. 3D simulation results were found to be in close agreement with the experimental results whereas 2D simulation results were found to underpredict the film thickness value by thirty-nine percent. The authors concluded that the assumption of laminar flow conditions on a spinning disk is the primary reason for the deviations.

2.3.2. Experimental investigation of droplet formation mechanism

Champagne and Angers [20] performed a centrifugal atomization process on various metals to identify various types of droplet formation mechanisms. In their study, they identified three different droplet formation mechanisms.

1. Direct droplet formation (DDF)
2. Ligament mode disintegration(LD)
3. Film disintegration(FD)

As mentioned earlier, researchers also observed that operating and material parameters control atomization mechanisms. Angular speed (ω), Diameter of the rotating electrode (D), the Volumetric flow rate of the melt (Q) are the operating parameters. Density (ρ), viscosity (μ) and surface tension (σ) of the melt are the material parameters. The authors determined that the ratio of operating and material parameters determines the molten melt disintegration mode. Equation 2.11 expresses the ratio.

$$\frac{Q\omega^{0.6}/D^{0.68}}{\sigma^{0.88}/\mu^{0.17}\rho^{0.71}} \tag{2.11}$$

Champagne and Angers determined that the change of mode from DDF to LD occur when the ratio is at 0.07 and from LD to FD when the ratio is at 1.33. Figure.2.8 gives a schematic representation of different types of drop formation mechanism.

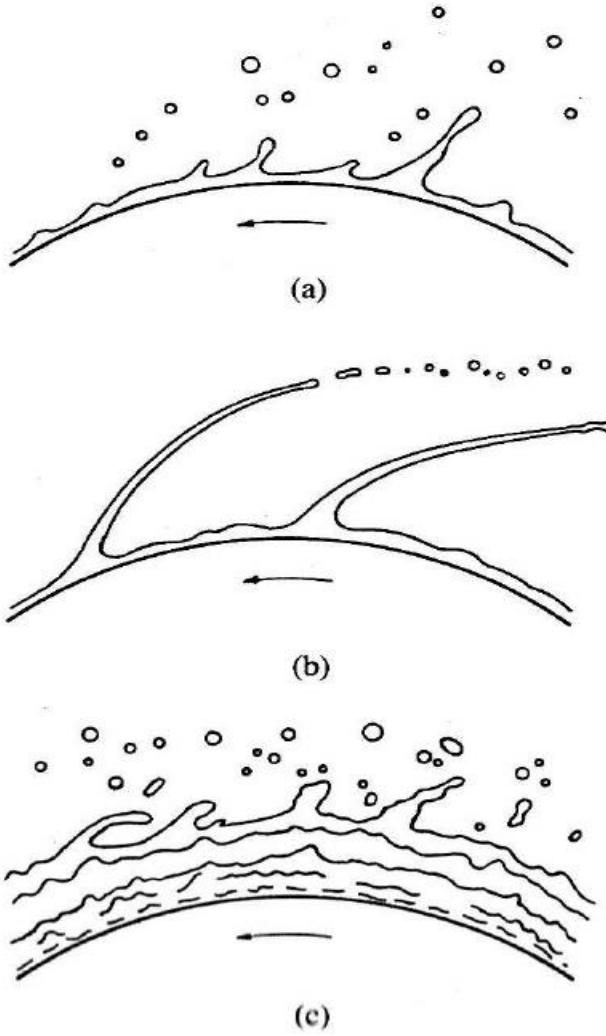

Figure 2.8. (a) Direct droplet regime (b) Ligament regime (c) Sheet regime [20]

The authors also developed a correlation to predict the mean volume surface diameter (d_{vs}). They also determined that the type of droplet formation mode has significant effects on shape, size and size distribution of droplets produced during centrifugal atomization process [21].

$$d_{vs} = \frac{\sigma^{0.43} Q^{0.12}}{\rho_l^{0.43} D^{0.64} \omega^{0.98}} (4.63 * 10^6) \tag{2.12}$$

Halada et al. [22] investigated the droplet formation mechanisms both theoretically and experimentally to develop centrifugal atomization (CA) diagram which represents the atomization

mode depending on the liquid and operating parameters. They gave a complicated relationship between the volumetric flow rate (Q), Weber number (We) and Reynolds number (Re) to predict the particle diameter (d_p).

$$We = \frac{\rho_l \omega^2 D^3}{\sigma} \tag{2.13}$$

$$Re = \frac{\rho_l \omega D^2}{\mu} \tag{2.14}$$

From their studies, authors also concluded that the liquid metal atomization was mainly occurring through DDF mechanism and they developed a correlation to predict the particle diameter (d_p) based on a theoretical calculation that neglects the effects of viscosity.

$$d_p = \frac{3.2R}{\sqrt{We}} \tag{2.15}$$

Hinze and Milborn [23] experimentally studied three different types of disintegration formation mechanisms occurring at the edge of the rotary cup to investigate the criteria for transition from one state to another state of droplet formation mode. From their studies, authors found that the transition from one state to another state occurs due to an increase in melt mass flow rate at a fixed angular speed. Researchers also developed correlations, which cover a wide range of operating conditions.

Criteria for the transition from ligament to direct droplet formation mode

$$\frac{Q}{D}\left(\frac{\rho_l}{\sigma D}\right)^{0.5}\left[D\left(\frac{\rho_l D}{\sigma}\right)^{0.5}\right]^{0.25}\left[\frac{\mu}{(\rho_l \sigma D)^{0.5}}\right]^{0.167} < 2.88 \times 10^{-3} \tag{2.16}$$

Criteria for the transition from sheet to ligament droplet formation mode

$$\frac{Q}{D}\left(\frac{\rho_l}{\sigma D}\right)^{0.5}\left[D\left(\frac{\rho_l D}{\sigma}\right)^{0.5}\right]^{0.6}\left[\frac{\mu}{(\rho_l \sigma D)^{0.5}}\right]^{0.167} < 0.442 \tag{2.17}$$

Most of the studies conducted by Hinze and Milborn focuses on droplet formation mechanism occurring at low volumetric flow rates. Fraster et al. [24] experimentally studied the factors influencing the liquid sheet dimensions during a spinning cup atomization process. The authors performed a photographic study and established two principal mechanisms of sheet disintegration. The first mechanism occurs at low tangential velocities and mass flow rates and the second mechanism occurs at high tangential velocities and mass flow rates. Kamiya and Kayano [25] performed numerous experiments to investigate the physics of film or sheet type disintegration mechanism on a rotating disk. The authors found that the operating parameters play an important role in determining the thickness of the film at the edge of the disk. Researchers also obtained a correlation determining the droplet diameter size in film type disintegration process.

$$\frac{d_{max}}{R} = 1.1We^{-0.3}\left(\frac{\rho_l Q^2}{\sigma R^3}\right)^{0.15}\left(\frac{Q}{\vartheta R}\right)^{-0.15} \tag{2.18}$$

2.3.3. Experimental and Numerical investigations of ligament mechanism

In this thesis, Ligament mode droplet formation mode is considered as the most appropriate atomization process. This mode of atomization can produce narrow ranges of droplet sizes than those obtained through sheet formation mode.

A.R. Frost [26] studied the physics of ligament mode droplet formation mechanism extensively through experiments to develop correlations to predict the first appearance of this mechanism. In his studies, the disk diameter was chosen between 40-120 mm, the depth of the disk edge was fixed to be around 1mm, and an electric motor was used to rotate the disk. Aqueous solutions of glycerol are used in these experiments to analyze the effects of critical parameters on the atomization process. The angular velocities of the Disk were in the range of 50-1000 rad/s. From his studies, the author found that molten metal flow rates play an important role in

determining the mode of the atomization mechanism. They also determined that the melt viscosity is less influential than the density or surface tension of the molten melts.

For direct drop formation mode

$$\frac{\left(\frac{Q\rho_l}{\mu D}\right)\left(\frac{\omega\rho_l D^2}{\mu}\right)^{0.95}}{\left(\frac{\sigma D\rho_l}{\mu^2}\right)} < 1.52 \tag{2.19}$$

For ligament mode droplet formation mode

$$\frac{\left(\frac{Q\rho_l}{\mu D}\right)\left(\frac{\omega\rho_l D^2}{\mu}\right)^{0.63}}{\left(\frac{\sigma D\rho_l}{\mu^2}\right)^{0.9}} > 0.46 \tag{2.20}$$

For the first appearance of sheet droplet formation mode

$$\frac{\left(\frac{Q\rho_l}{\mu D}\right)\left(\frac{\omega\rho_l D^2}{\mu}\right)^{0.84}}{\left(\frac{\sigma D\rho_l}{\mu^2}\right)^{0.9}} < 19.8 \tag{2.21}$$

Eisenklam [27] studied the instability responsible for the formation of ligaments for an inviscid fluid at the edge of the rotating disk or cup. From his research, the author has concluded that ligament mode disintegration happens due to the growth of waves in the melt. The author also derived a correlation to determine the wavelength of ligament based on the experimental values of Fraster et al. [24]. Kawase and De [28] performed centrifugal atomization experiments on Newtonian and Non-Newtonian fluids and determined correlations to predict the total number of ligaments formed during spinning disk atomization process.

Literature shows that the ligament mode droplet breakup process is similar to the liquid jet disintegration process. Ahmed et al. [29] [30] developed a two-dimensional computational model to study the effects of Weber number and Reynolds number on the breakup process of a viscous

liquid jet numerically. The authors used finite different schemes to solve the system of equations and performed numerical experiments by varying Reynolds and Weber numbers. The authors observed that the developed computational model underpredicts the droplet sizes at a relatively high Reynolds number of 1254 and overpredicts the drop sizes at a low Reynolds number of 587.

Wu et al. [31] and Lasheras et al. [32] numerically investigated the effects of turbulence on the breakup process of liquid jets. They found that liquid breakup process occurs due to the distortion of liquid at the air-liquid interface. The authors concluded that the distortion occurs due to the effects of air turbulence. Shinjo et al. [33] [34] performed computational fluid dynamic analysis to study different modes of ligament breakup process. They determined that the breakup of ligaments consist of two modes. The first mode is shortwave mode and the second mode is a longwave mode, which is also known as Rayleigh mode.

2.3.4. Computational methods for multiphase flows

Based on the spatial and temporal formulations the multi-phase flow problems are classified into two methods: Lagrangian method and Eulerian method [35]. In the Lagrangian method, the computational grid deforms at every time step to track the motion of the interface between two phases. This method requires significant computational resources for simulations, and they are also not preferred in flow fields containing large gradients. In the Eulerian method, single continuous equations are solved to capture the multiphase physics. Requirement of Computational efforts decreases significantly in this method, and generally, in the flow fields with large gradients, Eulerian method is preferred [36].

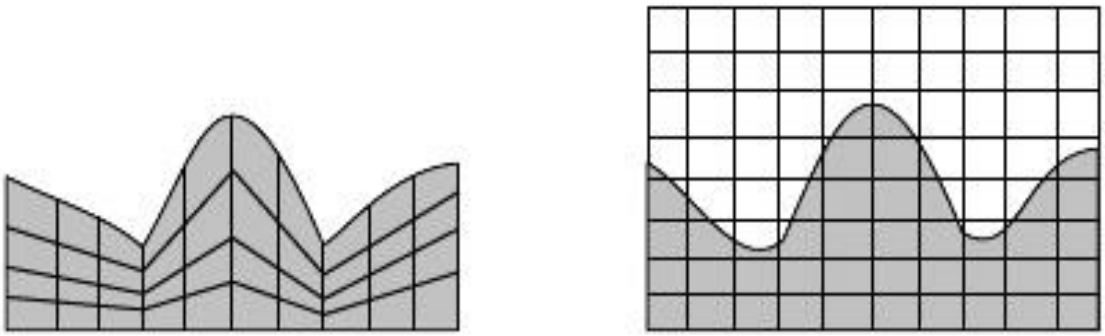

(a) (b)

Figure 2.9. (a) Lagrangian method (b) Eulerain method [36]

In Eulerian methodology, three different types of interface capturing schemes are used to model multiphase physics. They are Marker and cell (MAC) method; Level set method (LS) and the volume of fluid method (VOF). In MAC method, the interface physics is captured by capturing the movement of particles from one cell to other cells. These Lagrangian particles stores the coordinate values in every time step [37]. This method is usually not implemented in droplet breakup studies due to high numerical instabilities associated with the scheme.

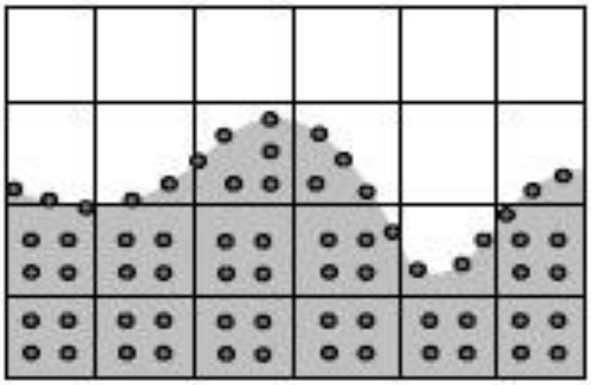

Figure 2.10. MAC method [37]

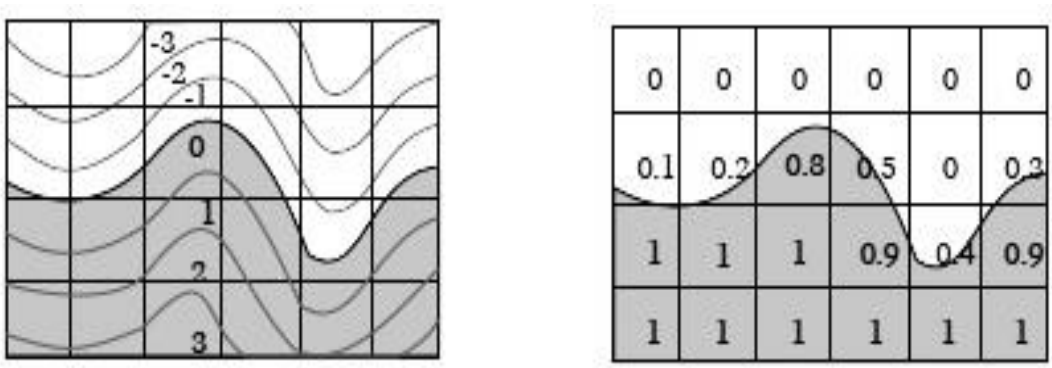

(a) (b)

Figure 2.11. (a) Level set method (b) Volume of Fluid method [40, 41]

Osher and Fedkiw [38] developed the level set method to track the interface between two phases. In this method, a scalar transport equation is solved to capture the movement of the interface. This method introduces a signed distance function into the system of equations. The sign of the function varies as a function of the location of the interface. It is zero at the interface and takes negative and positive values on either side of the interface. Ghost cells are used to describe multiple fluids in the computational domain to satisfy mass balance [39]. Accurate definition of ghost cells is complicated in this method.

The VOF is a commonly used interface-capturing model that was initially developed by Hirt and Nichols [40]. A color function known as volume fraction is used in this method to capture interface. Usually, the sum of volume fractions will be unity. Several interface capturing and tracing schemes are developed using VOF methods to compute local curvatures accurately [41] [42]. Volume of Fluid methods provides accurate mass conservation.

The surface tension force is a balance of pressure forces and attractive molecular forces. Three standard models are used to implement surface tension forces: Continuum surface force model (CSF), Continuum surface stress model (CSS) and ghost fluid method [42]. It is challenging to implement surface tension forces in finite volume methods (FVM). Brackbill [43] has successfully implemented the surface tension effects at the interface between two fluids by

coupling CSF with VOF method. The following chapter describes different mathematical models used in this thesis.

Chapter 3
Mathematical Modeling

Various mathematical models are used to perform numerical analysis of droplet breakup phenomenon in centrifugal atomization process. In this chapter, a complete description of the two-equation turbulence model is made to explain the physical meaning of different turbulent quantities. This chapter also describes the two-phase laminar interface capturing technique along with mass and momentum conservation equations. Eventually, surface tension force modeling using CSF method, turbulence modeling using RANS method and different wall treatment methods are described meticulously to close the chapter.

3.1 Conservation equations

In two-phase flows, a moving interface between the phases is used to separate the computational domain into two separate regions. Several interface capturing and tracking schemes are implemented to determine the location of the moving interface. In this thesis, Interface capturing methods are used to capture the complicated interface between two phases. In this method, for each phase, a single set of governing equations is solved, and surface tension force is acting at the interface is introduced as a source term into the governing equations where the fluid dynamic behavior of two phases depends on the local instantaneous variables such as velocity, pressure.

In the present work, both fluids are considered incompressible and immiscible, and SST k-w model is used to include the effect of turbulence into the system of equations. As a result, two additional scalar quantities turbulent kinetic energy (k) and specific dissipation rate (ω) are added to the system of equations. Volume of fluid methodology (VOF) is employed to solve a single set

of governing equations for individual phases. An overview of conservation equations used in this thesis is explained in the following sub chapters.

3.1.1. Mass conservation equations

Equation 3.1 expresses the mass conservation condition for a control volume dV in a fixed space with the difference between incoming and outgoing mass flow rate at every time interval

$$\frac{\partial \rho}{\partial t} + \frac{\partial (\rho u_i)}{\partial x_i} = 0 \tag{3.1}$$

The leftmost term in the above equation is a representation of the temporal variation of density in a control volume. The next term is the representation of net mass stream through the faces of the control volume. In multiphase flows, the density and viscosity of different phases are evaluated using volume fraction parameter.

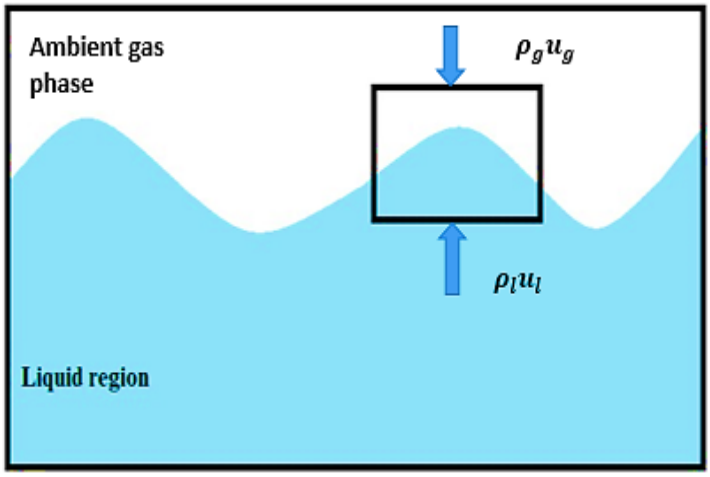

Figure 3.1. Schematic representation of mass conservation

3.1.2. Momentum conservation equations

In two-phase flows, the inertial and viscous forces of both phases must be considered to determine the evolution of interface. Apart from the above forces, surface tension force should also be considered to determine the interface shape.

The temporal variation of momentum in a control volume dV is equivalent to the sum of volume and surface strengths acting in that control volume. The momentum equation is shown in Equation 3.2.

$$\frac{\partial \rho u_i}{\partial t} + \frac{\partial (\rho u_i u_j)}{\partial x_j} = -\frac{\partial p}{\partial x_i} + \frac{\partial \tau_{ij}}{\partial x_j} + F_s \tag{3.2}$$

Where

$$\tau_{ij} = \mu(\frac{\partial u_i}{\partial x_j} + \frac{\partial u_j}{\partial x_i})$$

The leftmost term in equation (3.2) depicts the temporal variation of the velocity and the second term on the left-hand side of the equation represents force flux over a fixed control volume. The right-hand side of the equation indicates the total forces acting on a fluid element where the first term on the right-hand side represents the pressure force term, and the next term beside the first term indicates the effect of viscous forces on faces of a fixed control volume. Gravitational force is neglected due to the presence of significant centrifugal force. The last term represents external forces acting on a fluid element such as surface tension force, and the CSF model is used to include these forces in the system of equations [43].

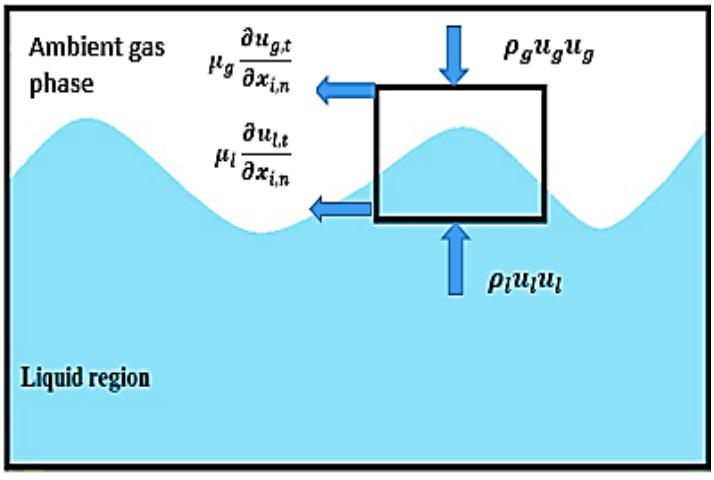

Figure 3.2. Schematic representation of momentum conservation

3.2. The Volume of Fluid (VOF) method

In the VOF method, interfaces are tracked using a color function know as volume fraction 'α'. The volume fraction values are used to determine the fractions of the computational cell occupied by liquid or gaseous phase. The values of 'α' are dependent on the grid size and distribution of phases. Volume fraction value has no physical significance. It is just a scalar variable that is used to determine the location of the interface between two fluids [43].

In this methodology, a cell is considered to be completely occupied by the liquid when the volume fraction value is $\alpha_l = 0$. And the same cell is considered to be completely filled with ambient gas when the volume fraction value is given as $\alpha_g = 1$[45]. The mesh should be very fine at the interface between two phases to avoid false diffusion.

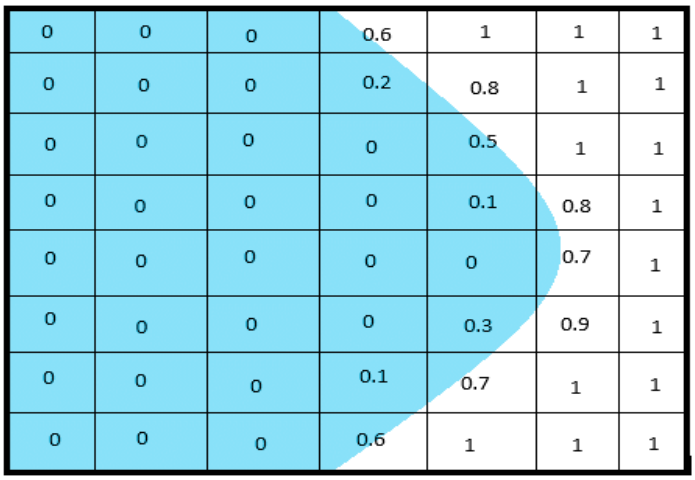

Figure 3.3. Schematic representation of volume fractions

The Equation 3.3 gives the time evolution of the volume fraction equation.

$$\frac{\partial \alpha}{\partial t} + \nabla.(\alpha \vec{u}) = 0 \tag{3.3}$$

Volume weighted sum of density and viscosity that depends on volume fraction values is used to determine the values of the properties appearing in transport equations. Equations 3.4 and 3.5 are used to calculate the physical properties in the computational domain.

$$\rho = \alpha_g \rho_g + (1 - \alpha_g)\, \rho_l \tag{3.4}$$

$$\mu = \alpha_g \mu_g + (1 - \alpha_g)\, \mu_l \tag{3.5}$$

The generalized expression to determine the properties in the computational domain is calculated by Equation 3.6.

$$\varphi = \alpha_g \varphi_g + (1 - \alpha_g)\, \varphi_l \tag{3.6}$$

The interfaces between two fluids are determined using geometric reconstruction scheme. In this scheme, a straight line in each computational cell approximates the interface between two fluids. In multiphase flow simulations, the possibility to produce false diffusion is evident. A monotonic advection scheme is used to avoid the production of false diffusion across interfaces in geometric reconstruction scheme [45].

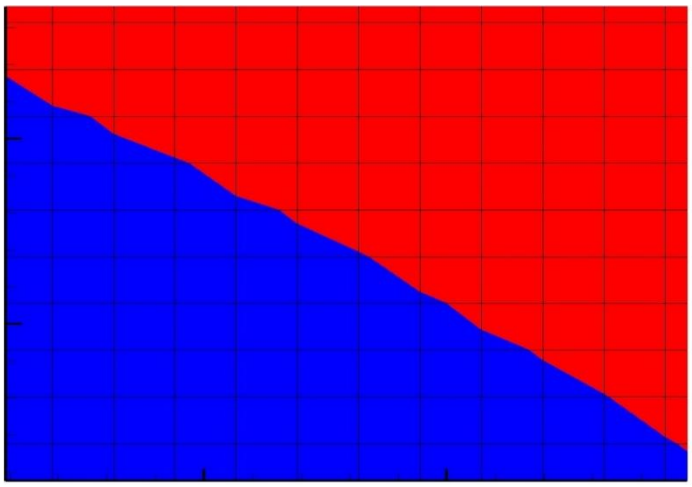

Figure 3.4. Interface capturing using the PLIC approach

Geometric reconstruction scheme reduces the numerical diffusion. The velocity is expressed as the weighted average of the velocity between different phases and is given by

$$u = \alpha_g u_g + (1 - \alpha_g)\, u_l \tag{3.7}$$

3.3. Surface tension modeling (CSF model)

In multiphase flows, the surface tension effects at the interface between two phases are due to attractive forces between the molecules of liquid and gaseous elements. The surface pressure

constraint that acts to minimize the interfacial area influences the interface shape significantly. The forces exerted by the surface tension at the interface tend to balance the pressure difference across the fluids, and their effects must be taken into account in the momentum equations [44].

Brackbill [43] proposed a continuum surface force (CSF) model to overcome the diskontinuous pressure distribution at the interface. In this method, Additional volumetric source term is introduced into the momentum equation to account for surface tension effects. Interface curvature (k) determines the magnitude of the surface tension force and it is given by Equation 3.8.

$$k' = \frac{1}{R1} + \frac{1}{R2} \tag{3.8}$$

Equation 3.9 gives interface curvature in divergence form.

$$k' = \nabla . \frac{\nabla \alpha}{|\nabla \alpha|} \tag{3.9}$$

R1 and R2 represent the principal curvature radii in the orthogonal directions and the normal vector determines the direction of the surface tension force on the interface. Volume fraction values determined the unit normal vector on the interface and are given by

$$\vec{n} = \frac{\nabla \alpha}{|\nabla \alpha|} \tag{3.10}$$

The volume fraction gradient has values only in the interfacial region.

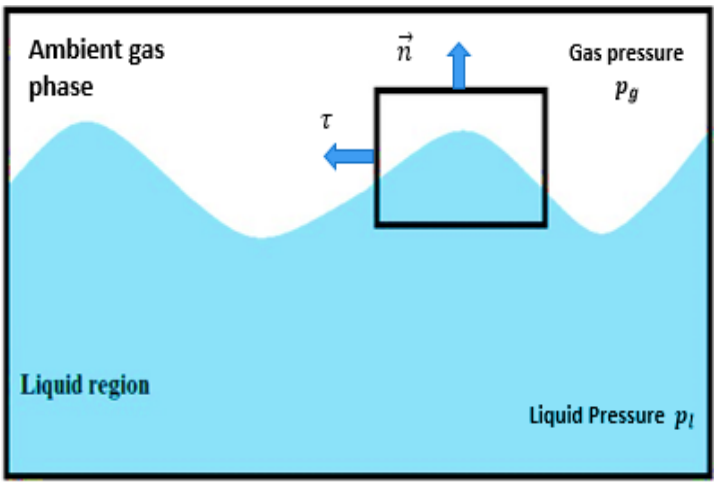

Figure 3.5. Schematic representation of surface forces at the interface

In all the simulations, the surface tension coefficient is considered to be constant and does not vary with temperature. The effect of surface tension forces is considered by adding surface tension force as an additional source term to the momentum equation. The source term is shown in equation 3.11[43].

$$F_s = \sigma k' \vec{n} \tag{3.11}$$

Where, F_s can be represented as

$$F_s = \sigma \nabla . \frac{\nabla \alpha}{|\nabla \alpha|} \frac{\nabla \alpha}{|\nabla \alpha|}$$

$$F_s = \sigma \left(\nabla . \frac{\nabla \alpha}{|\nabla \alpha|} \right) \nabla \alpha$$

3.4. Turbulence modeling in multiphase flows

At the edge of a rotating disk, turbulence effects play a significant role in effecting the mass and momentum equations significantly. At a large Reynolds number, fluctuating liquid and gas phase velocities governs the turbulence. It is very challenging to model turbulence effects in multiphase flow due to complicated interface involved. In this thesis, two equation turbulence models are used to model complex turbulent effects.

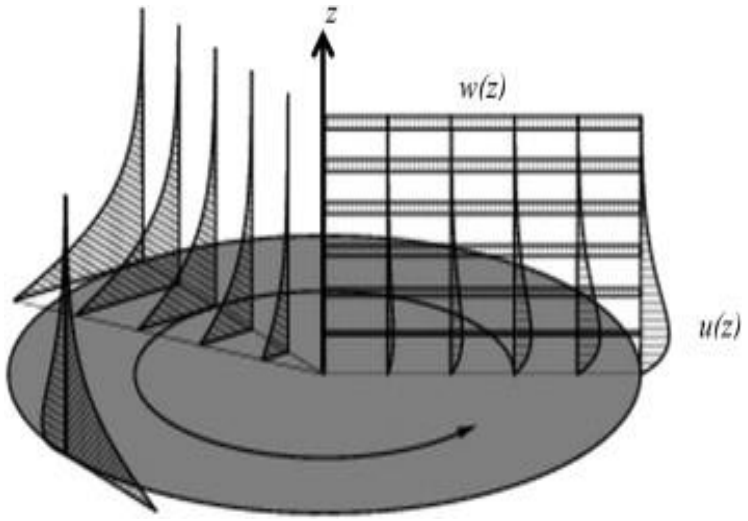

Figure 3.6. Schematic representation of velocity profiles on spinning disk [46]

Figure 3.6 shows the velocity profiles on the spinning disk. Generally, the flow becomes unstable when the inertial forces are much larger than the viscous forces. Velocity unsteadiness and arbitrariness are the characteristics of turbulence in multiphase flows. Fluctuating eddies causes flow property variations in the flow field, and the kinetic energy produced can transfer from the most considerable eddy to the smallest eddy due to the interactions between several eddies. These eddies should be modeled accurately in order to resolve multi-phase physics in spinning disk application. Usually, eddies will have different orders of magnitude. Kolmogorov length scale determines the smallest eddies at a particular length scale. This length scale (l_n) can be determined by using kinematic viscosity and turbulent kinetic energy dissipation rate.

$$l_n = \left(\frac{v^3}{\varepsilon}\right)^{\frac{1}{4}} \tag{3.12}$$

The Kolmogorov time scale is given by

$$\tau = \left(\frac{v}{\varepsilon}\right)^{\frac{1}{2}} \tag{3.13}$$

Kolmogorov time and length scales must be resolved to capture accurate turbulent flow physics in Direct Numerical Simulation (DNS). Equation 3.14 can be used to determine the total number of mesh points required to resolve Kolmogorov scales [47]

$$N = \frac{l}{l_n} \tag{3.14}$$

Where l is the integral scale and in the three-dimensional case, the equation 3.15 is used to determine the total number of grid points required to resolve Kolmogorov scales.

$$N = \frac{l}{l_n}^3 = Re^{\frac{9}{4}} \tag{3.15}$$

From the equation 3.15, it is found that the total number of grid points required to solve three-dimensional turbulent multiphase flow problems is very high for a high Reynolds number flows. Using direct numerical simulation approach will dramatically increase the computational costs. Other models that are available to model turbulence are RANS and LES models. In the LES approach, kinetic energy transported by large eddies are resolved explicitly [48] and kinetic energy transported by smaller eddies are modeled using the sub-grid scale method (SGS). One critical set back of this methodology is that the geometric reconstruction scheme cannot be coupled with the LES model in ANSYS Fluent [45]. In RANS turbulence models, two equation eddy viscosity models were used to determine the Reynolds stress terms in the momentum equation. The details of the RANS model is discussed in the following section.

3.4.1. RANS (Reynolds-averaged equations)

In this approach, flow quantities such as velocity, pressure can be separated into two components: average component and fluctuating component. The methodology to separate the fluctuating component from the system of governing equations is known as Reynolds averaging [49]. Equation 3.16 shows the general form of splitting expression.

$$\varphi_i = \bar{\varphi}_i + \varphi'_i \tag{3.16}$$

For example, equation 3.17 represents the separated equation of velocity

$$u_i = \bar{u}_i + u'_i \tag{3.17}$$

$\bar{u}_i$. u'_i are the average and fluctuating components of velocities.

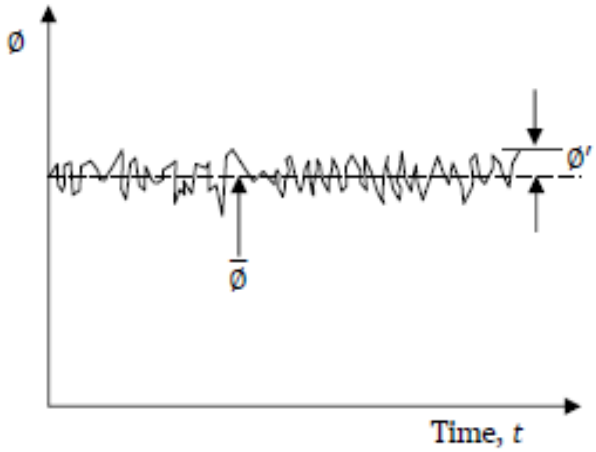

Figure 3.7. Propagation of statistically averaged fluctuating velocity with time [45]

RANS modeling produces time-averaged mass and momentum equations for incompressible flows. The Reynolds averaged mass and momentum equation are shown in equations 3.18, 3.19[45].

$$\frac{\partial \rho}{\partial t} + \frac{\partial (\rho \bar{u}_i)}{\partial x_i} = 0 \tag{3.18}$$

$$\frac{\partial \rho \bar{u}_i}{\partial t} + \frac{\partial (\rho \bar{u}_i \bar{u}_j)}{\partial x_j} = -\frac{\partial \bar{p}}{\partial x_i} + \frac{\partial}{\partial x_j}\mu\left(\frac{\partial \bar{u}_i}{\partial x_j} + \frac{\partial \bar{u}_j}{\partial x_i}\right) - \rho\overline{u'_i u'_j} + F_s \tag{3.19}$$

Due to the implementation of an averaging procedure to the Navier-stoke equations, an additional unknown term known as Reynolds stress term arises in the momentum equation. The Reynolds stresses are usually modeled using Boussinesq assumption. In this assumption, Reynolds stresses are determined by multiplying the turbulent viscosity with the velocity gradients and the contribution term is found by the equation 3.20.

$$-\rho\overline{u_i'u_j'} = \mu_t\left(\frac{\partial u_i}{\partial x_j}+\frac{\partial u_j}{\partial x_i}\right)-\frac{2}{3}\rho k\delta_{ij} \tag{3.20}$$

Where, μ_t is called as turbulent viscosity. It can also be called as eddy viscosity. k is the turbulence kinetic energy and δ_{ij} is kronecker delta.

The introduction of eddy viscosity into the system of equations changes the expression of momentum equations and is shown by equation 3.21.

$$\frac{\partial\rho\overline{u_i}}{\partial t}+\frac{\partial(\rho\overline{u_i}\overline{u_j})}{\partial x_j} = -\frac{\partial}{\partial x_i}\left(\bar{p}+\frac{2}{3}\rho k\right)+\frac{\partial}{\partial x_j}\left((\bar{\mu}+\bar{\mu_t})\left(\frac{\partial\overline{u_i}}{\partial x_j}+\frac{\partial\overline{u_j}}{\partial x_i}\right)\right)+F_s \tag{3.21}$$

Where,

$(\bar{\mu}+\bar{\mu_t})$ is the effective eddy viscosity.

Turbulent viscosity μ_t cannot be determined directly [45]. In turbulence models, Approximations are made to determine unknowns in terms of known quantities that are derived from empirical and semi empirical correlations. Literature [45] indicates that there exists zero, one, and two equation turbulence models. In each turbulence model, it is assumed that the turbulence is isotropic. One-equation models as if the Spalart-Allmaras model uses a transport variable similar to turbulent kinematic viscosity to determine the eddy viscosity of the flow. Most popular and accurate turbulent model in RANS is two-equation models and in this thesis, SST k-w model is used because of its ability to blend the formulation of the k-w model in the near wall region and k-ϵ model in the regions away from walls [47].

3.4.2. RANS SST K-w model

The SST k-w model is a two-equation turbulence model that has equations for turbulent kinetic energy and rate of dissipation of eddies [45]. Equation 3.22 shows the equation that should be solved to determine turbulent kinetic energy.

$$\frac{\partial(\rho k)}{\partial t} + \frac{\partial(\rho \bar{u_i} k)}{\partial x_i} = \frac{\partial}{\partial x_j}\left((\mu + \frac{\mu_t}{\sigma_k})\frac{\partial k}{\partial x_j}\right) + G_k - Y_k + S_k \quad (3.22)$$

The left-hand side of the equation represents the rate of change of turbulent kinetic energy and the convective transport of the generated turbulent kinetic energy. The first term on the right-hand side of the equation determines the effective diffusivity of the generated kinetic energy in the flow field. Turbulence kinetic energy generated due to velocity gradients is represented by $\bar{G}_k$. The dissipation due to turbulence is expressed as Y_k. Detailed explanation about $\bar{G}_k$ and Y_k is described in the following sub chapter. Specific dissipation rate in the turbulence model is the second transport equation that is to be solved to describe turbulence length scales [47]. The transport equation is expressed as following

$$\frac{\partial(\rho w)}{\partial t} + \frac{\partial(\rho \bar{u_i} w)}{\partial x_i} = \frac{\partial}{\partial x_j}\left((\mu + \frac{\mu_t}{\sigma_w})\frac{\partial w}{\partial x_j}\right) + G_w - Y_w + D_w + S_w \quad (3.23)$$

Once the length scales were determined, the turbulent viscosity is determined by applying the following expression [45]

$$\mu_t = \frac{\rho k}{w}\frac{1}{max\left(\frac{1}{\alpha^*}, \frac{SF_2}{a_1 w}\right)} \quad (3.24)$$

Here strain rate magnitude is expressed as S.

3.4.3. Modeling the turbulence production G_k and turbulence dissipation G_w

$\bar{G}_k$ and G_w express the production of turbulence kinetic energy and turbulence dissipation in the flow field. Where $\bar{G}_k$ is given by [45]

$$\bar{G}_k = minimum(G_k, 10\rho\beta^* kw)$$

G_k can be expressed as below using turbulence production equation (k)

$$G_k = -\rho\overline{u'_i u'_j}\frac{\partial u_j}{\partial x_i} \quad (3.25)$$

G_k can also be expressed as below using Boussinesq hypothesis

$$G_k = \mu_t S^2 \tag{3.26}$$

Equation 3.26 shows the strain tensor modulus S

$$S = \sqrt{2S_{ij}S_{ij}} \tag{3.27}$$

Production of w (G_w) is represented by the following equation

$$G_w = \frac{\alpha'}{v_t} G_k \tag{3.28}$$

Where the coefficient α' is given by

$$\alpha' = \frac{\alpha_\infty}{\alpha^*}\left(\frac{\alpha_0 + \frac{Re_t}{R_w}}{1 + \frac{Re_t}{R_w}}\right)$$

The coefficient of α^* in the above equations is expressed as

$$\alpha^* = \alpha_\infty^*\left(\frac{\alpha_0^* + \frac{Re_t}{R_k}}{1 + \frac{Re_t}{R_k}}\right)$$

Where,

$Re_t = \frac{\rho k}{\mu w}; R_k = 6; \alpha_0^* = \frac{\beta_i}{3}; \beta_i = 0.072; \alpha_\infty^* = 1; R_w = 2.95;\ \alpha_0 = \frac{1}{9}; \alpha_\infty = 0.52$

The formulation of dissipation production term in SST k-w models is different from the standard k-w model. A constant value of 0.52 is used in a standard k-w model whereas in SST k-w models blending functions $F_1$and F_2 were used to determine the value of α_∞. The function that is used to calculate (α_∞) is expressed as following

$$\alpha_\infty = F_1\alpha_{\infty,1} + (1 - F_1)\alpha_{\infty,2} \tag{3.29}$$

Where,

$$\alpha_{\infty,1} = \frac{\beta_{i,1}}{\beta_{\infty}^{*}} - \frac{\varrho^2}{\sigma_{w,1}\sqrt{\beta_{\infty}^{*}}}$$

$$\alpha_{\infty,2} = \frac{\beta_{i,2}}{\beta_{\infty}^{*}} - \frac{\varrho^2}{\sigma_{w,2}\sqrt{\beta_{\infty}^{*}}}$$

Where, $\varrho = 0.41$.

The First blending function that is used to determine (α_{∞}) is expressed as below

$$F_1 = \tanh(\varphi_1^4) \tag{3.30}$$

Where,

$$\varphi_1 = \min\left(\max\left(\frac{\sqrt{k}}{0.09wy'}, \frac{500\mu}{\rho y'^2 w}\right), \frac{4\rho k}{\sigma_{w,2} D_w^{+} y'^2}\right)$$

$$D_w^{+} = \max\left(2\rho \frac{1}{\sigma_{w,2}} \frac{1}{w} \frac{\partial k}{\partial x_j} \frac{\partial w}{\partial x_j}, 10^{-10}\right)$$

The second blending function used to determine (α_{∞}) is expressed as below

$$F_2 = \tanh(\varphi_2^4)$$

Where,

$$\varphi_2 = \max\left(\frac{\sqrt{k}}{0.09wy'}, \frac{500\mu}{\rho y'^2 w}\right)$$

In the above set of equations, y' represents the distance from the first surface to the next. Cross-diffusion term contains both a positive and negative portion where D_w^{+} represents only the positive portion. In the above equations the, constants are determined to be [45]

$\sigma_{k,1} = 1.176$; $\sigma_{w,1} = 2$; $\sigma_{k,2} = 1$; $\sigma_{w,2} = 1.168$; $a_1 = 0.31$; $\beta_{i,1} = 0.075$ and

$\beta_{i,2} = 0.0828$; $\beta_{\infty}^{*} = 0.09$

3.4.4. Modeling the turbulence kinetic energy dissipation

The turbulent kinetic energy dissipation in a flow field is given by Y_k. The following expression is used to determine the dissipation of turbulent kinetic energy [45].

$$Y_k = \rho\beta^* kw \tag{3.31}$$

Where,

$$\beta^* = \beta_i^*(1 + \zeta^* F(M_t))$$

$$\beta_i^* = \beta_\infty^* \left(\frac{0.2666 + \left(\frac{Re_t}{R_\beta}\right)^4}{1 + \left(\frac{Re_t}{R_\beta}\right)^4} \right)$$

$\zeta^* = 1.5$; R_β=8; β_∞^*=0.09; $Re_t = \frac{\rho k}{\mu w}$

In incompressible flow, the compressibility correction factor $F(M_t)$ becomes zero and the resultant equation for β^* is expressed as following

$$\beta^* = \beta_i^* \tag{3.32}$$

The dissipation of w is represented by Y_w. The expression used to determine dissipation of w is given by

$$Y_w = \rho\beta w^2 \tag{3.33}$$

Where blending function described in equation (3.34) is used to determine the values of β_i [45].

$$\beta_i = F_1\beta_{i,1} + (1 - F_1)\beta_{i,2} \tag{3.34}$$

Where, $\beta_{i,1} = 0.075$; $\beta_{i,2} = 0.0828$ and in incompressible flow, the term $F(M_t)$ is zero. And the resultant equation is expressed as $\beta = \beta_i$

3.4.5. Modeling of cross-diffusion term

To blend standard k-w model and standard k-ϵ model, a source term is added to the dissipation equation. This source term is known as a cross-diffusion term [45].

$$D_w = 2(1 - F_1)\rho\sigma_{w,2}\frac{1}{w}\frac{\partial k}{\partial x_j}\frac{\partial w}{\partial x_j} \tag{3.35}$$

3.4.6. Turbulence damping Source term to the w equation

Turbulence damping source term is added to the w equation to model free surface flows with high gradients in flow quantities accurately [45]. Large turbulence effects generated in the flow field due to high velocity gradients should be damped in order to model two phase flows accurately [45]. Equation 3.36 shows the source term added to the equation

$$S_w = A_i \Delta n \beta \rho_i \left(\frac{B6\mu_i}{\beta \rho_i \Delta n^2} \right)^2 \tag{3.36}$$

In the above equation, Interfacial area density is represented by A_i. Δn is the grid size and it represents the normal length of a cell to the interface. B is the damping factor which is fixed to be 10 for all the simulations and the value of β = 0.075.

3.4.7. Near-wall modeling in turbulent flows

In multiphase turbulence flows, the regions near the walls must be adequately resolved to capture accurate physics. In the turbulent boundary layer near the wall, there exist different layers in the inner region of the boundary layer. These layers are the viscous sublayer, the buffer layer, and the turbulent layer. These regions depend on the dimensionless velocity u^+ and dimensionless distance y^+. Dimensionless distance y^+ is calculated using the following expression.

$$y^+ = \frac{\rho u_t y_p}{\mu} \tag{3.37}$$

y_p – Distance between the center points of the grid to the wall.

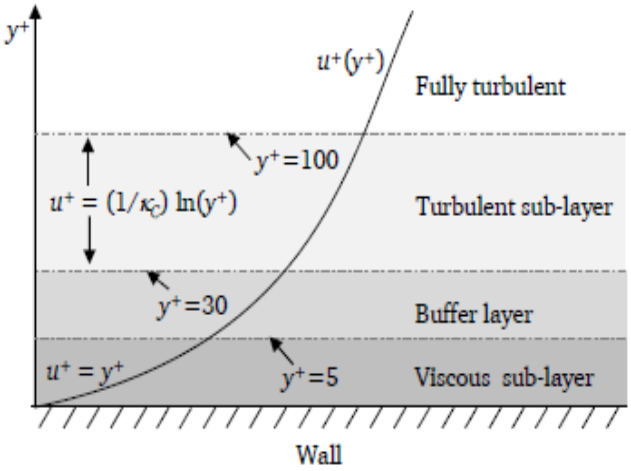

Figure 3.8. Schematic representation of the inner region of a turbulent boundary layer [45]

As shown in Figure 3.8, it can be determined that the region above the wall where $0 < y^+ < 5$ is considered to be in a viscous sub-layer region where viscous forces dominates the inertial forces. There exists a linear relationship between velocity distributions and wall distance [45].

$$u^+ = y^+$$

The region $5 < y^+ < 30$ is known as buffer layer region. It exists between the turbulent sub-layer and viscous sub-layer. In this layer, the viscous forces are cancelled out by turbulent stress values.

The region $y^+ > 30$ is known as a turbulent sub-layer region. In this region inertial forces dominates viscous forces. Logarithmic law is used to determine the dimensionless velocity distribution [50].

$$u^+(y^+) = \frac{1}{k_c}\ln(y^+) + C^+ \tag{3.38}$$

Where, $C^+ = 5$ and $k_c = 0.42$

In turbulent numerical simulations there exist two approaches to model the regions near the wall. One of them is enhanced wall treatment approach; This method combines a two-layer

model with enhanced wall functions to resolve viscosity affected regions which include viscous sub-layer. In this method, large numbers of grid points are required to resolve laminar sub-layer. In another approach, viscous sub-layer is related to the bulk region using semi-empirical correlations. In this thesis, the k-w SST model with enhanced wall treatment is used to solve all simulations.

Chapter 4
Computational Model and Convergence

Accuracy and convergence are essential aspects in the numerical solutions of fluid flow problems. The primary source of errors that affects the accuracy of numerical simulations is discretization and physical modeling errors. The discretization error arises due to the difference between a numerical solution and exact solution of the modeled equations whereas the physical modeling error arises due to oversimplification of existing models. In this chapter, the finite volume discretization method, interpolation schemes, material properties, and appropriate boundary conditions are described. Finally, a detailed discussion is made on Time, Iterative and grid convergence studies.

4.1. Material properties

As mentioned earlier, convergence studies play an essential role in identifying and determining the effects of errors on numerical simulations. The two materials used in performing convergence studies are a molten slag [51] and an aqueous glycerol solution. Table.4.1 shows the properties of different materials.

Table.4.1. Material properties

Case	**Material**	$\boldsymbol{\rho(\frac{kg}{m^3})}$	$\boldsymbol{\mu(Pa.s)}$	$\boldsymbol{\sigma(\frac{N}{m})}$
Case1	Molten slag	2612	0.125	0.538
Case2	Aqueous-glycerol solution	1170	0.0175	0.073

4.1.1. Non-Dimensional analysis and parameters

In the centrifugal atomization process, it is essential to study the effects of material and operating parameters on transition and atomization phenomenon. Previous studies have

determined all those quantities, which have a significant effect on the centrifugal atomization process [26].

$$F(\omega, D, Q, \mu, \sigma, \rho) = 0 \tag{4.1}$$

Depending on the number of quantities and fundamental dimensions involved, these parameters are classified into three groups. Three quantities are selected to make the groups independent of each other, and they are ω, Q and σ [26]. Three non-dimensional groups are obtained by combining the dependent parameters with the independent quantities. In addition, the following expressions could be written to express non-dimensional quantities.

$$F\left(\frac{\omega\rho D^2}{\mu}, \frac{\sigma D\rho}{\mu^2}, \frac{Q}{\pi\vartheta h}\right) = 0 \tag{4.2}$$

Other critical non-dimensional parameters are Length of the ligament$L^* = \frac{l}{D}$; and droplet diameter $D^* = \frac{d}{D}$ where D is the disk diameter. The operating conditions for the simulations in non-dimensional form are shown in Table.4.2

Table.4.2. Non-dimensional input parameters for convergence studies

Material	**Ek**	**Oh**	**Re**
Molten Slag	7.83e-05	0.0143	458
Aqueous glycerol solution	2.72e-05	0.0085	1312

4.2. Computational domains

4.2.1. Computational domain for molten slag material

General assumptions are made to perform numerical simulations to capture the droplet breakup phenomenon in centrifugal atomization process. Molten slag is assumed to flow continuously with a constant volume flow rate at the edge of the rotating disk. The production of molten metal occurs along the axis of disk edge, and rotational periodic boundary conditions are

applicable in the tangential direction. As shown in Figure 4.1 the computational domain only includes region near the edge of the spinning disk [51].

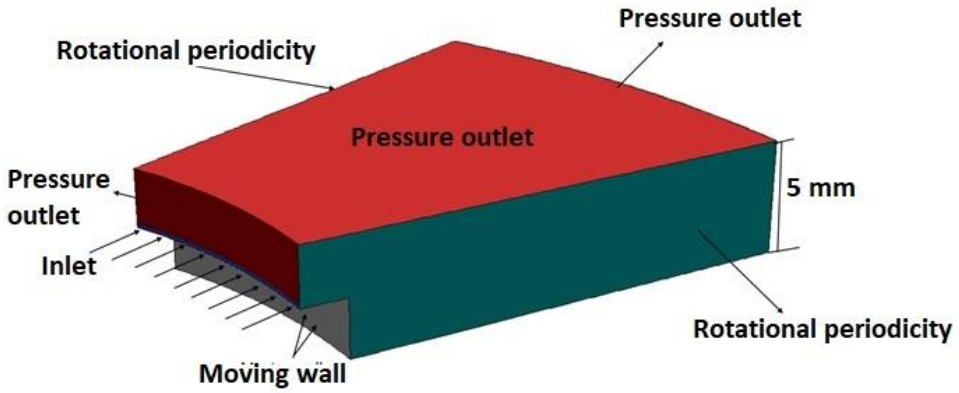

Figure 4.1. Computational domain with relevant boundary conditions for molten slag material (all units in mm) [51]

4.2.2. Computational domain for aqueous glycerol solution

For the given operating conditions, the liquid film thickness formed on the spinning disk is much smaller for aqueous glycerol solution when compared to molten slag material. Therefore, the computational domain is re-designed to capture the atomization process of an aqueous glycerol solution. Figure 4.2 shows the computational domain with re-designed dimensions for aqueous glycerol solution.

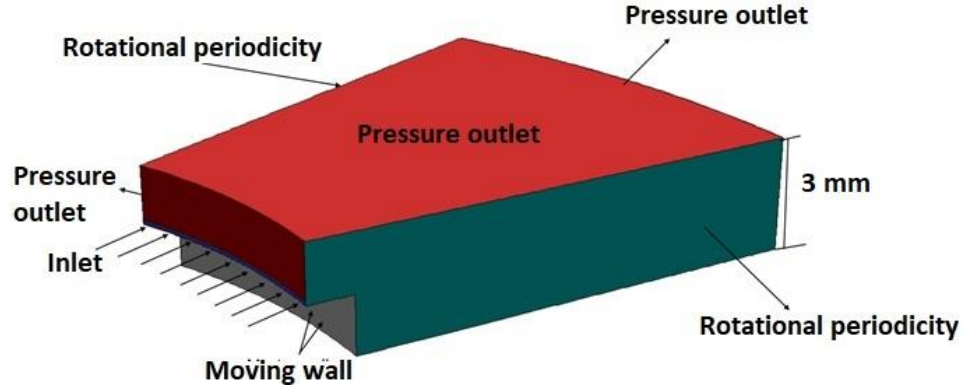

Figure 4.2. Computational domain with relevant boundary conditions for aqueous glycerol material (all units in mm) [51]

4.3. Boundary conditions

In any numerical simulation, boundary conditions play a significant role in simplifying the system of governing equations. Following sub-sections gives a brief discussion about different boundary conditions used in the atomization process.

4.3.1. Velocity Inlet

For both cases, same boundary conditions are used to perform numerical experiments. Dirichlet boundary conditions are applicable at the inlet, and the velocities in x, y, and z-direction of the Cartesian frame of coordinates is given by equations 4.3, 4.4 and 4.5.

$$u = u_r cos\theta - u_\theta sin\theta \tag{4.3}$$

$$v = u_r sin\theta + u_\theta cos\theta \tag{4.4}$$

$$z = 0 \tag{4.5}$$

Where the thickness of the liquid film at a particular radius along with radial and tangential velocities are expressed using the following relations [51]

$$u_r = C_2 e^{\zeta z}\cos(\zeta z) - C_1 e^{\zeta z}\sin(\zeta z) - C_4 e^{-\zeta z}\cos(\zeta z) + C_3 e^{-\zeta z}\sin(\zeta z)$$

Where, C_1, C_2, C_3, C_4 are constants and are represented as belows

$$C_1 = \frac{1}{2}\omega r e^{-\zeta h}\frac{2e^{\zeta h}cos(\zeta h)^2 - e^{\zeta h} + e^{-\zeta h}}{4\cos(\zeta h)^2 + e^{2\zeta h} - 2 + e^{-2\zeta h}}$$

$$C_2 = C_4 = \frac{\omega r cos(\zeta h)\sin(\zeta h)}{4\cos(\zeta h)^2 + e^{2\zeta h} - 2 + e^{-2\zeta h}}$$

$$C_3 = \frac{1}{2}\omega r e^{\zeta h}\frac{2e^{-\zeta h}cos(\zeta h)^2 - e^{-\zeta h} + e^{\zeta h}}{4\cos(\zeta h)^2 + e^{2\zeta h} - 2 + e^{-2\zeta h}}$$

$$\zeta = \sqrt{\frac{\omega}{\vartheta}}$$

$$r = \sqrt{x^2 + y^2}$$

$$\theta = \tan^{-1}\left(\frac{y}{x}\right)$$

$$r = -\frac{1}{2\zeta Q}\pi\omega\frac{4e^{2\zeta h}\cos(\zeta h)\sin(\zeta h) - e^{4\zeta h} + 1}{4e^{2\zeta h}\cos(\zeta h^2) + e^{4\zeta h} - 2e^{2\zeta h} + 1}^{-0.5} \quad (4.6)$$

$$u_\theta = \omega * r \quad (4.7)$$

u_r- Radial velocity of liquid at the edge of the spinning disk

u_θ − Tangential velocity at the edge of the spinning disk

In turbulence modeling, turbulent intensity and turbulent viscosity ratio at the inlet describes turbulence transport quantities such as turbulent kinetic energy and turbulent dissipation rate. The following expression gives approximate values for kinetic energy and dissipation rate from the turbulent intensity and turbulent viscosity ratio [45].

$$k = \frac{3}{2}\left(u_{avg}I\right)^2 \quad (4.8)$$

u_{avg} − Mean velocity of the flow field.

$$\omega = \rho\frac{k}{\mu}\left(\frac{\mu_t}{\mu}\right)^{-1} \quad (4.9)$$

I- Turbulent Intensity; $\frac{\mu_t}{\mu}$ – Turbulent viscosity ratio

4.3.2. Solid wall

Moving solid walls have no-slip boundary conditions.

$$u_r = 0; u_\theta = \omega r; u_z = 0 \quad (4.10)$$

4.3.3. Outlet boundary conditions

Pressure outlet boundary conditions are imposed to represent free stream conditions at remaining computational boundary faces.

$$p = P_0 \quad (4.11)$$

4.3.4. Rotational Periodic boundary conditions

Rotational periodic boundary conditions are applied on the two faces in theta direction to perform numerical simulations with less computational effort. In tangential direction (θ) the computational domain covers the formation of at least two to three ligaments. The angle θ is determined by performing a vast number of numerical simulations. By conducting analysis on a vast number of results, it is determined to use 24 degrees for molten slag material and 20 degrees for aqueous glycerol solution.

4.3.5. Initial conditions

At time t =zero, the values of different variables like u,k,ω should be provided at all computational cells to perform numerical simulations. At t=zero, A thin liquid film of thickness (h) is patched at the top of the spinning disk.

4.4 Spatial discretization for molten slag material

At high Reynold number values, the thickness of the molten metal film formed at the edge of the spinning disk will be very thin. In order to capture the physics of centrifugal atomization process accurately, the mesh needs to be fine enough near the thin film formed at the edge of the spinning disk. The developed mesh consists of hexahedral elements with sides of 1e-04 in X and Y directions and with sides of 0.5e-04 in the z-direction. Hexahedral cells are more accurate than tetrahedral elements for calculating the surface tension in ANSYS FLUENT. Adaptive mesh refinement method is avoided to eliminate spatial discretization errors

4.4.1. Spatial discretization of aqueous glycerol solution

For the aqueous glycerol solution, the thickness of the liquid film formed at the disk edge will be minimal. To capture the atomization process, the developed mesh should have a large number of grid points in order to solve the problem accurately. Similar to the previous case, the

developed mesh consists of hexahedral elements with sides of 6e-05 in X and Y directions and with sides of 3e-05 in the z-direction. Figure 4.3 shows a schematic representation of the mesh used in the numerical simulations.

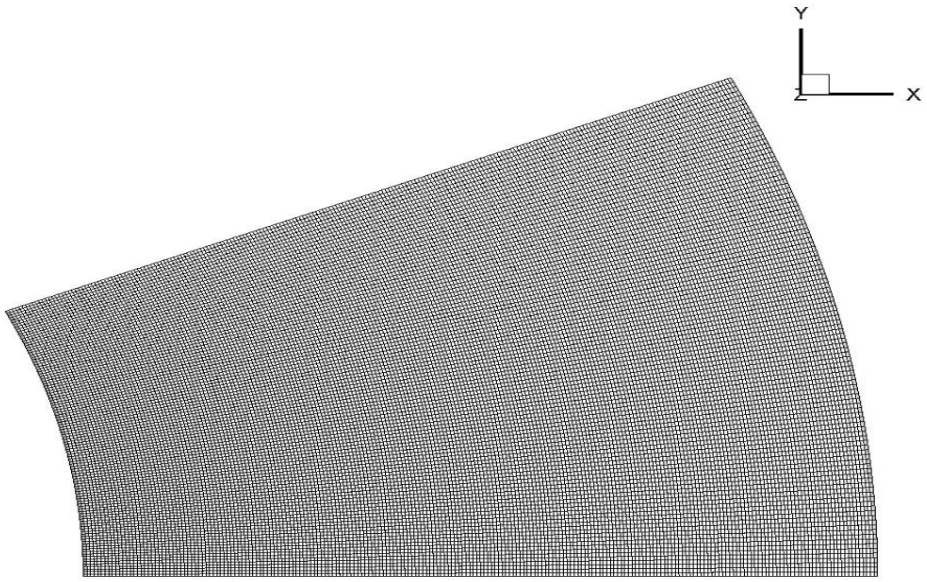

Figure 4.3. Spatial discretization of the computational domain for molten slag material

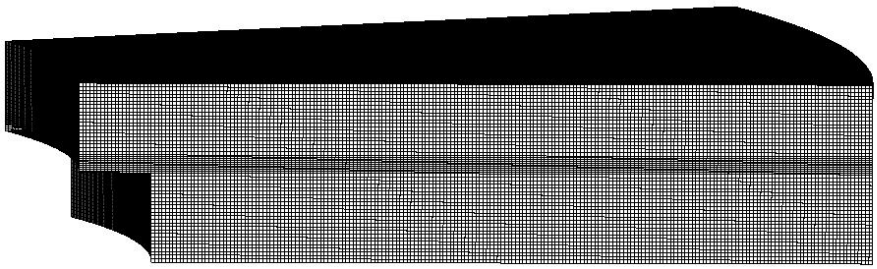

Figure 4.4. Spatial discretization of the computational domain for aqueous glycerol material

4.5. Settings and Solvers

In both cases, similar settings and solvers are applied to perform numerical simulations. In the computational domain Pressure and velocity, values are stored at the center of a cell using

finite volume methods in Fluent. Second order upwind scheme is used to interpolate the cell-centered values, and pressure values are interpolated using pressure staggering option (PRESTO). Least squares cell-based approach is used to compute gradients in the flow field. First order implicit formulation is used to discretize the time and explicit VOF methods are used to capture the interface. Fluent should be in double-precision mode to reduce round-off error. Pressure and velocity fields are coupled using Pressure implicit with the splitting of operators (PISO) algorithm in ANSYS FLUENT because an accurate adjustment of the face mass flux correction according to the normal pressure gradient can be achieved in transient simulations using PISO algorithm.

4.6. Convergence study for different materials

Three different convergence studies are performed to determine the numerical accuracy of the simulations for both materials. The first is the mesh independence study; in this study, the mesh was refined to see if the grid is adequate to resolve the flow features. The second is the temporal convergence study; in this study global courant number was varied to check the accuracy of the simulations when the time-step is varied. The third study is a residual convergence study; in this study, the residual cuts off criteria for all equations are varied to determine the sensitivity of mathematical equations to the residual cut-off values.

4.7. Spatial Convergence for molten slag system

Four different mesh densities are used to perform spatial convergence analysis. The coarse grid setup is considered as a base mesh. The base mesh is refined throughout the domain to produce high mesh densities. In this analysis, non-dimensional Sauter mean diameter and droplet size distribution values are compared for different mesh values to determine the effect of grid resolution on the numerical simulation accuracy.

4.7.1. Sauter mean diameter for different mesh densities

Iterative convergence criterion of 1e-5 and Global courant number of 0.25 is used to perform spatial convergence studies. Table.4.3 represents the obtained values.

Table.4.3. Spatial convergence of D_{32}^{*} for (Ek-7.83e-05, Oh-0.0143, and Re-458)

Mesh	**No.of.Cells**	$\boldsymbol{D_{32}^{*}}$
Meshslag-1	720000	0.0115
Meshslag-2	943200	0.0113
Meshslag-3	1257800	0.0110
Meshslag-4	2419480	0.0110

The ratio of the refined mesh and the base mesh is 1.3, and from the results, it is noticed that the Sauter mean diameter D_{32}^{*} value is insensitive to the grid resolution and mesh convergence is achieved.

4.7.2. Droplet size distribution for different mesh densities

Figure 4.5 shows the comparison of droplet size distribution for different mesh densities for a slag system.

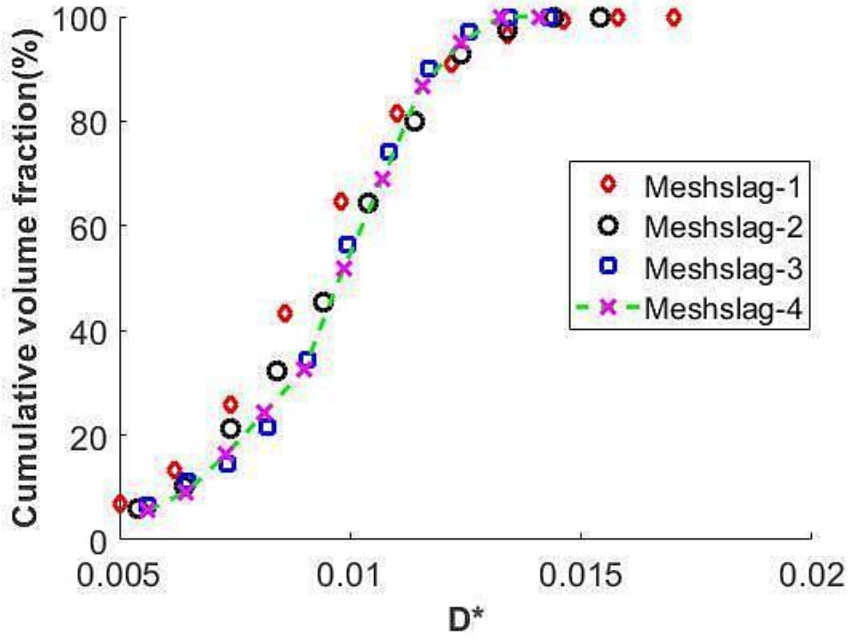

Figure 4.5. Spatial convergence study for Ek-7.83e-05, Oh-0.0143, and Re-458 (Molten slag material)

High mesh density is required to track the interface between two fluids and to capture the droplet breakup process during the atomization process. The droplet size distribution obtained using Meshslag-3 is comparable to the results produced from Meshslag-4. Therefore, Meshslag-3 is chosen to perform the case studies.

4.8. Spatial Convergence study for the aqueous glycerol material

Similar to slag system, base mesh is refined throughout the domain to produce finer grid resolutions to perform mesh convergence studies on domain2. Three different mesh densities are used to analyze grid convergence. Non-dimensional Sauter mean diameter values and droplet size distribution are compared to study the effects of mesh density on the accuracy of numerical modeling.

4.8.1 Sauter mean diameter for different mesh densities

Global courant number of 0.3 and iterative convergence cut-off value of 1e-05 is used for all equations to conduct spatial convergence study. Table.4.4 shows the results.

Table.4.4. Spatial convergence of D_{32}^{*} for (Ek-2.72e-05, Oh-0.0085, and Re-1312)

Mesh	**No.of.Cells**	$\boldsymbol{D_{32}^{*}}$
Meshgly-1	2129664	0.0074
Meshgly-2	2799994	0.0071
Meshgly-3	4736000	0.00706

Even for this case, the ratio of the refined mesh and the base mesh is 1.3. From analyzing the obtained results, it is noticed that the Sauter mean diameter (D_{32}^{*}) values are grid independent and further refinement of the mesh is not required to resolve the flow features. Also, the change of Sauter diameter value (D_{32}^{*}) is insignificant between Meshgly-2 and Meshgly-3.

4.8.2. Droplet size distribution for different mesh densities

Figure.4.6 represents the comparison of droplet size distribution for different mesh densities for an aqueous glycerol solution.

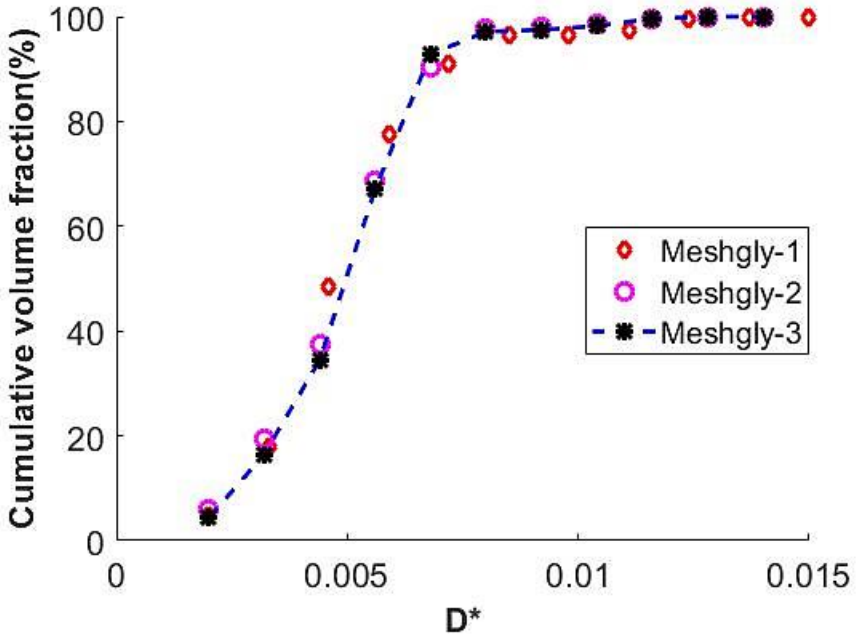

Figure 4.6. Spatial convergence study for Ek-2.72e-05, Oh-0.0085, and Re-1312 (Aqueous glycerol solution)

As mentioned earlier, a high-density mesh is required to resolve the sharp velocity gradients and to capture accurate physics during droplet breakup phenomenon. From the results, it is noticed that the droplet size distribution obtained from Meshgly-2 is comparable to the values produced by Meshgly-3. Therefore, Meshgly-2 is chosen to conduct parametric studies.

4.9. Time Convergence for molten slag material

In this thesis, the Variable time stepping methodology is used to vary time step size. The time step magnitude is dependent on the Courant-Friedrichs-Lewy (CFL) condition, which is also known as the Courant number.

$$\Delta t = \frac{Courant\ number}{\max \sum \left(\frac{outgoing\ fluxes\ in\ cell}{volume\ of\ the\ cell} \right)} \tag{4.12}$$

Global courant number is varied to determine the effect of time step size on the simulations. Sauter mean diameter (D_{32}^{*}) and droplet size distribution values are compared for different courant numbers in order to determine the sensitivity of mathematical equations to time step size.

4.9.1. Sauter mean diameter for different courant numbers

In these simulations, Meshslag-3 with an iterative convergence criterion of 1e-5 was used to perform simulations, and Table.4.5 represents the obtained values.

Table.4.5. Time convergence of D_{32}^{*} for (Ek-7.83e-05, Oh-0.0143, and Re-458)

Courant number(CN)	**Global Courant no**	$\boldsymbol{D_{32}^{*}}$
CNslag-1	0.3	0.0112
CNslag-2	0.25	0.0110
CNslag-3	0.2	0.0111

Global courant number criteria changes from 0.3 to 0.2. By analyzing the obtained values, it is noticed that the Sauter mean diameter (D_{32}^{*}) value is not affected by varying the Global courant number criteria from 0.25 to 0.2.

4.9.2. Droplet size distribution for different courant numbers

Figure.4.7 shows the comparison of droplet size distribution for different courant numbers for a slag system.

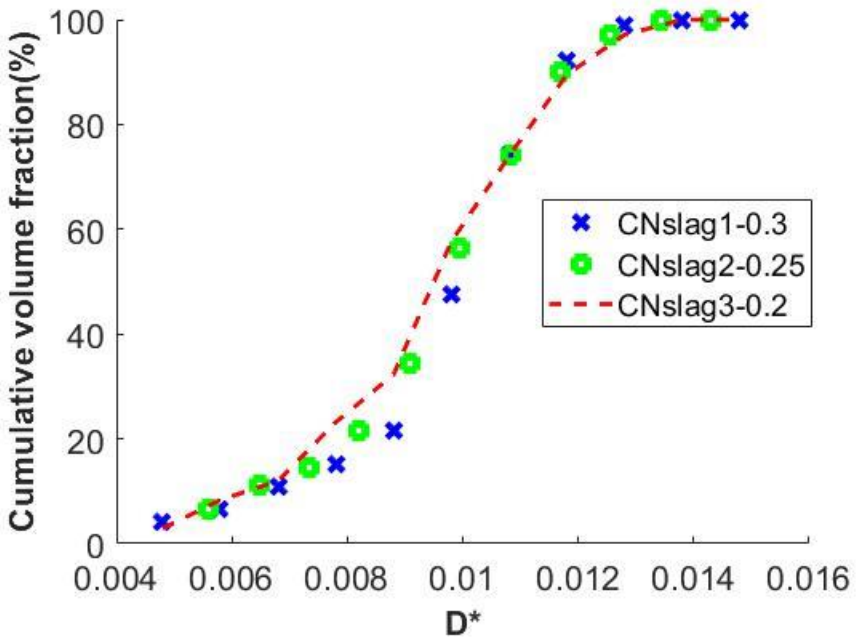

Figure 4.7. Time convergence study for Ek-7.83e-05, Oh-0.0143, and Re-458 (Molten slag material)

The drop size distribution obtained using CNslag-2 is comparable to the results produced from CNslag-3. Therefore, global courant number of 0.25 is used to conduct parametric simulations.

4.10. Time Convergence for aqueous glycerol material

For aqueous glycerol material, the global courant number is varied to determine the effect of time step size on the system of mathematical equations.

4.10.1. Sauter mean diameter for different courant numbers

In these simulations, Meshgly-2 is chosen with a residual convergence criterion of 1e-5 to perform numerical analysis, and Table.4.6 shows the results.

Table.4.6. Time convergence of D_{32}^{*} for case2 (Ek-2.72e-05, Oh-0.0085, and Re-1312)

Courant number(CN)	**Global Courant no**	$\boldsymbol{D_{32}^{*}}$
CNgly-1	0.2	0.0069
CNgly-2	0.25	0.0069
CNgly-3	0.3	0.0071

Global courant number criteria changes from 0.3 to 0.2. By analyzing the results, it is noticed that the global courant number does not have a significant effect on the droplet breakup process. Moreover, the change in D_{32}^{*} between CNgly-2 and CNgly-3 is insignificant.

4.10.2. Droplet size distribution for different courant numbers

Figure 4.8 shows the comparison of droplet size distribution for different courant numbers for aqueous glycerol.

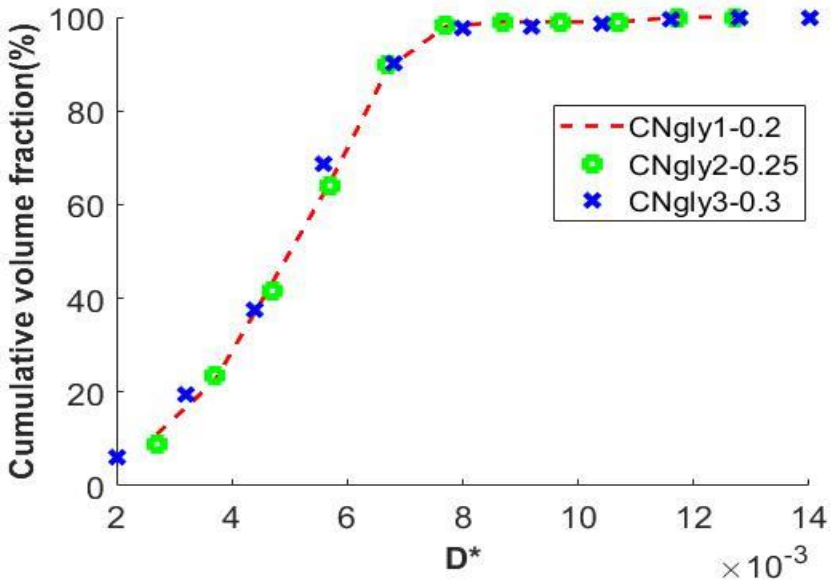

Figure 4.8. Time convergence study for Ek-2.72e-05, Oh-0.0085, and Re-1312 (Aqueous glycerol solution)

From the time convergence analysis, it can be found that a global courant number of 0.25 can be used to conduct parametric simulations for aqueous glycerol material because the droplet size distribution values obtained for courant number 0.25 is comparable to the values produced using a Courant number of 0.2.

4.11. Residual Convergence for molten slag material

For the residual convergence, three different convergence cut-off values were chosen to determine the convergence for the simulations. Six residual criteria are changed within Fluent: continuity, x-velocity, y-velocity, z- velocity, k –Turbulent kinetic energy and ϖ – specific dissipation rate. These simulations are performed using Meshslag-3 and a courant number of 0.25 and the results are represented in Table.4.7.

4.11.1. Sauter mean diameter for different residual cut-off values

Table.4.7. Residual convergence of D_{32}^{*} for (Ek-7.83e-05, Oh-0.0143, and Re-458)

Convergence criteria(CC)	**Residual cut-off**	$\boldsymbol{D_{32}^{*}}$
CCslag-1	1e-04	0.0112
CCslag-2	1e-05	0.0110
CCslag-3	1e-06	0.0111

The residual convergence criteria changes from 1e-04 to 1e-06. From the results, It is found that the Sauter mean diameter (D_{32}^{*}) value is insensitive to the residual convergence criteria.

4.11.2 Droplet size distribution for different residual convergence values

Figure 4.9 shows the comparison of droplet size distribution for different convergence criteria for a slag system.

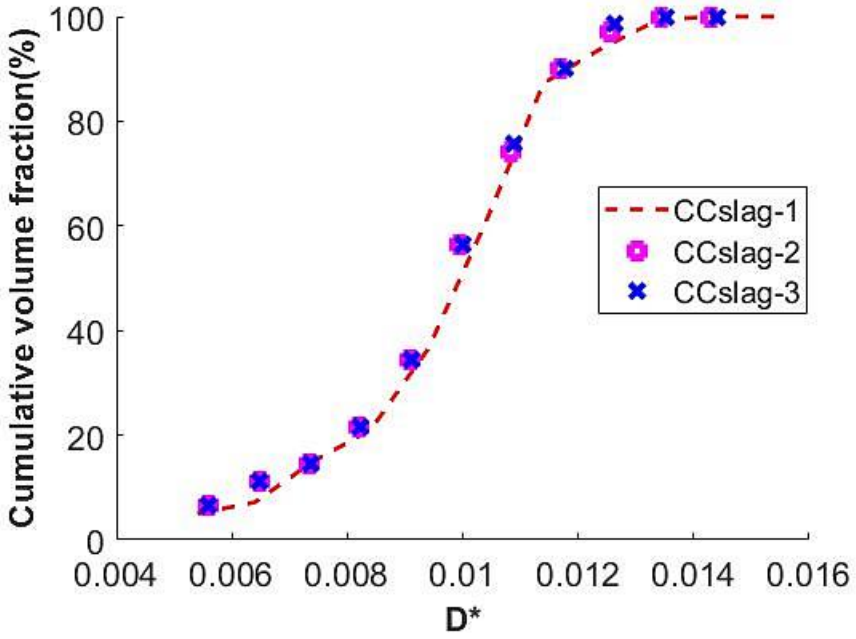

Figure 4.9. Residual convergence study for Ek-7.83e-05, Oh-0.0143, and Re-458 (Molten slag material)

Stringent convergence criteria are required to obtain highly accurate numerical results. It is noticed that the droplet size distribution produced by CCslag-2 is comparable to the results obtained using CCslag-3. Therefore, CCslag-2 is used to analyze case studies. From these three convergence study analysis, it is found that a grid set up with around 1 million cells should be used to run parametric studies using a global courant number of 0.25 and residual criteria of 1e-05.

4.12. Residual Convergence study for the aqueous glycerol material

Six different criteria in ANSYS fluent are varied to perform Iterative convergence criteria: continuity, x-velocity, y-velocity, z- velocity, k –Turbulent kinetic energy and ϖ – specific dissipation rate.

4.12.1. Sauter mean diameter for different residual cut-off values

This convergence study was conducted using Meshgly-2 and a global courant number of 0.25. Table.4.8 represents the resultant data.

Table.4.8. Residual convergence of D_{32}^{*} for (Ek-2.72e-05, Oh-0.0085, and Re-1312)

Convergence criteria(CC)	**Residuals cut-off**	$\boldsymbol{D_{32}^{*}}$
CCgly-1	1e-04	0.0072
CCgly-2	1e-05	0.0069
CCgly-3	5e-06	0.0069

The convergence criteria changes from 1e-04 to 5e-06. From the obtained results, it can be observed that the Sauter mean diameter (D_{32}^{*}) value is not effected by changing the iterative convergence cut off criteria. Therefore, it is concluded that the simulations are independent of residual criteria.

4.12.2. Droplet size distribution for different residual cut-off values

Figure 4.10 shows the comparison of droplet size distribution for different convergence criteria for an aqueous glycerol solution.

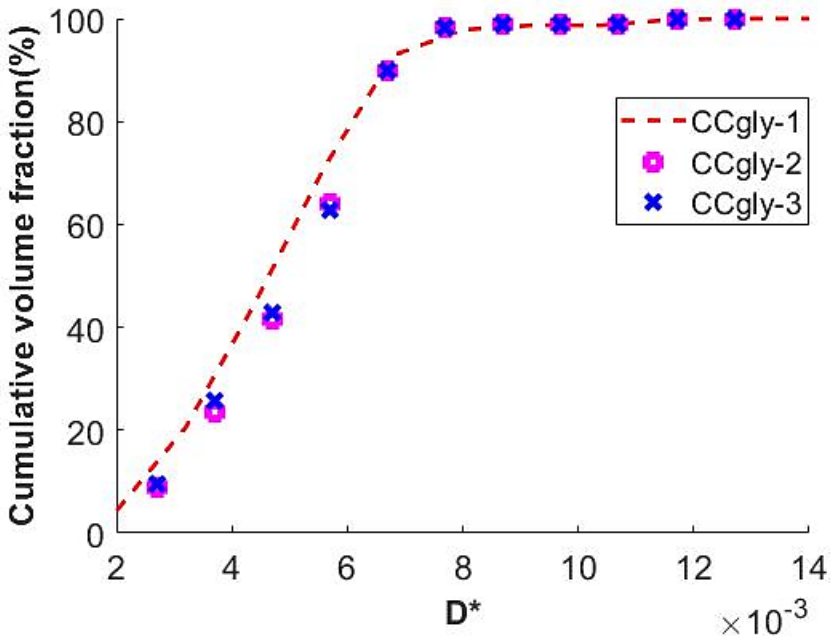

Figure 4.10. Residual convergence study for Ek-2.72e-05, Oh-0.0085, and Re-1312 (Aqueous glycerol solution)

Stringent residual criterion is imposed on the numerical equations to achieve accuracy. Moreover, from results, it is noticed that the change in droplet size distribution is insignificant for different residual criteria. Therefore, for aqueous glycerol material residual cut off value of 1e-05 is chosen to conduct parametric studies.

Chapter 5
Results and observations

5.1. Procedure

The primary purpose of this thesis work is to determine the influence of Reynolds number, Ohnesorge number and Ekman number on the droplet size distribution, Sauter mean diameter and ligament length values produced during centrifugal atomization process. Molten slag, aqueous glycerol solution, and molten nickel-niobium metal are the materials used for performing numerical simulation in two computational domains. The effects of non-dimensional parameters on the ligament mode atomization process are analyzed by performing a parametric study on these materials.

In many atomization processes, the mean droplet diameters and droplet size distribution describes the quantitative information on the atomization quality. Sauter mean diameter (SMD) is the ratio of volume to surface area as the whole ensemble, and it is usually more significant than the surface, volume and arithmetic diameters. In most of the additive manufacturing applications, SMD values are used to describe the fineness of the spray and the atomization quality is expressed by using SMD values [51].

$$D_{32} = \frac{\sum D_i^3}{\sum D_i^2}$$

Figure 5.1 shows the complete evolution of Air-Molten metal interface shape during the ligament mode atomization process by using Volume of Fluid methodology.

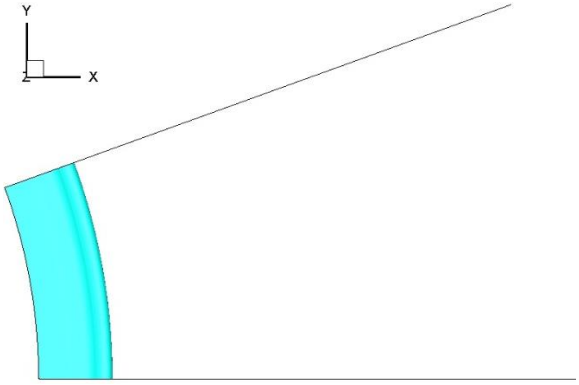

A. Annular ring structure at disk edge

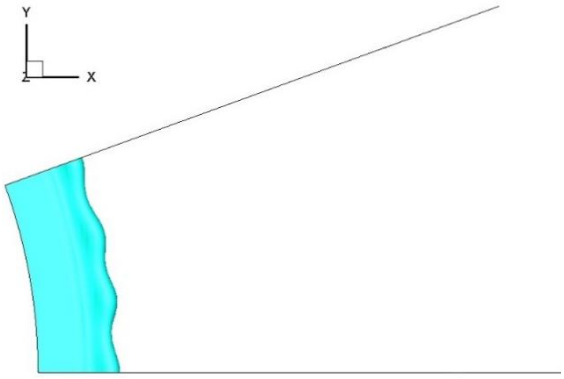

B. Formation of Torus structures

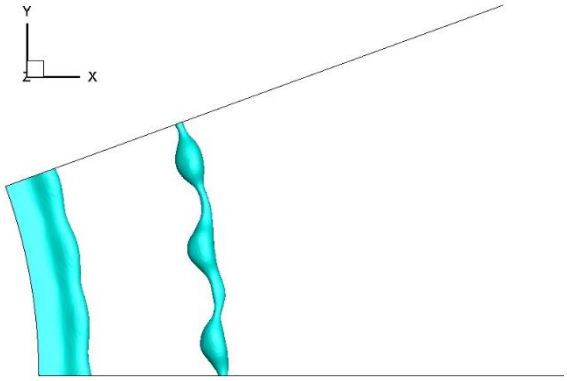

C. Secondary breakup process

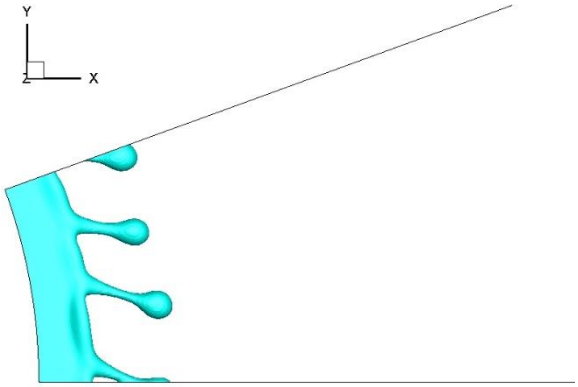

D. Stretching and bulging of ligament

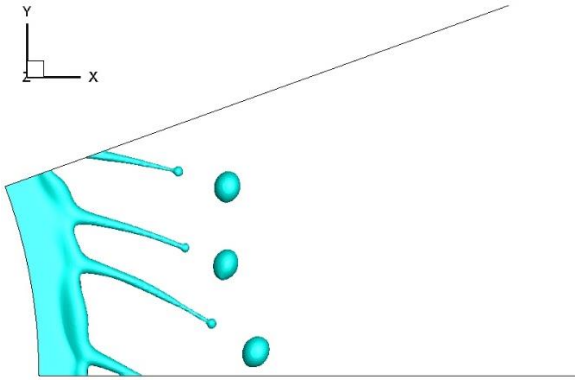

E. Stretching and thinning of ligaments

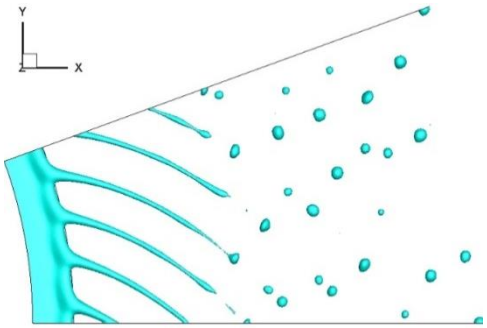

F. Quasi-steady state process of atomization

Figure 5.1. Overall flow structure for Ni-Nb at (Ek-2.36e^{-05},Oh-0.0039, Re-3584) (A)t= 6 ms;(B)t=14 ms ;(C)t=18 ms;(D)t=23 ms;(E)t=26 ms; (F)t=74 ms;

From Figure.5.1, it is observed that after a significant amount of time, due to the influence of surface tension and centrifugal forces the liquid film will disintegrate into torus structures. The connection section between the liquid film and the torus structure will keep growing. Because of this growth, the connection section becomes very thin, and finally, the torus structure will detach from the liquid film, which is known as a primary breakup. The detached liquid film will move in a radial direction continuously, and the surface tension effects will disintegrate the liquid film into large droplets. This phenomenon is known as a secondary breakup. Simultaneously, another torus structure will appear at the disk edge, which is the first stage of ligament formation.

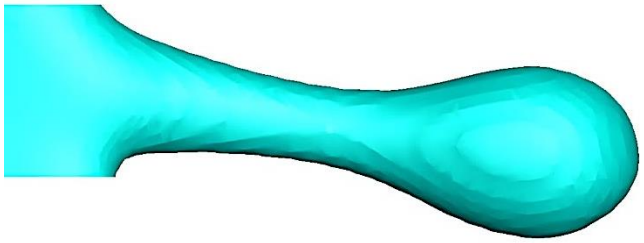

Figure 5.2. Torus structure at the edge of the disk at (Ek-2.36e^{-05},Oh-0.0039, Re-3584)

Under the influence of centrifugal and surface tension forces, initially formed ligaments undergo stretching and thinning phenomenon. The ligaments will stretch up to a certain length in radial direction before it disintegrates into fine droplets.

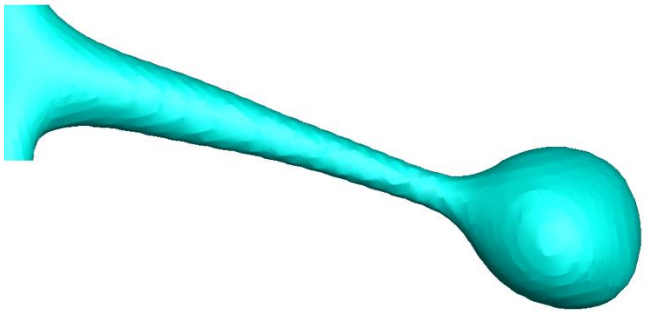

Figure 5.3. Stretching phenomenon of a ligament in the radial direction at (Ek-2.36e^{-05},Oh-0.0039, Re-3584)

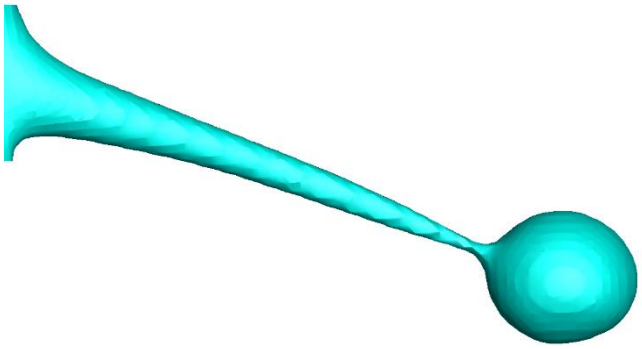

Figure 5.4. Thinning phenomenon of a ligament at (Ek-2.36e^{-05},Oh-0.0039, Re-3584)

Due to the phenomenon of stretching and thinning, initially formed ligaments will disintegrate into fine droplets under the quasi-steady state process. Figure 5.5 demonstrates the ligament disintegration process.

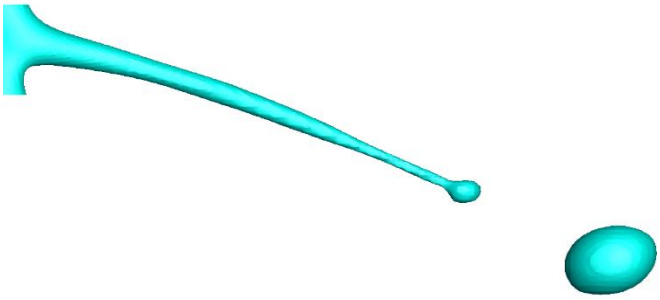

Figure 5.5. Disintegration of ligament into large droplet during first breakup at (Ek-2.36e^{-05},Oh-0.0039, Re-3584)

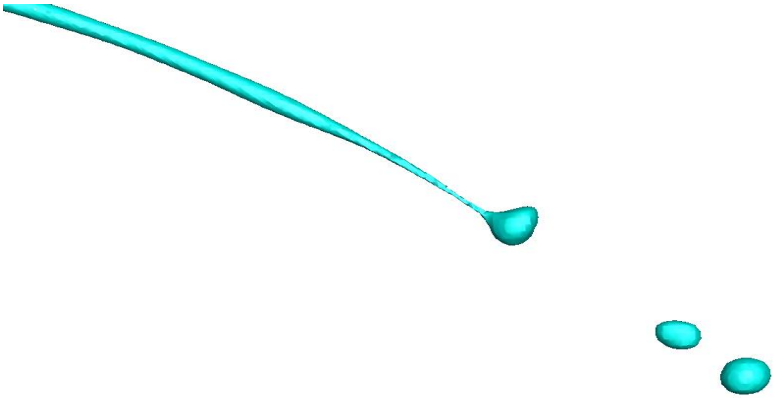

Figure 5.6. Disintegration of ligament into fine droplets at (Ek-2.36e^{-05},Oh-0.0039, Re-3584)

The observed ligaments stream is similar to the involute of a circle and Frost [26] also observed this phenomenon experimentally, and Liu et al [2] determines that the instabilities on the air-liquid interface are the primary source of disturbances, which cause ligament formation. Several types of instabilities exist at the air-liquid interface, such as Kelvin Helmholtz instability. However, the most critical instability in these simulations is the Rayleigh Taylor (RT) instability.

5.2. Verification with numerical experiments

In this thesis, an initial study is conducted to determine the accuracy of the numerical models used in the simulations. Wang et al. [51] has performed a dimensional analysis on the ligament mode atomization process using the volume of fluid methodology for 3 different viscous values and 750000 hexahedral cells on a $caO - SiO_2 - MgO - Al_2O_3$ slag system. The operating parameters and material properties for the slag system at 1450 C are described in the below Table.5.1

Table.5.1. Dimensional material properties of slag system

Case	$\boldsymbol{\rho(\frac{kg}{m^3})}$	$\boldsymbol{\mu\ (pa.s)}$	$\boldsymbol{\sigma(\frac{N}{m})}$	$\boldsymbol{D(mm)}$	$\boldsymbol{Q\left(\frac{ml}{s}\right)}$	$\boldsymbol{\omega(\frac{rad}{s})}$
Case1	2612	0.125	0.538	54	12.8	209.44
Case2	2612	0.25	0.538	54	12.8	209.44
Case3	2612	0.334	0.538	54	12.8	209.44

The primary objective of Wang et al. [51] study is to determine the effects of viscosity on the Sauter mean diameter (SMD) and droplet size distribution values. Table 5.2 represents the results obtained from Wang et al. study.

Table.5.2. Dimensional values of D_{32} for the slag system from Wang.et.al

Case	**SMD(D_{32}) (mm)**
Case1	0.656
Case2	0.743
Case3	0.826

A similar study is performed using identical operating parameters, material properties, and boundary conditions. The numerical simulation is conducted using Mesh_Slag_3 grid setup and the results obtained from these simulations are shown in the below Table5.3.

Table.5.3. Dimensional values of D_{32} for the slag system from numerical simulations

Case	**SMD(D_{32}) (mm)**
Case1	0.601
Case2	0.6433
Case3	0.6974

The obtained SMD values from the two studies are different. The droplet diameter values obtained using Mesh_slag_3 grid setup in this thesis are smaller than the diameter values obtained by Wang.et.al [51]. This variation in droplet size diameter is because Mesh_slag_3 grid setup had more number of hexahedral cells, which were able to capture the formation of smaller droplets near the tip of the ligaments during ligament disintegration process. Figure 5.7 shows a direct comparison between numerical results, Wang et al. [51] and Frost et al. [26].

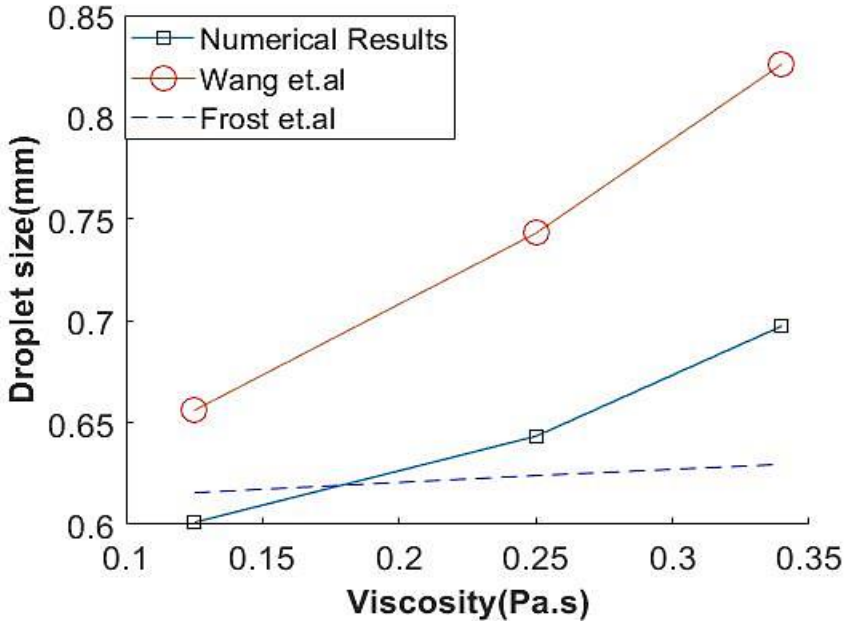

Figure 5.7.Comparison with Wang.et.al [51]

Frost et al. [26] has developed a correlation to predict droplet size diameter for a slag system by performing an experimental analysis on the droplet breakup process using a rotary atomization mechanism. From the above results, it can be observed that the results obtained from numerical analysis are in close agreement with the correlation developed by Frost et.al [26].

5.3. Parametric analysis

In this thesis, three different materials are chosen to perform parametric analysis. Table.5.4 represents the three different materials and their properties.

Table.5.4. Material properties of molten slag, glycerol, and molten Ni-Nb materials

Material	$\boldsymbol{\rho}(\frac{\boldsymbol{kg}}{\boldsymbol{m^3}})$	$\boldsymbol{\mu}\ (\boldsymbol{pa.s})$	$\boldsymbol{\sigma}(\frac{\boldsymbol{N}}{\boldsymbol{m}})$
$\boldsymbol{caO - SiO_2 - MgO - Al_2O_3}$	2612	0.125	0.538
Water + 60% glycerol	1170	0.0175	0.073
Molten Ni-Nb	8000	0.09	1.34

For each material, only one non-dimensional parameter is varied at a time to perform the parametric study. The angular speed of the disk is varied to change Ekman number. Likewise, the surface tension and mass flow rate is varied to change Ohnesorge number and Reynolds number. The influence of different non-dimensional parameters on the atomization process are determined by analyzing and evaluating the Sauter mean diameter (SMD), droplet size distribution and length of the ligaments. Moreover, these parameters are captured in quasi-steady state condition. The total volume occupied by each particle in the computational domain is analyzed to determine the size of droplets. Each droplet particle volume is captured using a customized user developed function in ANSYS FLUENT.

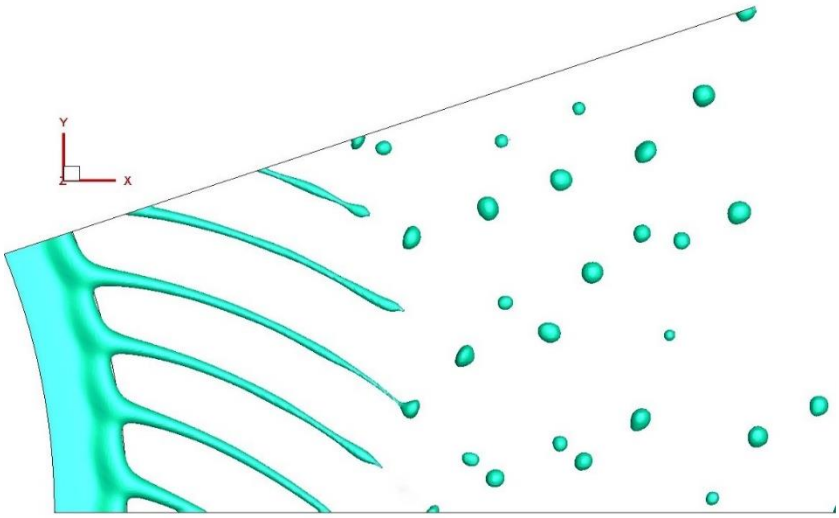

Figure 5.8. Droplet breakup process of Ni-Nb at (Ek-2.36e^{-05},Oh-0.0039, Re-3584)

Another important parameter in ligament mode atomization is the mean value of ligament length. This value is measured by summing up the length of the lines used to connect all the centroid values of different segments of a ligament. A customized MATLAB code is developed to automate the process. In addition, SMD values at different locations are analyzed to discern the variation of mean diameter values along the radial direction in the computational domain.

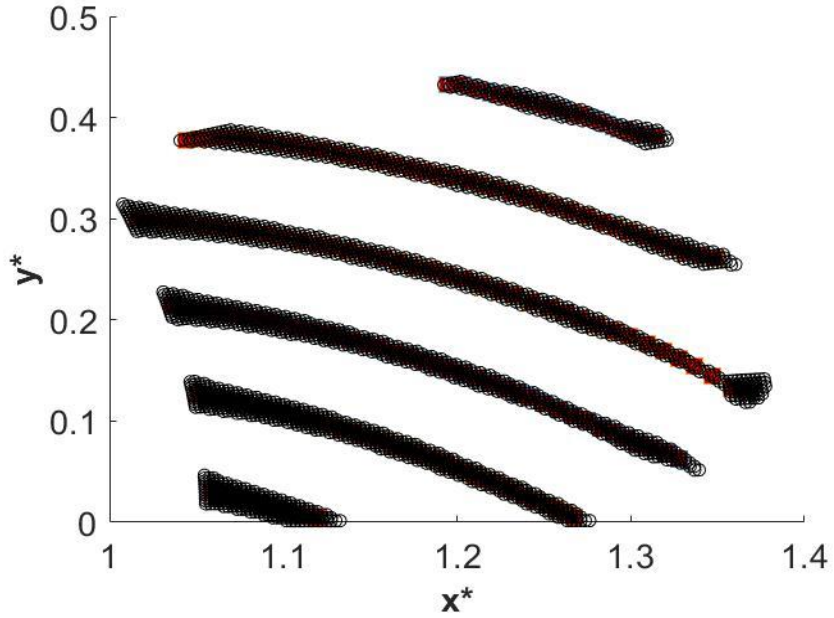

Figure 5.9. Extracted data points to measure ligament length at (Ek-2.36e^{-05},Oh-0.0039, Re-3584)

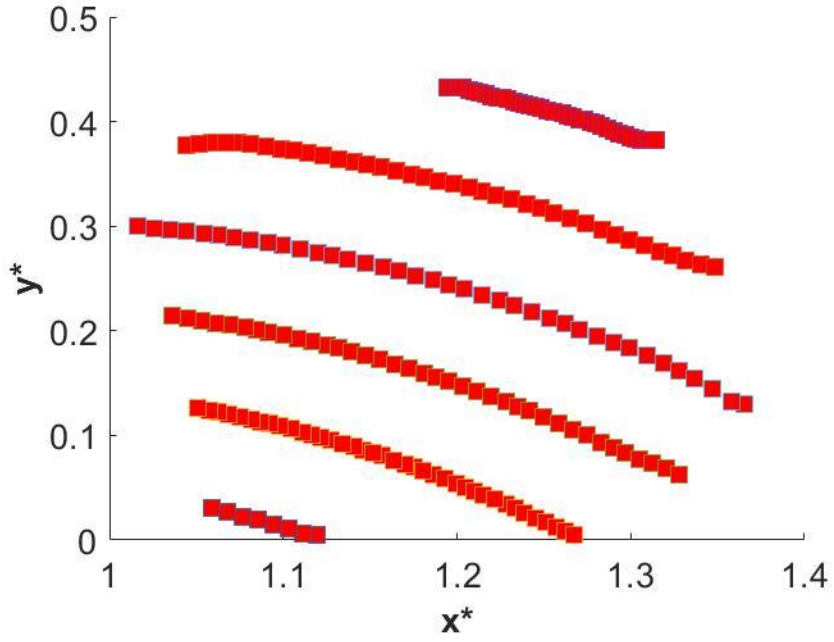

Figure 5.10. Centroid points at different segments of a ligament at (Ek-2.36e^{-05},Oh-0.0039, Re-3584)

In all cases, the velocity distribution across the computational domain follows a similar pattern. Results show that the effect of tangential velocities on the ligament atomization process is

more significant than radial and axial velocities. Figure 5.11 and 5.12 shows contour plots of the non-dimensional radial and tangential velocity distribution across the computational domain for a slag material.

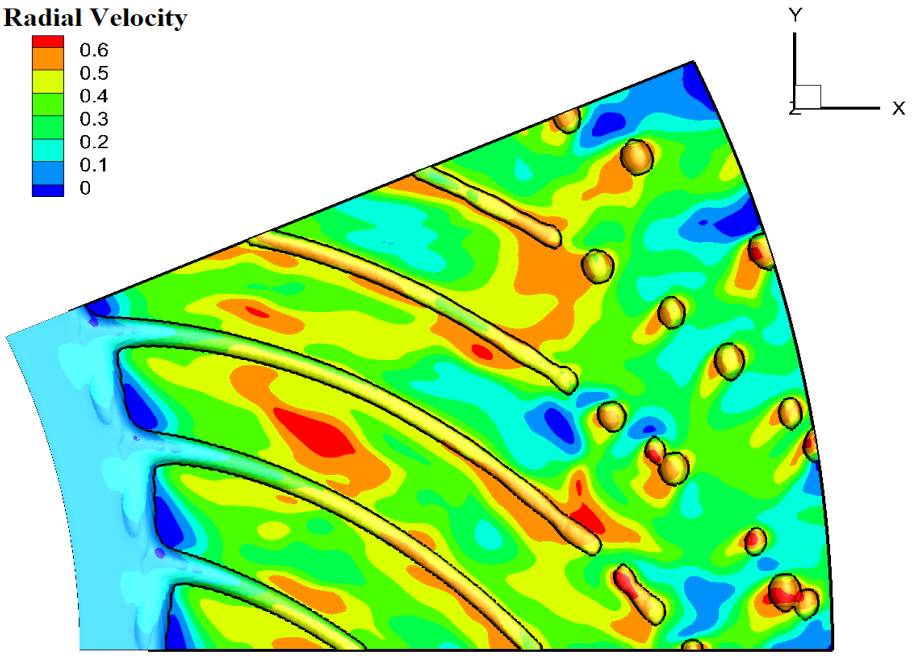

Figure 5.11. Non-dimensional radial velocity for a slag system at (Ek-1.56e-04, Oh-0.0287, and Re-170)

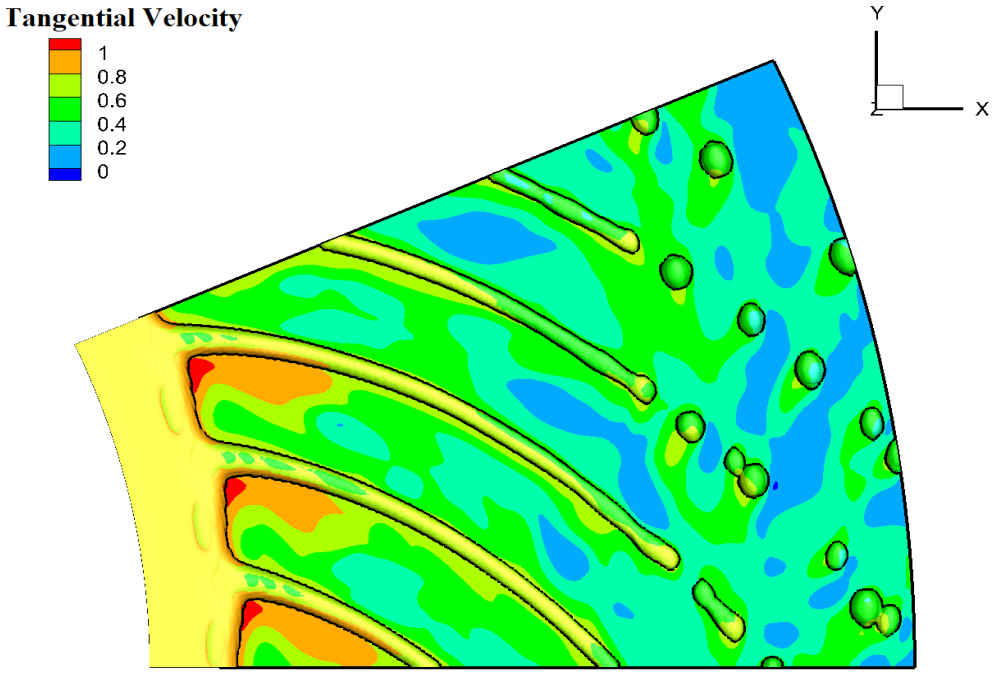

Figure 5.12. Non-dimensional tangential velocity for a slag system at (Ek-1.56e-04, Oh-0.0287, and Re-170)

5.3.1. Effect of Ekman number on different materials

The first parametric analysis is performed to study the influence of Ekman number on various parameters in the atomization process. Tables [5.5, 5.6, and 5.7] shows the effect of Ekman number on SMD and ligament length. Results demonstrate that the size of the particle increases with an increase in Ekman number. An observed increase of the droplet size with increase in Ekman number is due to the decrease of the atomization energy, where the applied energy to the fluid decreases with the increase of Ekman number. Previous studies have mentioned that decreasing the rotational speed of the disk increases the thickness of the fluid at the edge of the disk, and decreases the angular displacement of the fluid, resulting in a lower average velocity of the liquid leaving the disk. The lower the velocity, the larger the droplets produced. Another important parameter to track in the ligament mode atomization process is ligament length.

Table.5.5. D_{32}^{*} and L* Values for a slag system with a constant (Oh-0.0143, Re-458) and varying Ek-($7.8e^{-05}, 8.4e^{-05}, 9.8e^{-05}$)

Material	**Ekman number (Ek)**	**SMD (D_{32}^{*})**	**L***
$\boldsymbol{caO - SiO_2 - MgO - Al_2O_3}$	7.8e-05	0.0110	0.1944
	8.4e-05	0.0124	0.2352
	9.8e-05	0.0135	0.2444

Table.5.6. D_{32}^{*} and L* Values for an aqueous glycerol with a constant (Oh-0.0085, Re-1312) and varying Ek - ($2.72e^{-05}, 3.19e^{-05}, 3.81e^{-05}$)

Material	**Ekman number (Ek)**	**SMD (D_{32}^{*})**	**L***
Water + 60% glycerol	2.72e-05	0.0069	0.078
	3.19e-05	0.0098	0.122
	3.81e-05	0.0115	0.15

Table.5.7. D_{32}^{*} and L* Values for Ni-Nb with a constant (Oh-0.0039, Re-3584) and varying Ek-($1.63e^{-05}, 2.04e^{-05}, 2.36e^{-05}$)

Material	Ekman number (Ek)	SMD (D_{32}^{*})	L*
Nickel-Niobium	1.63e-05	0.0096	0.068
	2.04e-05	0.0129	0.102
	2.36e-05	0.0165	0.184

From the obtained results it is observed that as the Ekman number increases the ligament length increases. This phenomenon occurs due to a decrease in atomization energy received by the thin liquid film at the edge of the disk. Because of negligible disturbances and lower atomization energy, wavelength of dilatational waves becomes long, and longer ligaments are produced. Figure 5.13, 5.14 and 5.15 shows the droplet size distribution for all different Ekman number.

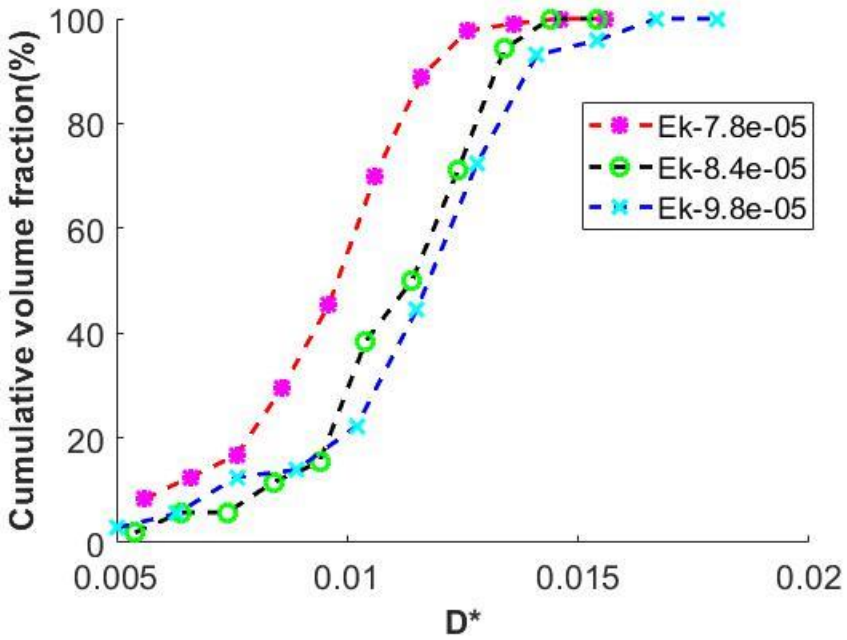

Figure 5.13. Comparison of non-dimensional droplet size distribution for slag system with a constant (Oh-0.0143, Re-458) and varying Ek-($7.8e^{-05}, 8.4e^{-05}, 9.8e^{-05}$)

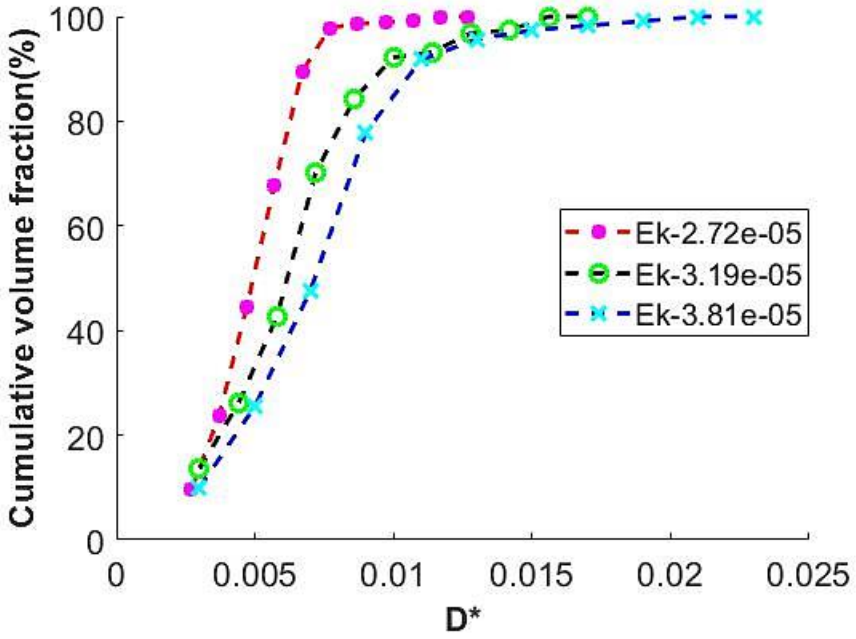

Figure 5.14.Comparison of non-dimensional droplet size distribution for aqueous glycerol solution with a constant (Oh-0.0085 Re-1312) and varying Ek-($2.72e^{-05}, 3.19e^{-05}, 3.81e^{-05}$)

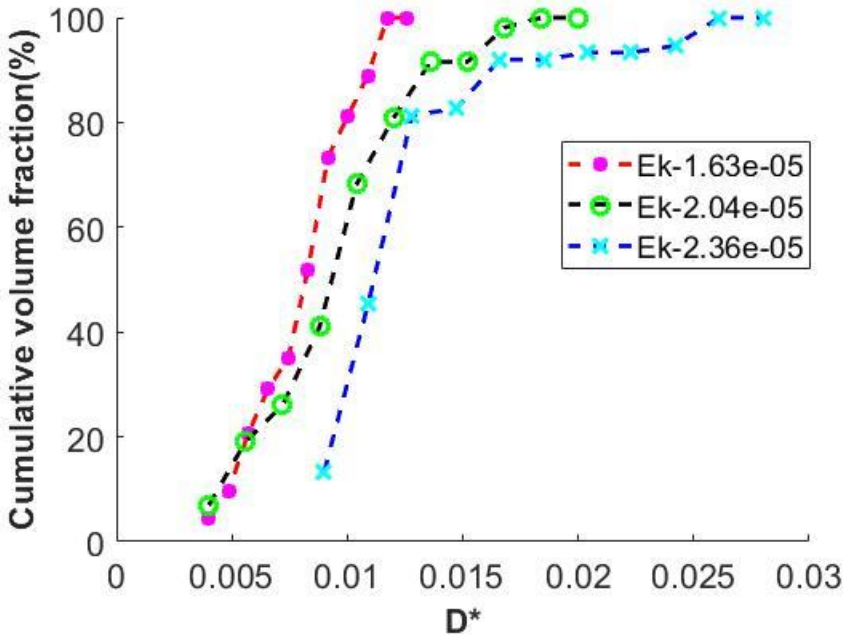

Figure 5.15. Comparison of non-dimensional droplet size distribution for Ni-Nb with a constant (Oh-0.0039 Re-3584) and varying Ek-($1.63e^{-05}, 2.04e^{-05}, 2.36e^{-05}$)

Results demonstrate that as the Ekman number increases, the droplet size distribution curve shifts right in the graph. This means larger droplets are produced by imposing higher Ekman

number. Another study is conducted to determine the variation of mean diameter values at different locations in the computational domain. The domain is divided into five components, which have equal spacing. Moreover, the SMD values are calculated for each component to determine the variation of SMD values. Tables [5.8, 5.9, and 5.10] represents the variation of SMD values at different locations in a computational domain.

Table.5.8. Variation of non-dimensional SMD values across the computational domain for a molten slag system with a constant (Oh-0.0143, Re-458) and varying Ek- ($7.8e^{-05}, 8.4e^{-05}, 9.8e^{-05}$)

Material	**Ekman number(Ek)**	**Component-I (1.29-1.44) (D_{32}^{*})**	**Component-II (1.44-1.59) (D_{32}^{*})**	**Component-III (1.59-1.74) (D_{32}^{*})**
$\boldsymbol{caO - SiO_2 - MgO - Al_2O_3}$	7.8e-05	0.0095	0.0112	0.0110
	8.4e-05	0.0111	0.013055	0.0126
	9.8e-05	0.0109	0.0133	0.0136

Table.5.9. Variation of non-dimensional SMD values across the computational domain for an aqueous glycerol solution with a constant (Oh-0.0085, Re-1312) and varying Ek - ($2.72e^{-05}, 3.19e^{-05}, 3.81e^{-05}$)

Material	**Ekman number (Ek)**	**Component-I (1.2-1.4) (D_{32}^{*})**	**Component-II (1.4-1.6) (D_{32}^{*})**	**Component-III (1.6-1.8) (D_{32}^{*})**
Water + 60% glycerol	2.72e-05	0.0067	0.00694	0.0064
	3.19e-05	0.0092	0.0086	0.0094
	3.81e-05	0.0102	0.0112	0.012

Table.5.10. Variation of non-dimensional SMD values across the computational domain for Ni-Nb with a constant (Oh-0.0039, Re-3584) and varying Ek-($1.63e^{-05}, 2.04e^{-05}, 2.36e^{-05}$)

Material	**Ekman number (Ek)**	**Component-I (1.2-1.4) (D^*_{32})**	**Component-II (1.4-1.6) (D^*_{32})**	**Component-III (1.6-1.8) (D^*_{32})**
Nickel-Niobium	1.63e-05	0.00976	0.008892	0.007908
	2.04e-05	0.009931	0.009862	0.0013425
	2.36e-05	0.018507	0.01564	0.015315

Variation of droplet size in terms of counts is analyzed for different materials at different Ekman numbers. Droplet size distribution for slag system is shown in Figure 5.16, 5.17 and 5.18.

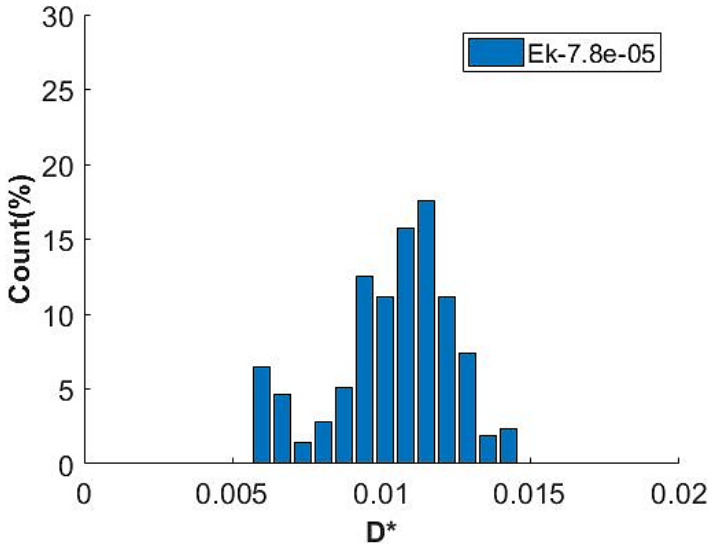

Figure 5.16. Non-dimensional droplet diameter distribution for (Ek-7.8e-05, Oh-0.0143, Re-458)

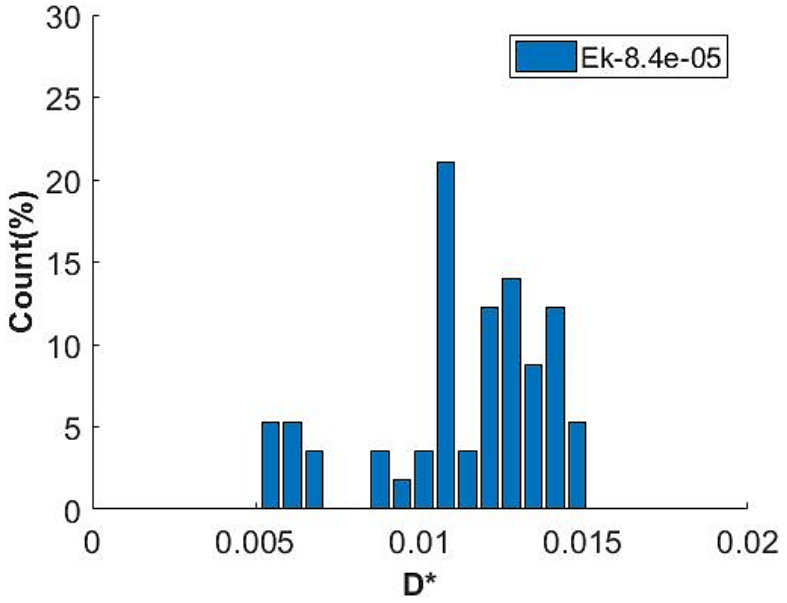

Figure 5.17. Non-dimensional droplet diameter distribution for (Ek-8.4e-05, Oh-0.0143, Re-458)

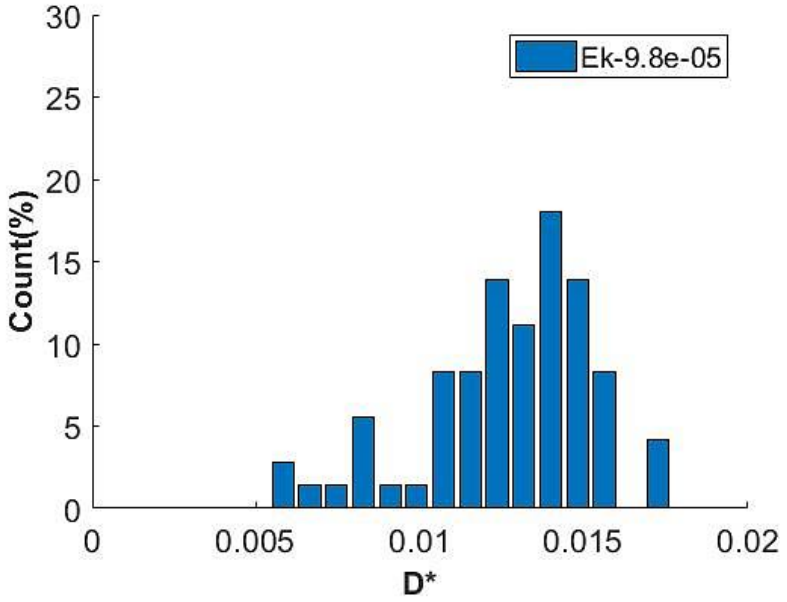

Figure 5.18. Non-dimensional droplet diameter distribution for (Ek-9.8e-05, Oh-0.0143, Re-458)

Figure 5.19, 5.20, 5.21 shows droplet size distribution for aqueous glycerol solution at different Ekman numbers.

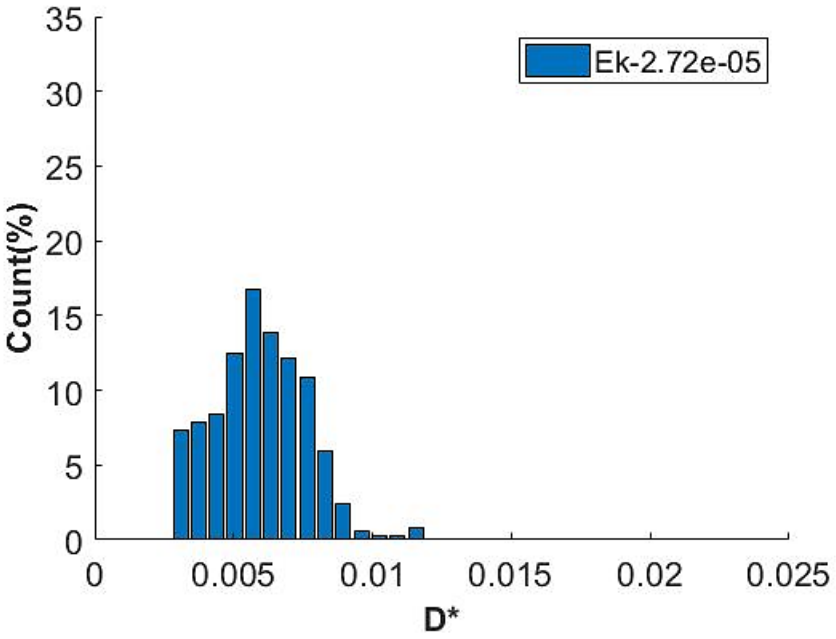

Figure 5.19. Non-dimensional droplet diameter distribution for (Ek-2.72e-05, Oh-0.0085, Re-1312)

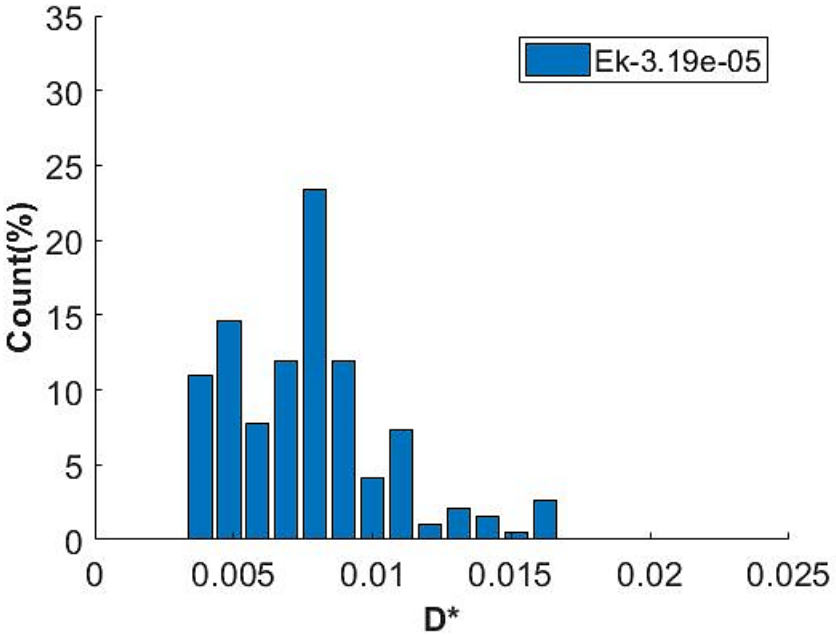

Figure 5.20. Non-dimensional droplet diameter distribution for (Ek-3.19e-05, Oh-0.0085, Re-1312)

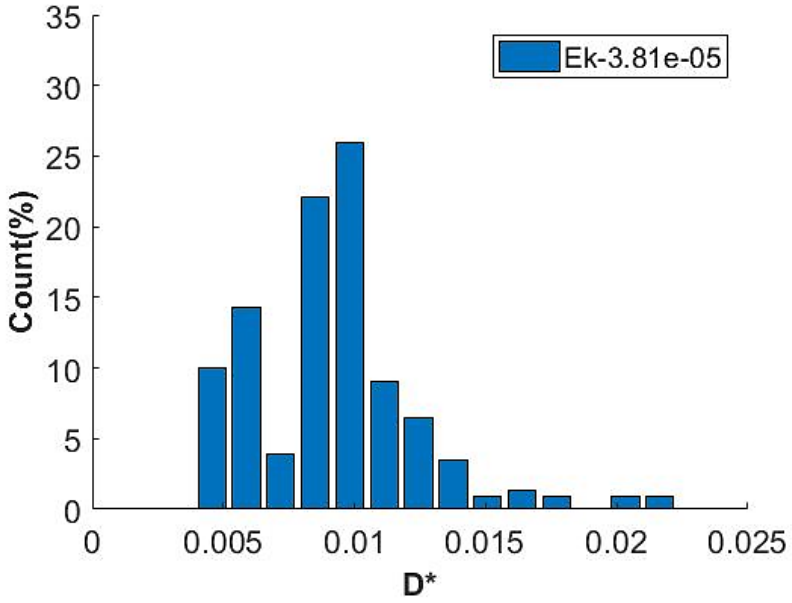

Figure 5.21. Non-dimensional droplet diameter distribution for (Ek-3.81e-05, Oh-0.0085, Re-1312)

Figure 5.22, 5.23, 5.24 demonstrates the variation of droplet size distribution for Ni-Nb material at different Ekman numbers

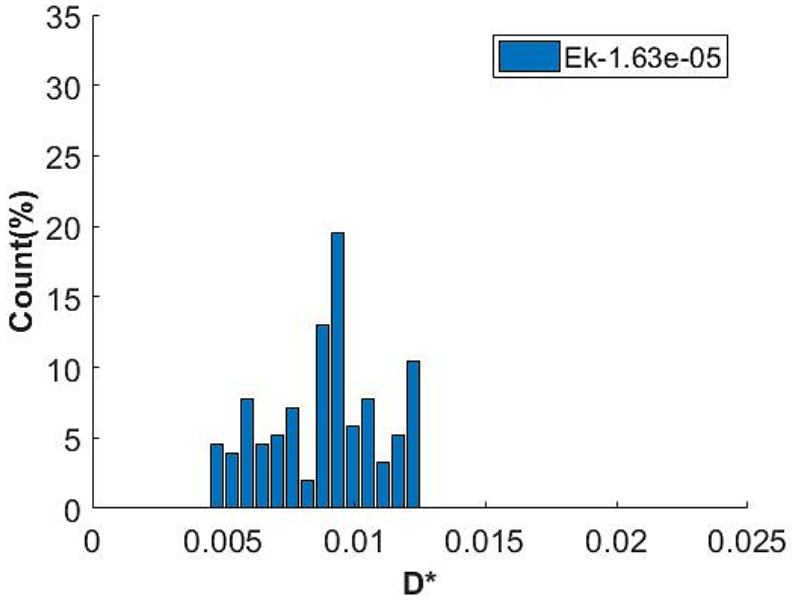

Figure 5.22. Non-dimensional droplet diameter distribution for (Ek-1.63e-05, Oh-0.0039, Re-3584)

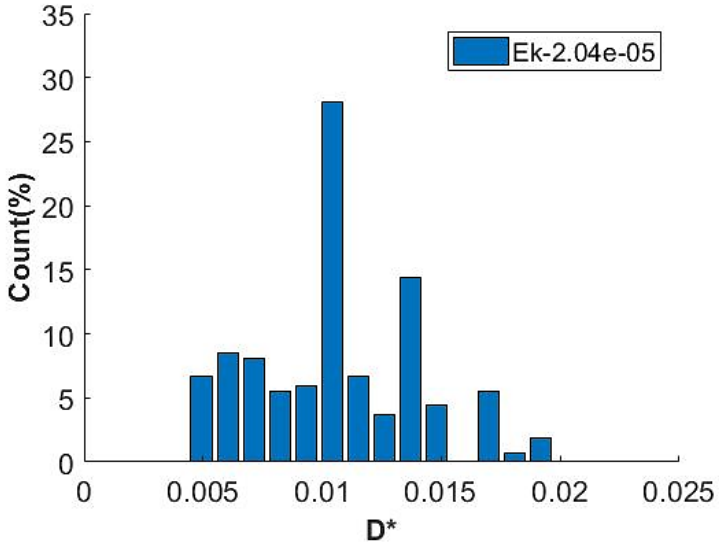

Figure 5.23. Non-dimensional droplet diameter distribution for (Ek-2.04e-05, Oh-0.0039, Re-3584)

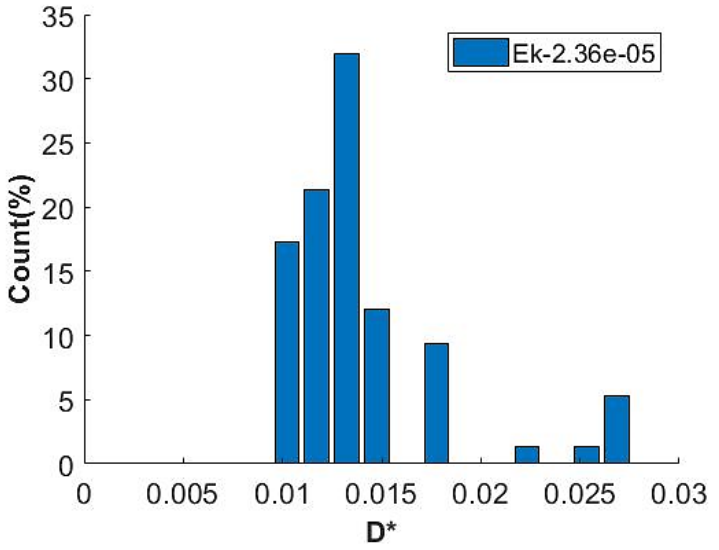

Figure 5.24. Non-dimensional droplet diameter distribution for (Ek-2.36e-05, Oh-0.0039, Re-3584)

Above plots demonstrates the effect of Ekman number on the size of the droplets produced during centrifugal atomization process. Results shows that production of droplets with larger diameter value increases with an increase in Ekman number. This phenomenon is due to the decrease of rotational speed of the disk, which affects the atomization energy.

5.3.2. Effect of Ohnesorge number on different materials

The second parametric analysis is performed to study the influence of Ohnesorge number on various parameters in the atomization process. The input parameters for different materials and the relationship between SMD and the Ohnesorge number is shown in Table [5.11, 5.12 and 5.13]. Results indicate that the particle size becomes more significant by decreasing Ohnesorge number. In the centrifugal atomization process, the thin liquid film is disintegrated into ligaments and then into droplets only when the centrifugal forces overcome the viscous and surface tension forces. Usually, surface tension forces tend to stabilize the liquid film, preventing its breakup and leading to produce droplet with larger diameter. Hence, for a lower Ohnesorge number the mean diameter of particles will be larger due to a higher resistance offered by surface tension forces to the liquid disintegration process.

Table.5.11. D_{32}^{*} and L* Values for a slag system with a constant (Re-458, Ek-7.8e^{-05}) and varying (Oh-0.0143, 0.0134, 0.0126)

Material	**Ohnesorge number(Oh)**	**SMD(D_{32}^{*})**	**L***
$\boldsymbol{CaO - SiO_2 - MgO - Al_2O_3}$	0.0143	0.0110	0.1944
	0.0134	0.0119	0.2056
	0.0126	0.0128	0.2241

Table.5.12. D_{32}^{*} and L* Values for an aqueous glycerol solution with a constant (Re-1312, Ek-2.72e-05) and varying (Oh-0.0085, 0.0075, 0.0068)

Material	**Ohnesorge number(Oh)**	**SMD(D_{32}^{*})**	**L***
Water + 60% glycerol	0.0085	0.0069	0.078
	0.0075	0.0073	0.09
	0.0068	0.0082	0.11

Table.5.13. D_{32}^{*} and L* Values for Ni-Nb with a constant (Re-3584, Ek-1.63e-05) and varying (Oh-0.0039, 0.0036, 0.0032)

Material	**Ohnesorge number(Oh)**	**SMD(D_{32}^{*})**	**L***
Nickel-Niobium	0.0039	0.0096	0.068
	0.0036	0.0103	0.094
	0.0032	0.0122	0.12

Obtained values demonstrate that as the Ohnesorge number decreases the ligament length increases. That is because the thin liquid film at the edge of the disk will experience a large stabilizing force due to higher surface tension forces. Due to this effect, the liquid film at the disk edge will have less energy, which makes the disintegration process less considerable. Figure 5.25, 5.26 and 5.27 shows the droplet size distribution for different Ohnesorge numbers.

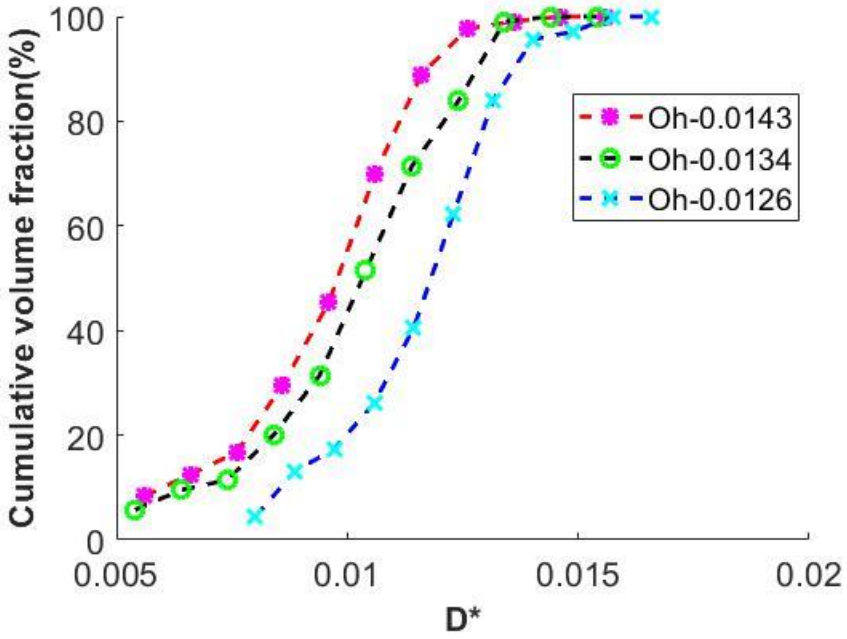

Figure 5.25. Comparison of non-dimensional droplet size distribution for slag system with a constant (Re-458, Ek-7.8e^{-05}) and varying (Oh-0.0143, 0.0134, 0.0126)

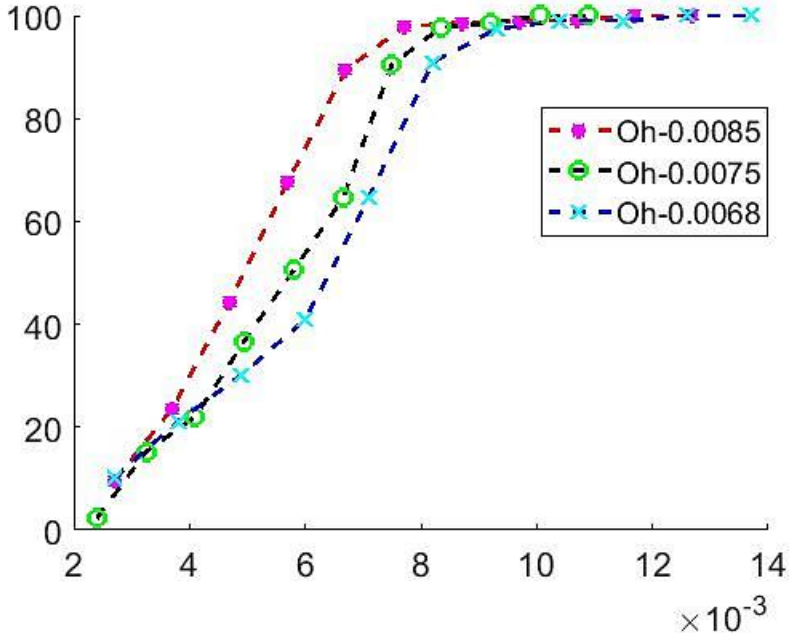

Figure 5.26. Comparison of non-dimensional droplet size distribution of aqueous glycerol solution with a constant (Re-1312 Ek-2.72e-05) and varying (Oh-0.0085, 0.0075, 0.0068)

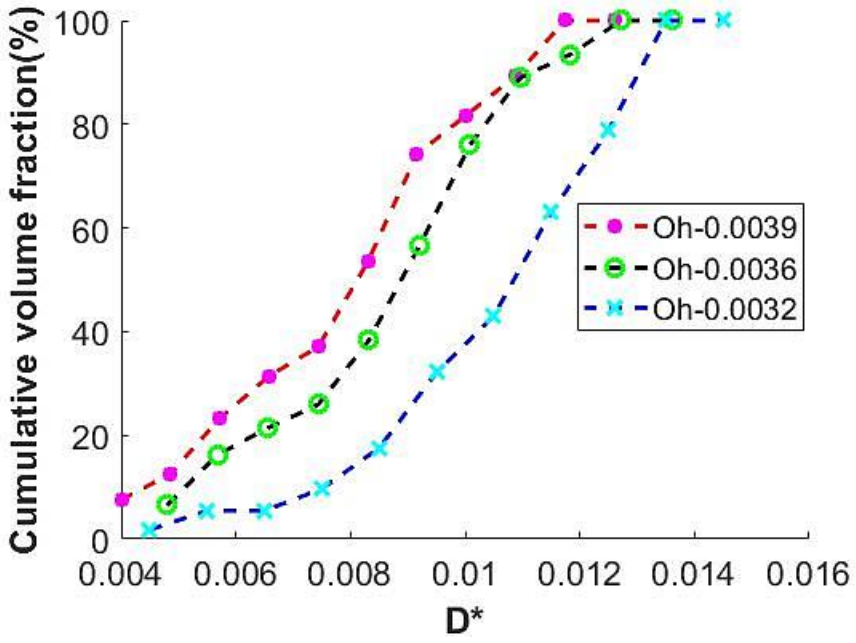

Figure 5.27. Comparison of non-dimensional droplet size distribution of Ni-Nb with a constant (Re-3584, Ek-1.63e-05) and varying (Oh-0.0039, 0.0036, 0.0032)

Results show that as the Ohnesorge number increases, the droplet size distribution curve moves left in the graph. Imposing higher Ohnesorge number produces smaller particles. Also, the variation of mean diameter values at different locations in the computational domain is represented in Tables [5.14, 5.15, and 5.16]

Table.5.14. Variation of non-dimensional SMD values across the computational domain for a slag system with a constant (Re-458, Ek-7.8e^{-05}) and varying (Oh-0.0143, 0.0134, 0.0126)

Material	**Ohnesorge number(Oh)**	**Component-I (1.29-1.44) (D^*_{32})**	**Component-II (1.44-1.59) (D^*_{32})**	**Component-III (1.59-1.74) (D^*_{32})**
$caO - SiO_2 - MgO - Al_2O_3$	0.0143	0.0095	0.0112	0.0110
	0.0134	0.0114	0.0122	0.0117
	0.0126	0.0119	0.0132	0.0131

Table.5.15. Variation of non-dimensional SMD values across the computational domain for an aqueous glycerol solution with a constant (Re-1312, Ek-2.72e-05) and varying (Oh-0.0085, 0.0075, 0.0068)

Material	**Ohnesorge number(Oh)**	**Component-I (1.2-1.4) (D_{32}^{*})**	**Component-II (1.4-1.6) (D_{32}^{*})**	**Component-III (1.6-1.8) (D_{32}^{*})**
Water + 60% glycerol	0.0085	0.0067	0.00694	0.0064
	0.0075	0.0072	0.0081	0.0073
	0.0068	0.0077	0.0083	0.0085

Table.5.16. Variation of non-dimensional SMD values across the computational domain for Ni-Nb with a constant (Re-3584, Ek-1.63e-05) and varying (Oh-0.0039, 0.0036, 0.0032)

Material	**Ohnesorge number(Oh)**	**Component-I (1.2-1.4) (D_{32}^{*})**	**Component-II (1.4-1.6) (D_{32}^{*})**	**Component-III (1.6-1.8) (D_{32}^{*})**
Nickel-Niobium	0.0039	0.00976	0.008892	0.007908
	0.0036	0.009315	0.01053	0.009896
	0.0032	0.0112	0.0124	0.0119

Total number of droplets present in various size ranges for different materials at different Ohnesorge numbers is determined. Figure 5.28, 5.29 and 5.30 shows the influence of Ohnesorge number on droplet size distribution of a slag system.

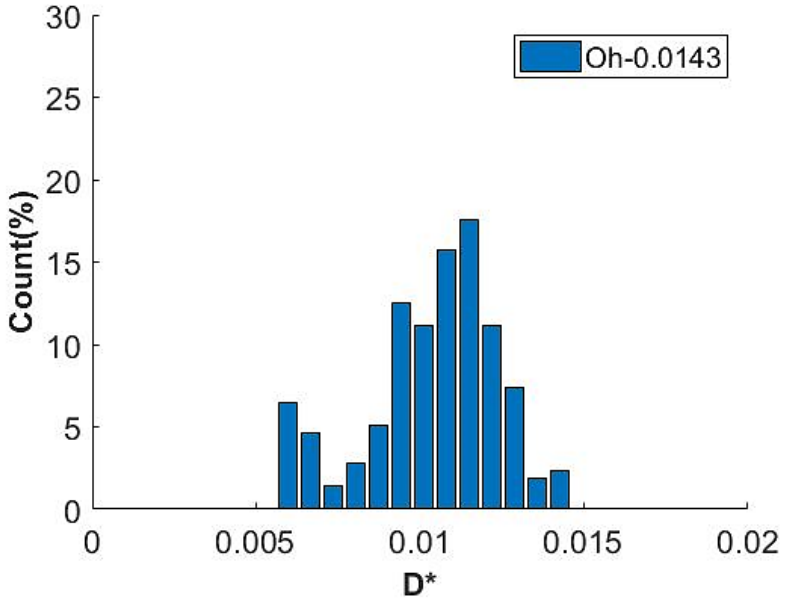

Figure 5.28. Non-dimensional droplet diameter distribution for (Ek-7.8e-05, Oh-0.0143, Re-458)

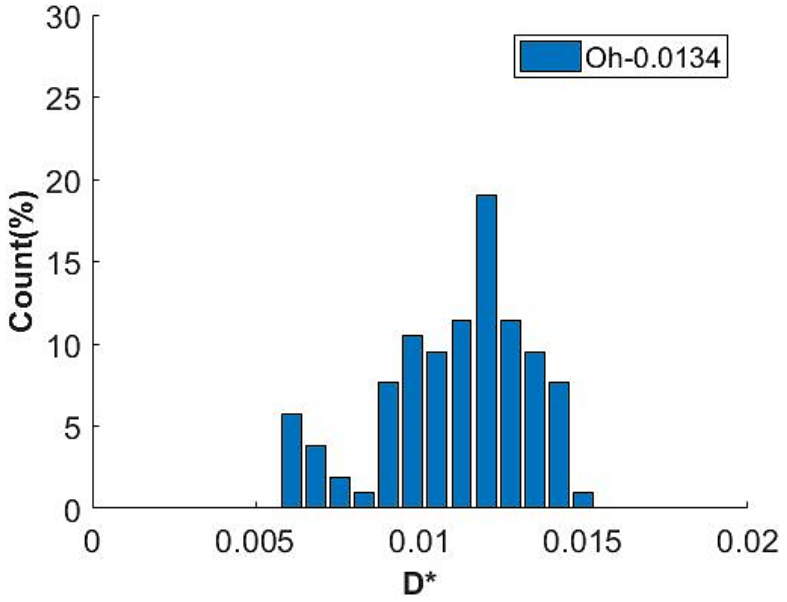

Figure 5.29. Non-dimensional droplet diameter distribution for (Ek-7.8e-05, Oh-0.0134, Re-458)

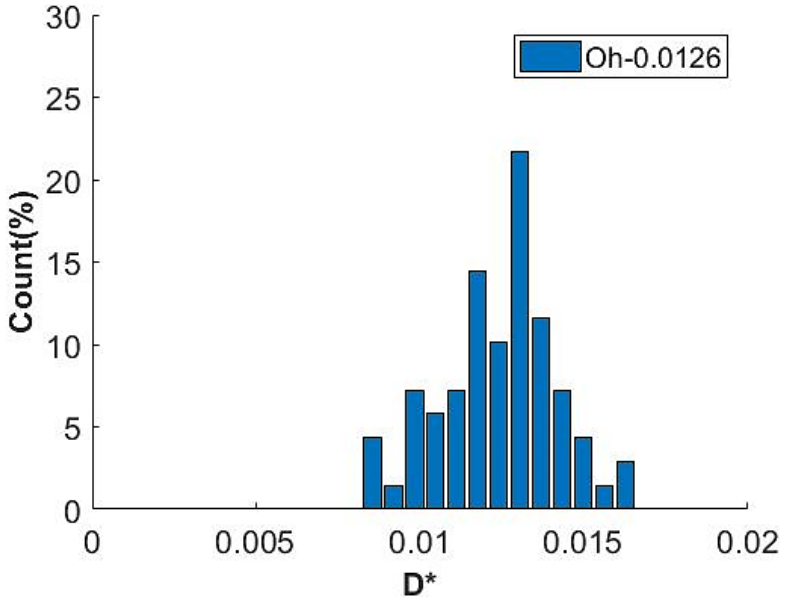

Figure 5.30. Non-dimensional droplet diameter distribution for (Ek-7.8e-05, Oh-0.0126, Re-458)

Figure 5.31, 5.32, 5.33 shows the variation of droplet size distribution for aqueous glycerol solution at different Ohnesorge numbers.

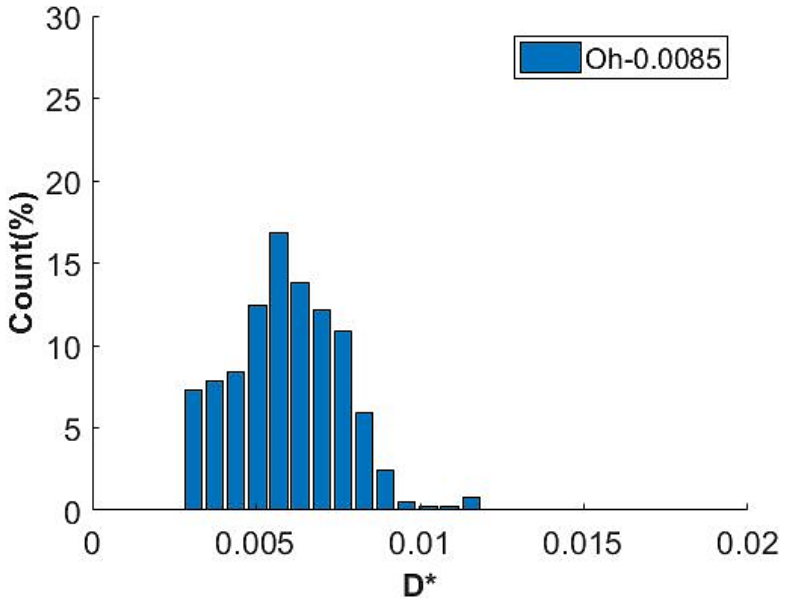

Figure 5.31. Non-dimensional droplet diameter distribution for (Ek-2.72e-05, Oh-0.0085, Re-1312)

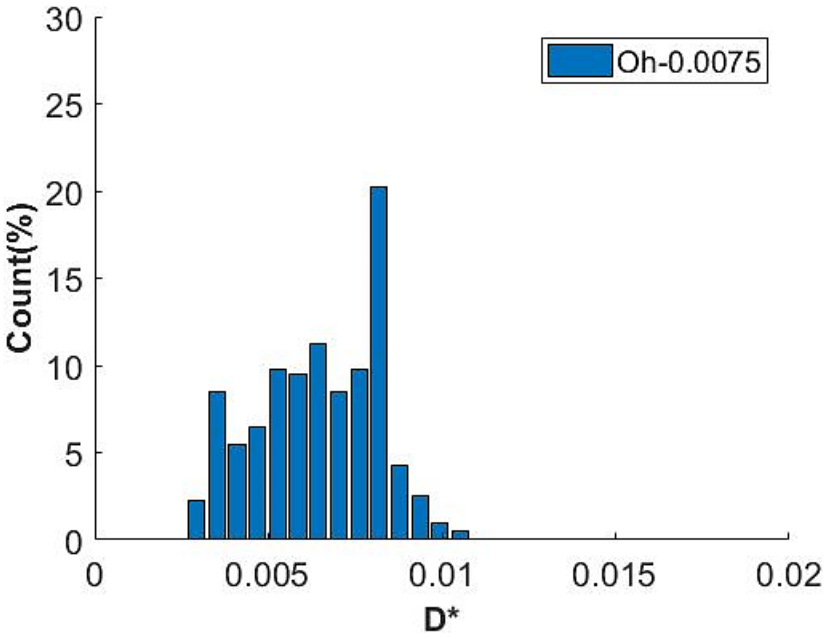

Figure 5.32. Non-dimensional droplet diameter distribution for (Ek-2.72e-05, Oh-0.0075, Re-1312)

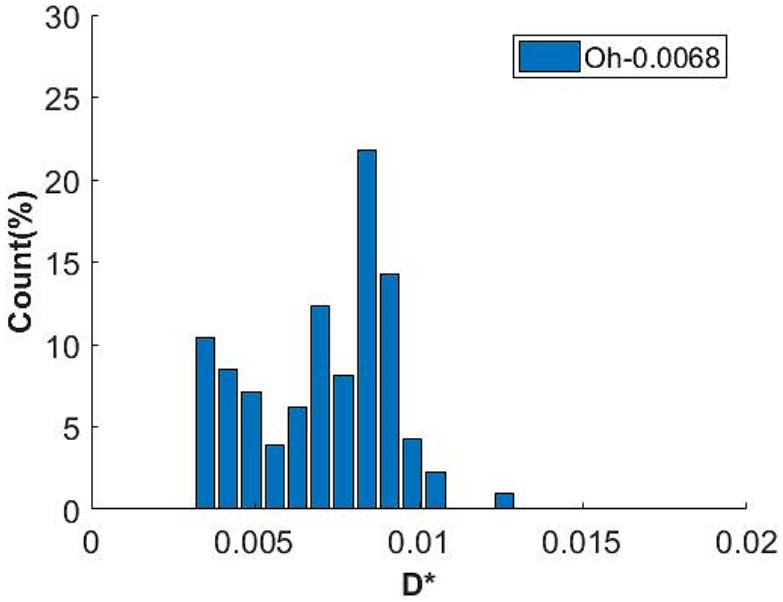

Figure 5.33. Non-dimensional droplet diameter distribution for (Ek-2.72e-05, Oh-0.0068, Re-1312)

Figure 5.34, 5.35, 5.36 demonstrates the influence of Ohnesorge number on the droplet size diameter of a Ni-Nb material.

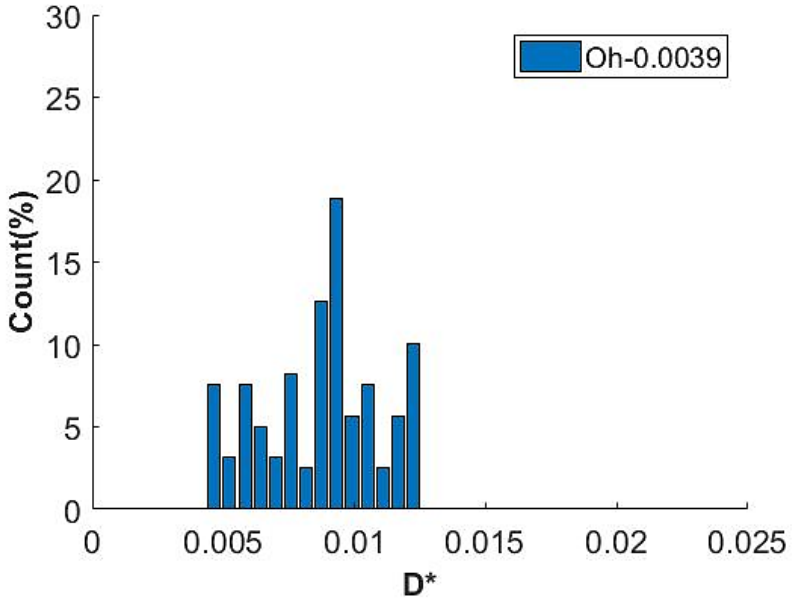

Figure 5.34. Non-dimensional droplet diameter distribution for (Ek-1.63e-05, Oh-0.0039, Re-3584)

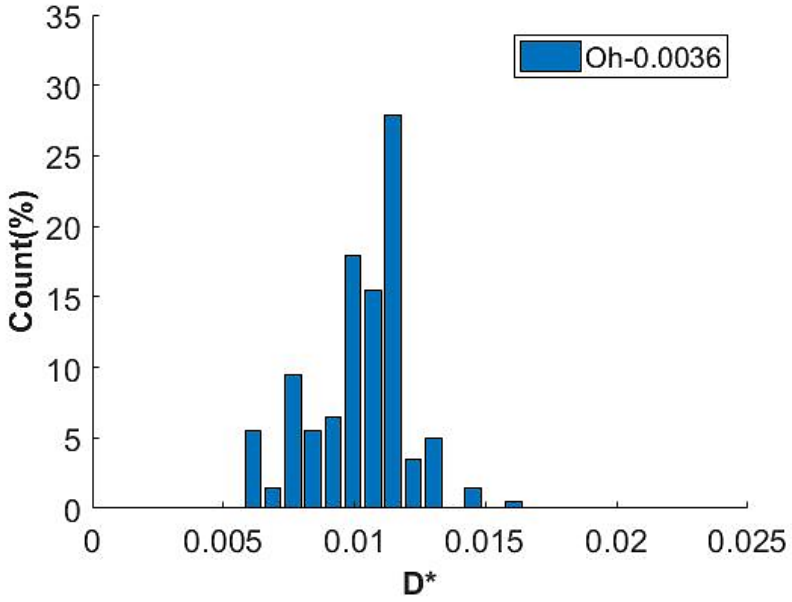

Figure 5.35. Non-dimensional droplet diameter distribution for (Ek-1.63e-05, Oh-0.0036, Re-3584)

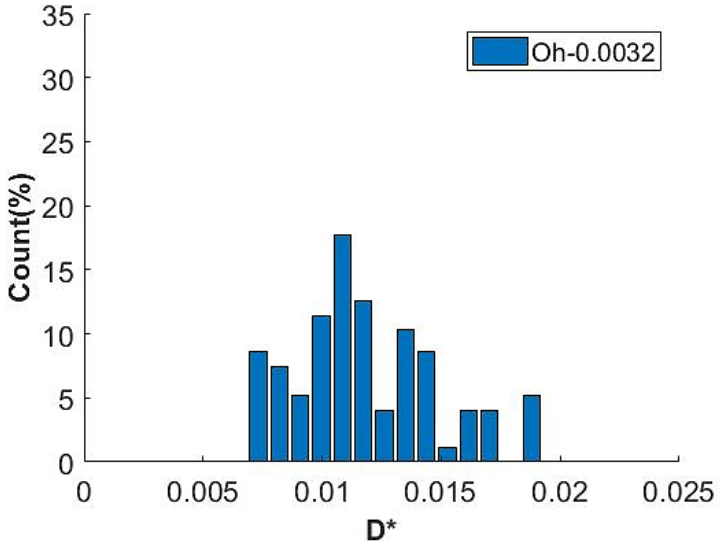

Figure 5.36. Non-dimensional droplet diameter distribution for (Ek-1.63e-05, Oh-0.0032, Re-3584)

Results demonstrates the effect of Ohnesorge number on the size of the droplets produced during centrifugal atomization process. Results indicates that production of droplets with larger diameter value increases with a decrease in Ohnesorge number. This phenomenon is due to an increase in surface tension forces, which tend to stabilize the liquid film, preventing its breakup and leading to a larger average droplet size diameter.

5.3.3. Effect of Reynolds number on different materials

The third parametric analysis is performed to study the influence of Reynolds number on various parameters in the atomization process. The input parameters for each material and the relationship between SMD and Re are shown in Table [5.17, 5.18 and 5.19]. Results demonstrate that the size of the particle becomes more significant with increasing Reynolds number. This result is consistent with the report by Xie et al. that has shown that increasing melt flow rate leads to the increased size of particles. Results show that mass flow rate has a significant influence on the film thickness at the disk edge. Decrease in mass or melt flow rate leads the unit mass liquid film at disk edge to obtain high energy from rotating disk, and, overall, the liquid film disintegration

becomes significant. Due to this effect, droplet SMD and length of the ligament decreases with a decrease in Reynolds number.

Table.5.17. D_{32}^{*} and L* Values for a slag system with a constant (Ek-7.8e-05, Oh-0.0143) and varying (Re-458, 682, 1076)

Material	Re	SMD(D_{32}^{*})	L*
$\mathbf{CaO - SiO_2 - MgO - Al_2O_3}$	458	0.0110	0.1944
	682	0.0121	0.2389
	1076	0.0130	0.2519

Table.5.18. D_{32}^{*} and L* Values for an aqueous glycerol solution with a constant (Ek-2.72e-05, Oh-0.0085) and varying (Re-1312, 1568, 2026)

Material	Re	SMD(D_{32}^{*})	L*
Water + 60% glycerol	1312	0.0069	0.078
	1568	0.0088	0.104
	2026	0.0099	0.121

Table.5.19. D_{32}^{*} and L* Values for Ni-Nb with a constant (Ek-1.63e-05, Oh-0.0039) and varying Re-3584, 7194, 9958)

Material	Re	SMD(D_{32}^{*})	L*
Nickel-Niobium	3584	0.0096	0.068
	7194	0.0126	0.1
	9958	0.0147	0.118

Results show that as Re increases the ligament length increases. Figures 5.37, 5.38 and 5.39 shows the droplet size distribution for the different Reynolds number.

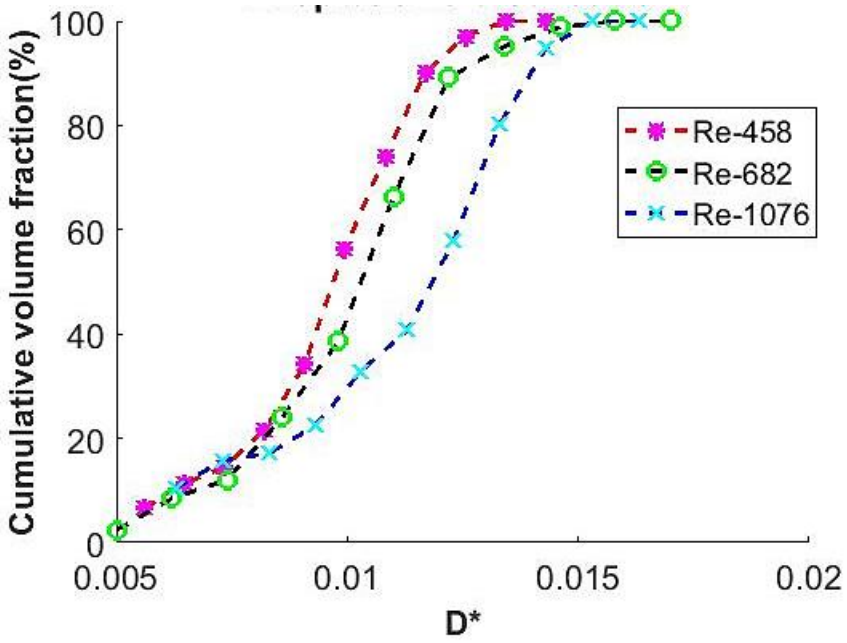

Figure 5.37. Comparison of non-dimensional droplet size distribution for slag system with a constant (Ek-7.8e-05, Oh-0.0143) and varying (Re-458, 682, 1076)

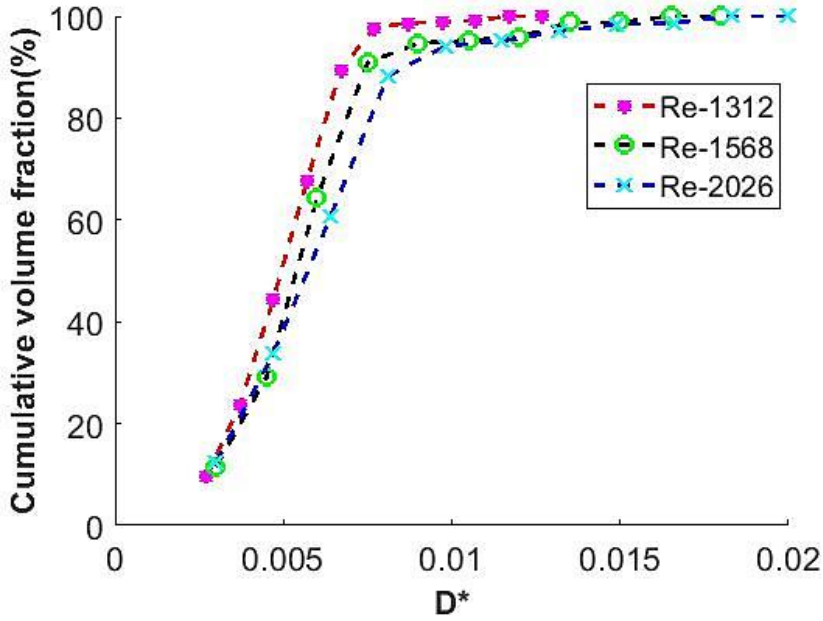

Figure 5.38. Comparison of non-dimensional droplet size distribution for an aqueous glycerol solution with a constant (Ek-2.72e-05 and Oh-0.0085) and varying (Re-1312, 1568, 2026)

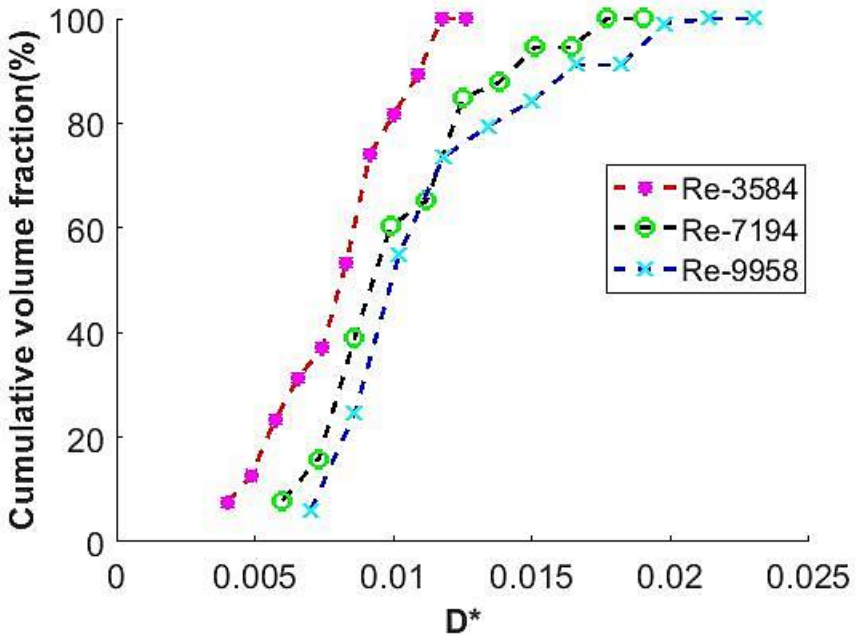

Figure 5.39. Comparison of non-dimensional droplet size distribution of Ni-Nb with a constant (Ek-1.63e-05, Oh-0.0039) and varying (Re-3584, 7194, 9958)

Results demonstrate that as Re increases, the droplet size distribution curve moves towards right in the graph. Having Lower mass or melt flow rates can produce particles with smaller diameters. In addition, SMD values for each component is calculated to analyze the variation of SMD values across the computational domain. Tables [5.20, 5.21, and 5.22] shows the variation of SMD values at different locations.

Table.5.20. Variation of non-dimensional SMD values across the computational domain for a slag system with a constant (Ek-7.8e-05, Oh-0.0143) and varying (Re-458, 682, 1076)

Material	**Re**	**Component-I (1.29-1.44) (D_{32}^*)**	**Component-II (1.44-1.59) (D_{32}^*)**	**Component-III (1.59-1.74) (D_{32}^*)**
$\boldsymbol{caO - SiO_2 - MgO - Al_2O_3}$	458	0.0095	0.0112	0.0110
	682	0.0106	0.0118	0.0120
	1076	0.0117	0.0130	0.0135

Table.5.21. Variation of non-dimensional SMD values across the computational domain for an aqueous glycerol solution with a constant (Ek-2.72e-05, Oh-0.0085) and varying (Re-1312, 1568, 2026)

Material	**Re**	**Component-I (1.2-1.4) (D_{32}^*)**	**Component-II (1.4-1.6) (D_{32}^*)**	**Component-III (1.6-1.8) (D_{32}^*)**
Water + 60% glycerol	1312	0.0067	0.00694	0.0064
	1568	0.0103	0.0078	0.0085
	2026	0.0112	0.0089	0.0098

Table.5.22. Variation of non-dimensional SMD values across the computational domain for Ni-Nb with a constant (Ek-1.63e-05, Oh-0.0039) and Varying (Re-3584, 7194, 9958)

Material	**Re**	**Component-I (1.2-1.4) (D_{32}^*)**	**Component-II (1.4-1.6) (D_{32}^*)**	**Component-III (1.6-1.8) (D_{32}^*)**
Nickel-Niobium	3584	0.00976	0.008892	0.007908
	7194	0.009848	0.011936	0.013142
	9958	0.0122	0.0143	0.0149

Further, droplet size distribution in terms of count is determined to analyze the effect of Reynolds number on the diameter of droplets produced during centrifugal atomization process. Figure 5.40, 5.41 and 5.42 shows the influence of Reynolds number on the diameter of slag system droplets.

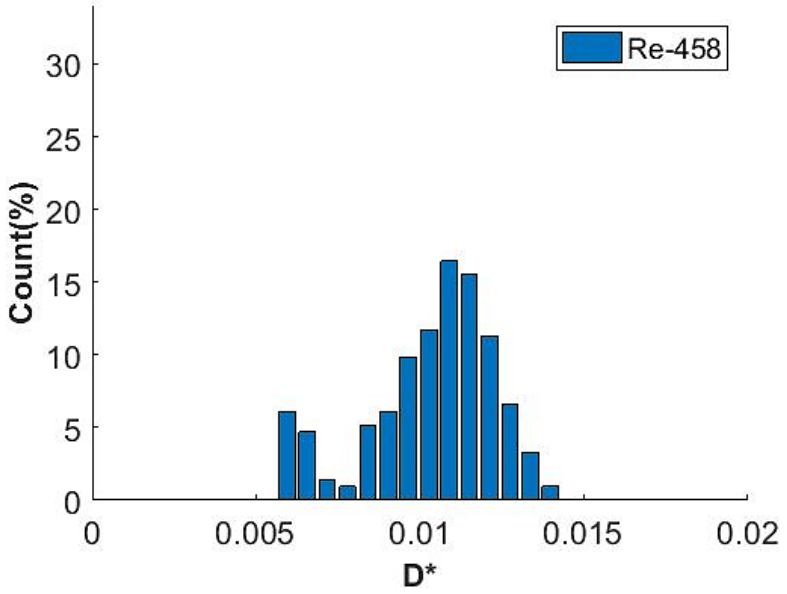

Figure 5.40. Non-dimensional droplet diameter distribution for (Ek-7.8e-05, Oh-0.0143, Re-458)

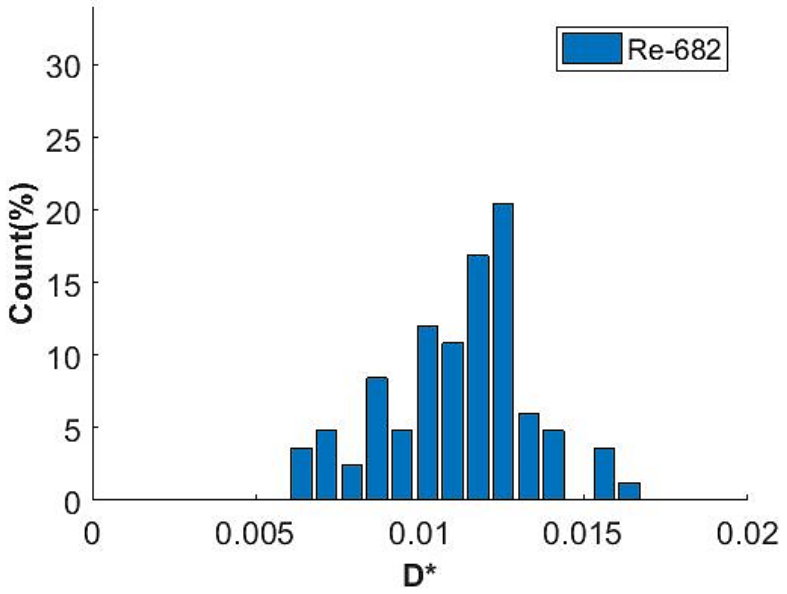

Figure 5.41. Non-dimensional droplet diameter distribution for (Ek-7.8e-05, Oh-0.0143, Re-682)

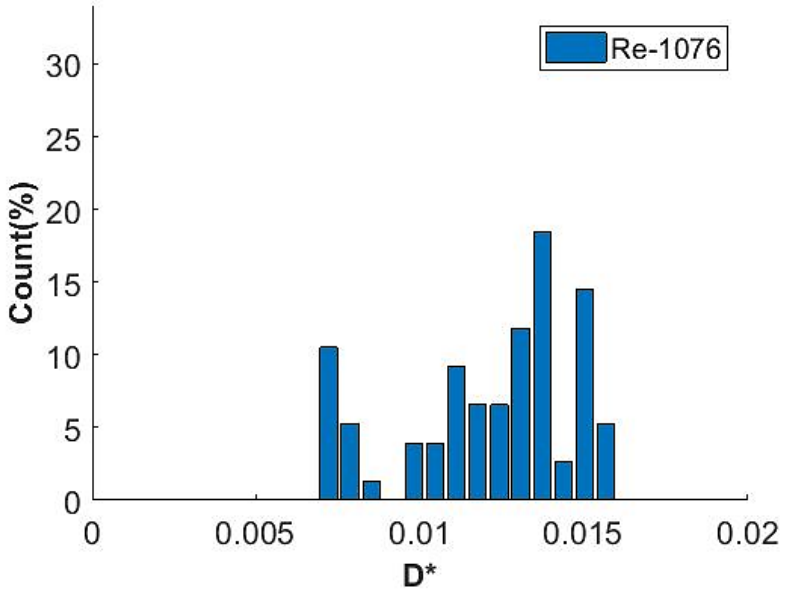

Figure 5.42. Non-dimensional droplet diameter distribution for (Ek-7.8e-05, Oh-0.0143, Re-1076)

Similarly, Figure 5.43, 5.44 and 5.45 demonstrates the influence of Reynolds number on the droplet size diameter of an aqueous glycerol material.

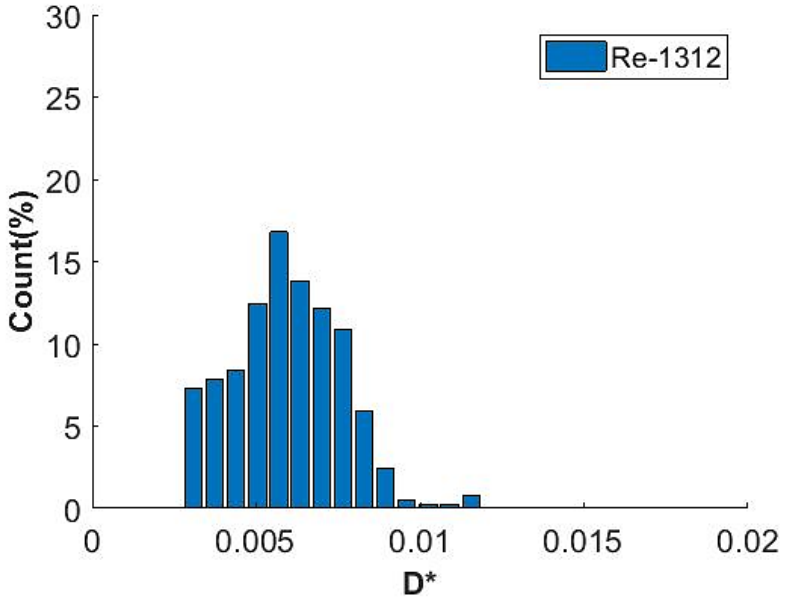

Figure 5.43. Non-dimensional droplet diameter distribution for (Ek-2.72e-05, Oh-0.0085, Re-1312)

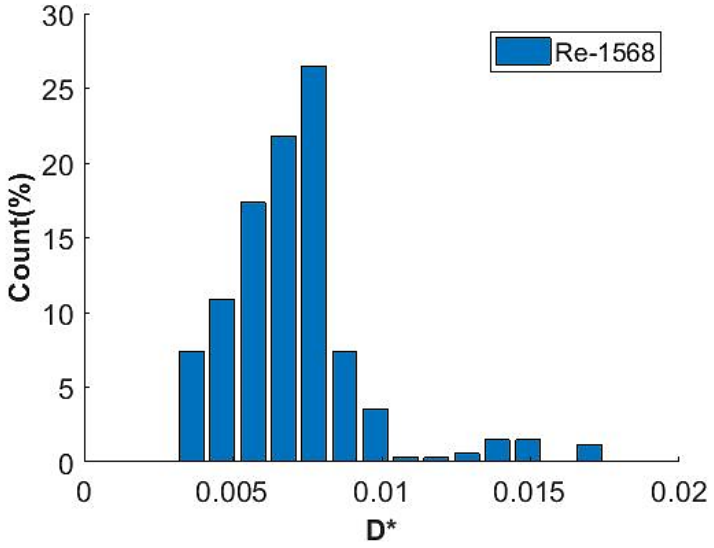

Figure 5.44. Non-dimensional droplet diameter distribution for (Ek-2.72e-05, Oh-0.0085, Re-1568)

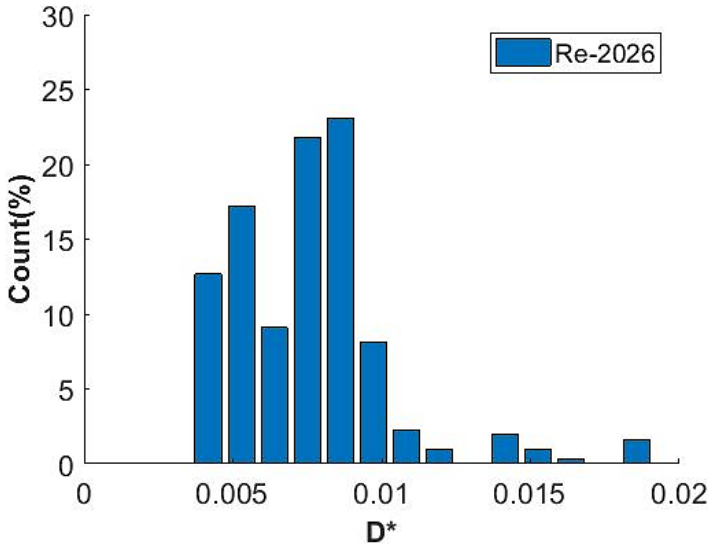

Figure 5.45. Non-dimensional droplet diameter distribution for (Ek-2.72e-05, Oh-0.0085, Re-2026)

Finally, figure 5.46, 5.47 and 5.48 shows the effect of Reynolds number on the droplet size diameter of Ni-Nb material.

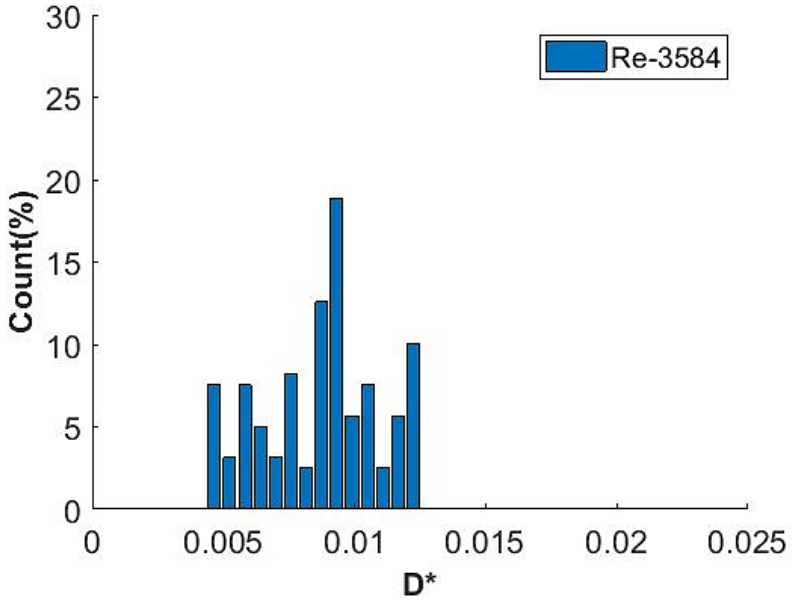

Figure 5.46. Non-dimensional droplet diameter distribution for (Ek-1.63e-05, Oh-0.0039, Re-3584)

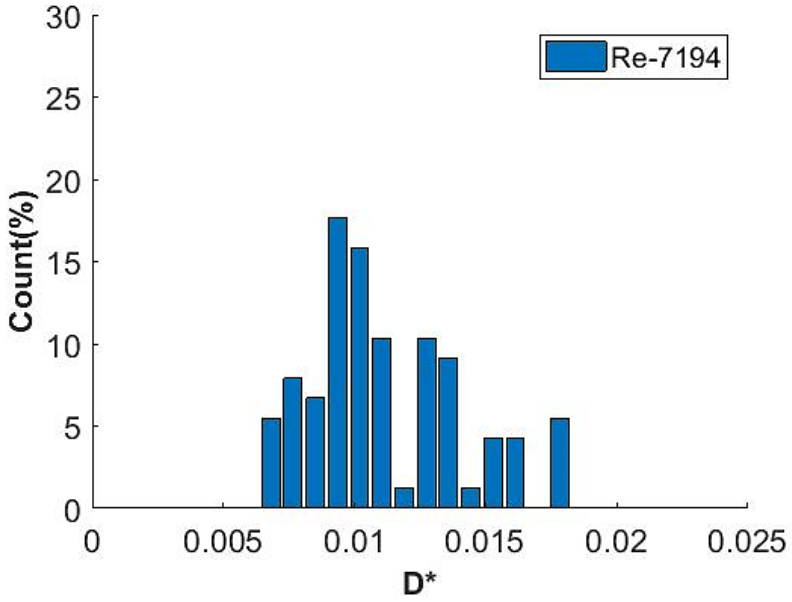

Figure 5.47. Non-dimensional droplet diameter distribution for (Ek-1.63e-05, Oh-0.0039, Re-7194)

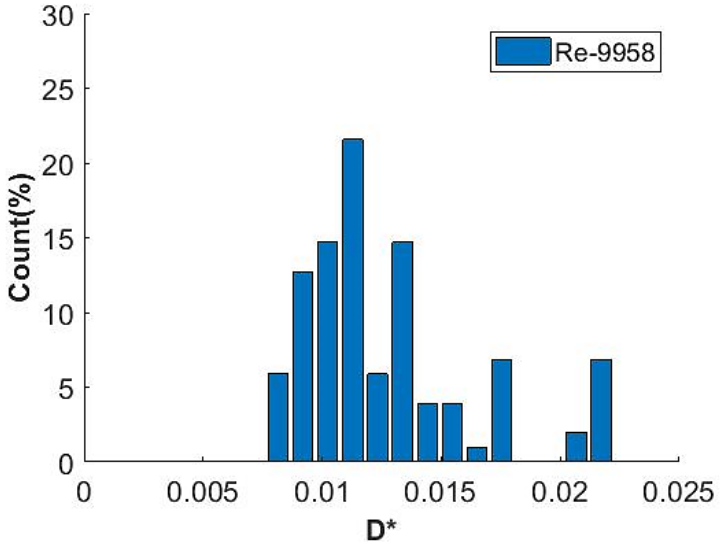

Figure 5.48. Non-dimensional droplet diameter distribution for (Ek-1.63e-05, Oh-0.0039, Re-9958)

Results demonstrates the effect of Reynolds number on the size of the droplets produced during centrifugal atomization process. Results shows that production of droplets with larger diameter value increases with an increase in Reynolds number. This phenomenon is due to an increase in mass flow rate, which makes the liquid disintegration process insignificant.

5.4. Correlations

Correlations are determined to estimate the Sauter mean diameter values for the materials: slag system, aqueous glycerol solution, and Ni-Nb binary alloy by using linear regression methodology. Equation 5.1 represents the correlation for Sauter mean diameter for a slag system.

$$\frac{d_{32}}{D} = 0.18 * Re^{0.172} * Oh^{-0.990} * Ek^{0.849} \quad (5.1)$$

Equation 5.2 represents the correlation for Sauter mean diameter for an aqueous glycerol solution.

$$\frac{d_{32}}{D} = 0.99 * Re^{0.867} * Oh^{-0.639} * Ek^{1.352} \quad (5.2)$$

Equation 5.3 shows the correlation for Sauter mean diameter for a Ni-Nb solution.

$$\frac{d_{32}}{D} = 2.957 * Re^{0.429} * Oh^{-1.276} * Ek^{1.481} \quad (5.3)$$

Similarly, correlations are determined to estimate the length of the ligament for all the materials used in numerical simulations. Equation 5.4 shows the correlation for the mean value of ligament length for a slag system.

$$\frac{L}{D} = 0.99 * Re^{0.272} * Oh^{-0.769} * Ek^{0.689} \quad (5.4)$$

Equation 5.5 represents the correlation for the mean value of ligament length for an aqueous glycerol solution.

$$\frac{L}{D} = 0.998 * Re^{1.11} * Oh^{-1.508} * Ek^{1.681} \quad (5.5)$$

Finally, equation 5.6 describes the correlation for the mean value of ligament length for a Ni-Nb solution.

$$\frac{L}{D} = 0.994 * Re^{0.574} * Oh^{-3.41} * Ek^{2.383} \quad (5.6)$$

Chapter 6
Conclusions

This study was performed to understand the behavior of droplet breakup phenomenon in centrifugal atomization process. The first part of the study computationally explored the droplet breakup phenomenon of a molten slag material. The second and third part studied the atomization of an aqueous glycerol solution and molten Ni-Nb materials.

For all materials, the effects of Ekman number, Ohnesorge number, and Reynolds number on the Sauter mean diameter were explored. Additionally, a variation of Sauter mean diameter across the computational domain and ligament length were also investigated.

The effect of Ekman number on Sauter mean diameter was explored for molten slag material at a constant Ohnesorge and Reynolds number, around Oh=0.0143, Re= 458. It was found that as Ekman number increases, Sauter mean diameter increases due to the absence of large centrifugal forces to break up thin liquid sheet. Similar behavior was observed for aqueous glycerol solution at a constant Oh=0.0085, Re=1312 and molten Ni-Nb solution at a constant Oh=0.0039, Re= 3584. Apart from Sauter mean diameter, Ligament length values were also investigated. From the analysis, it was determined that as the Ekman number increases, ligament length will become significant due to dominant viscous force effect.

Further research was performed to determine the effect of Ohnesorge number on Sauter mean diameter for molten slag material at a constant Ekman number and Reynolds number, around Ek=7.8e-05, Re=458. From this study, it was determined that Sauter mean diameter of molten metal droplets increases with a decrease in Ohnesorge number. This is due to the presence of large surface tension forces, which stabilize the thin liquid film and prevents its breakup at the edge of spinning disk. Once again, a similar pattern was observed for aqueous glycerol solutions at a

constant Ek=2.72e-05, Re= 1312 and molten Ni-Nb solution at a constant Ek=1.63e-05, Re=3584. In addition, Ohnesorge number effect on ligament length for all materials was also investigated. From the analysis, it was observed that as the Ohnesorge number decreases, ligament length increases due to a higher resistance offered by surface tension forces to the liquid disintegration process.

Finally, the effect of Reynolds number on Sauter mean diameter and ligament length was explored for all three materials. For molten slag material, the numerical simulation was performed at a constant Ohnesorge number and Ekman number, around Oh=0.0143, Ek=7.8e-05. From the results, it was determined that as the Reynolds number increases, Sauter mean diameter and ligament length values increases due to an increase in film thickness at the edge of rotating disk. An increase in film thickness leads the unit mass liquid film to obtain less disintegration energy, and, overall, the liquid film disintegration process becomes insignificant. Due to this effect, SMD and ligament length values increases with an increase in Reynolds number. Similar results were obtained for aqueous glycerol solution at a constant Oh=0.0085, Ek=2.72e-05 and molten Ni-Nb solution at a constant Oh =0.0039, Ek= 1.63e-05.

The results of the current research reveal that the multi-phase flow numerical technique is beneficial for studying the droplet breakup phenomenon in centrifugal atomization process. The VOF model of turbulent two-phase flow has a high potential for further enhancement. In particular, it is desirable to establish a mathematical model to capture the droplet breakup phenomenon in centrifugal atomization process of metal alloys. Hence, the following set of tasks are recommended for future investigations

To perform numerical study of rotating electrode atomization process, accurate solidification/melting models are required. The formulation of these models could be extended

from the modeling approaches developed by V.R. Voller [52]. A systematic analysis of this formulation would allow for coupling between VOF and enthalpy-porosity technique.

The current numerical study does not include analysis on the molten metal alloys like (Titanium alloys or Super alloys), which are very important in the additive metal manufacturing process. A detailed study on the thickness of the liquid formed at the edge of the rotating electrode for different metal alloys will be of interest in further research.

Appendix A
Validity of the choice and definition of non-dimensional numbers for the problem.

Previous literatures have determined quantities that have a significant effect on the ligament mode atomization process. Equation shows the quantities.

$$F(\omega, D, Q, \mu, \sigma, \rho) = 0 \tag{4.1}$$

These parameters are classified into three groups depending on the number of quantities and fundamental dimensions involved. ω, Q and σ are selected to make the groups independent of each other. Three non-dimensional groups are determined by combining the dependent parameters with the independent quantities. Equation shows three non-dimensional quantities.

$$F\left(\frac{\omega\rho D^2}{\mu}, \frac{\sigma D\rho}{\mu^2}, \frac{Q}{\pi\vartheta h}\right) = 0 \tag{4.2}$$

Other critical non-dimensional parameters in this problem are Length of the ligament $L^* = \frac{l}{D}$ and droplet diameter $D^* = \frac{d}{D}$. Disk diameter (D) is the characteristic length scale in this problem.

The three non-dimensional parameters represented in the equation are Ekman number, Ohnesorge number and Reynolds number. Ekman number describes the ratio of viscous forces to the Coriolis forces in a flow field. Tritton gives the expression of Ekman number as $Ek = \frac{\mu}{\omega\rho D^2}$. Next important parameter is the Ohnesorge number. This number describes relation between the viscous forces to surface tension and inertial forces and it is defined as $Oh = \frac{\mu}{\sqrt{\rho\sigma D}}$. Another significant parameter in this problem is the Reynolds number. This number describes the ratio of inertial forces to the viscous forces and it is defined as $Re = \frac{\rho u D}{\mu}$ where, u is defined as $\frac{Q}{\pi D h}$.

To analyze the effect of each non-dimensional number on the droplet diameter size and ligament length, Ekman number, Ohnesorge number and Reynolds number are varied individually by keeping the other two parameters constant. The validity of these three non-dimensional numbers are determined by performing additional numerical simulations. To validate the significance of non-dimensional numbers, Ekman number, Ohnesorge number and Reynolds number are kept constant for aqueous glycerol solution and Ni-Nb material by adjusting the rotational speed of the disk, coefficient of surface tension of the melt and volumetric flow rate at the inlet. For the next two cases, Ohnesorge number is varied by keeping Reynolds and Ekman number constant for Ni-Nb material and the obtained results for all three cases are compared with aqueous glycerol solutions to verify the validity of non-dimensional number for the problem. Figure A.1, A.2 and A.3 shows the droplet size distribution for different materials at same non-dimensional numbers.

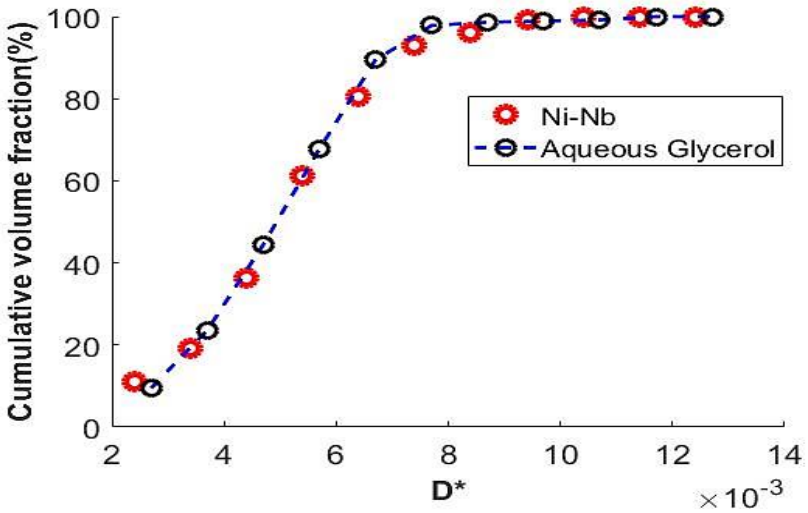

Figure A.1. Droplet size distribution for different materials at (Ek-2.72e-05, Oh-0.0085, Re-1312)

Table A.1. Significance of non-dimensional numbers on droplet size at (Ek-2.72e-05, Oh-0.0085, Re-1312)

Material	$\boldsymbol{D_{32}^{*}}$
Aqueous Glycerol	0.0069
Ni-Nb	0.00686

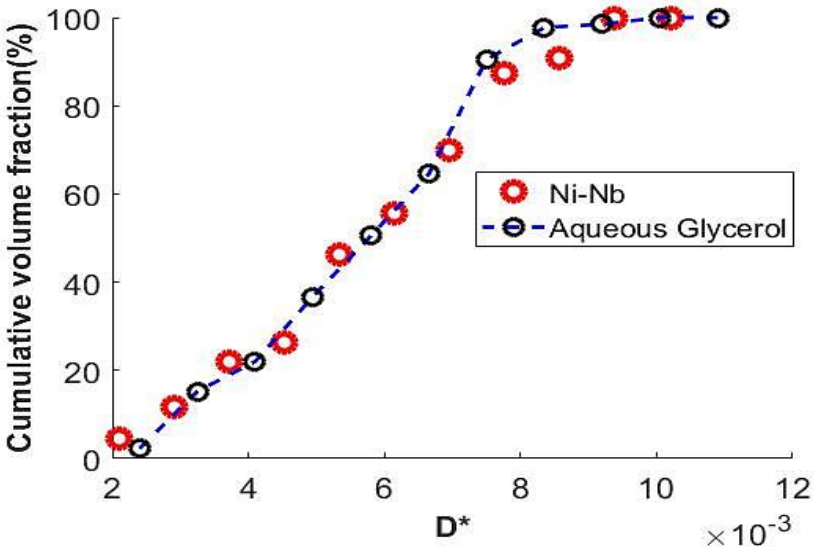

Figure.A.2: Droplet size distribution for different materials at (Ek-2.72e-05, Oh-0.0075, Re-1312)

Table A.2. Significance of non-dimensional numbers on droplet size at (Ek-2.72e-05, Oh-0.0075, Re-1312)

Material	$\boldsymbol{D_{32}^{*}}$
Aqueous Glycerol	0.0073
Ni-Nb	0.00748

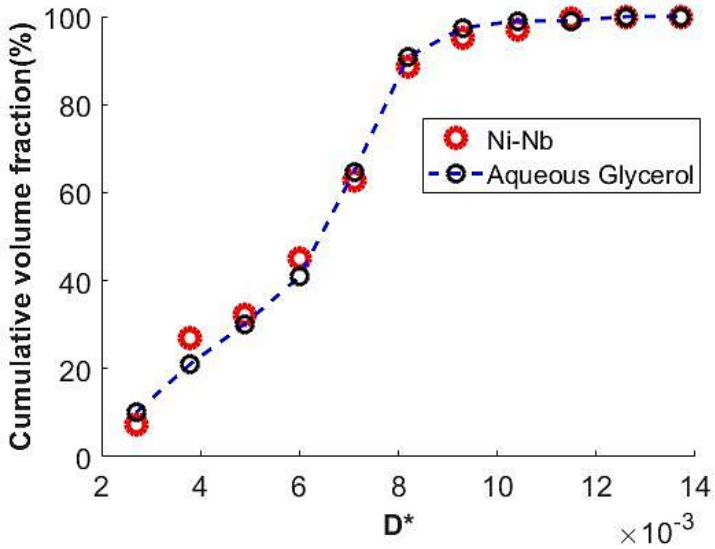

Figure.A.3: Droplet size distribution for different materials at (Ek-2.72e-05, Oh-0.0068, Re-1312)

Table A.3. Significance of non-dimensional numbers on droplet size at (Ek-2.72e-05, Oh-0.0068, Re-1312)

Material	D_{32}^{*}
Aqueous Glycerol	0.0082
Ni-Nb	0.00834

It is determined from the results that the droplet size distribution and SMD values for different materials at same non-dimensional numbers falls well on a single trend. This trend confirms that the choices of the scales and non-dimensional numbers to perform parametric analysis are appropriate for the problem.

Appendix B
Velocity distribution for different non-dimensional number combinations.

Tangential and radial velocity distribution across the computational domain follows a similar pattern for different combinations of non-dimensional numbers. Similar to Figure 5.11 and 5.12, obtained results for combinations of different non-dimensional numbers demonstrates that the effect of tangential velocities on the ligament atomization process is more significant than radial and axial velocities. Figure B.1 and B.2 shows contour plots of the non-dimensional radial and tangential velocity distribution across the computational domain for a slag material at (Ek-9.8e-05, Oh-0.0143, and Re-458). Figure B.3 and B.4 shows the non-dimensional radial and tangential velocity distribution for a slag material at (Ek-7.8e-05, Oh-0.0134, and Re-458).

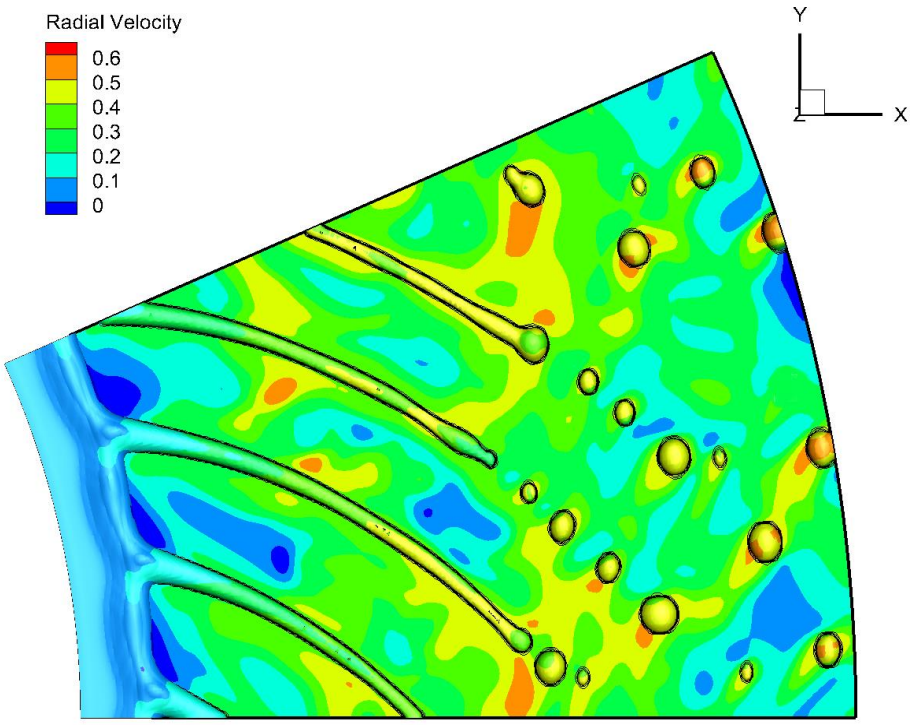

Figure.B.1. Non-dimensional radial velocity for a slag system at (Ek-9.8e-05, Oh-0.0143, and Re-458)

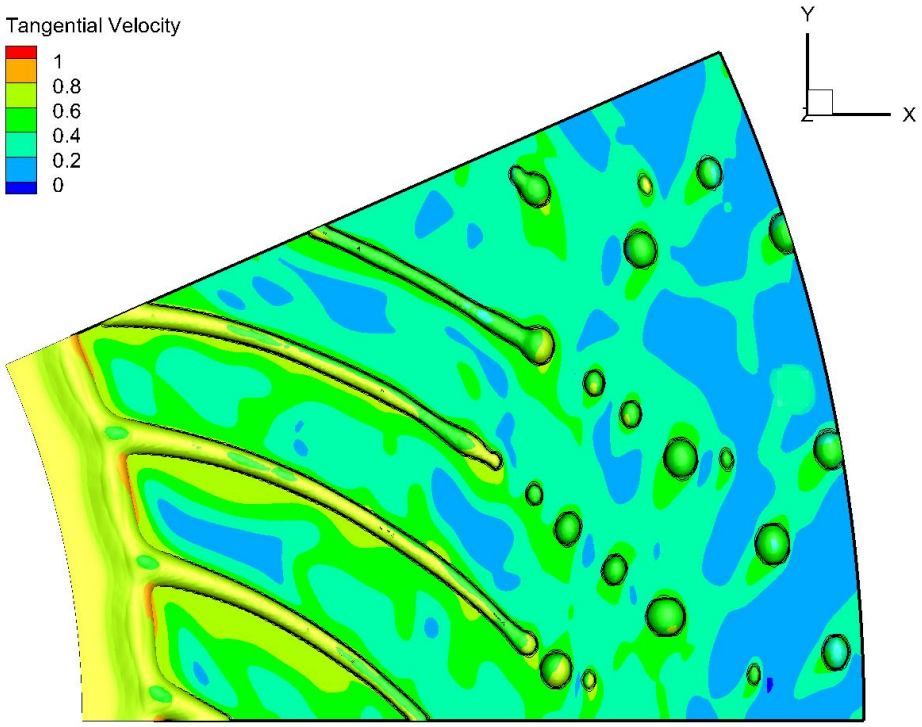

Figure.B.2. Non-dimensional tangential velocity for a slag system at (Ek-9.8e-05, Oh-0.0143, and Re-458)

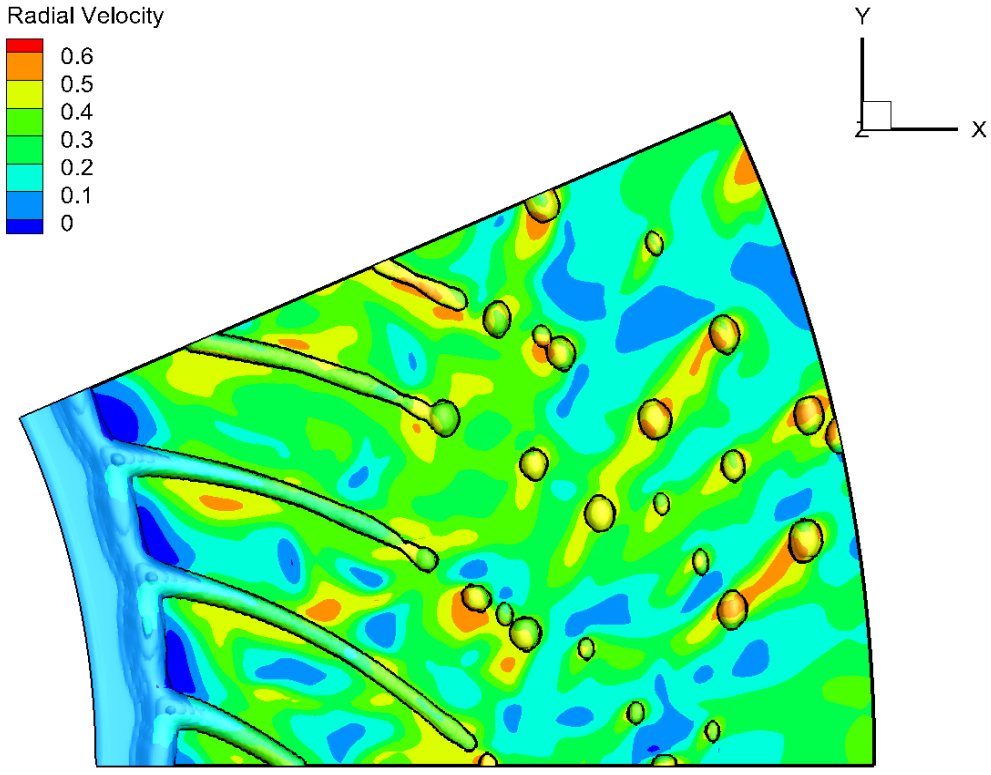

Figure.B.3.Non-dimensional radial velocity for a slag system at (Ek-7.8e-05, Oh-0.0134, and Re-458)

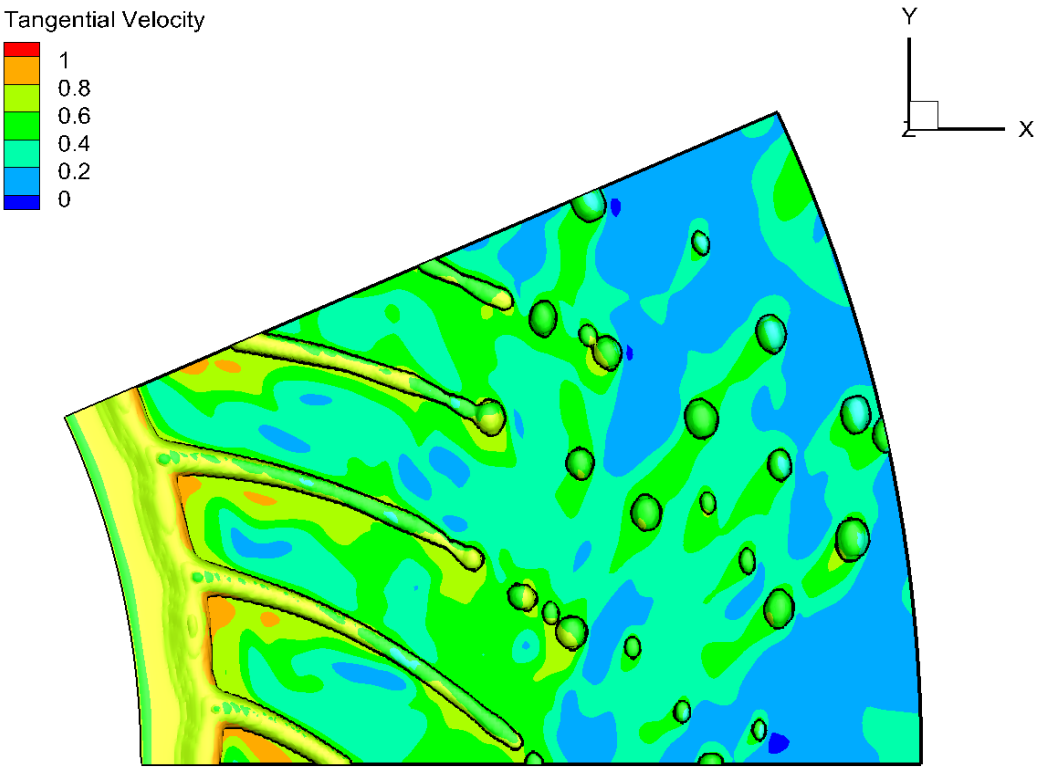

Figure.B.4. Non-dimensional tangential velocity for a slag system at (Ek-7.8e-05, Oh-0.0134, and Re-458)

References

[1] M.D.A. Lightfoot, “Fundamental Classification of Atomization Processes,” *Atomization and Sprays,* vol. 19, pp. 1065-1104, 2009.

[2] H.Liu, “Science and Engineering of Droplets,” *William Andrew Publishing,* 1999.

[3] Rayleigh, “On the Instability of Jets,” *Proc. London Mathematical Society,* vol. 10, pp. 4-13, 1879.

[4] A.H.Lefebvre, “Atomization and sprays,” *Taylor & Francis,* 1989.

[5] El-Sayed R. Negged, S. Hidaka, M.Kohno, Y. Takata, “Experimental and analytical investigation of liquid sheet breakup characteristic,” International journal of heat and fluid flow, vol. 32, pp 95-106, 2011.

[6] N. Holden, “Advances in Powder Metallurgy: Properties, Processing, and Applications.” *Woodhead Publishing Limited,* 2013.

[7] Christopher Wayne Potts,” Development of a centrifugal atomizer,” *California state university,* 2017.

[8] J. A. Tallmadge, “Chapter 1 - Powder Production by Gas and Water Atomization of Liquid Metals, in Powder Metallurgy Processing,” *Eds. Academic Press,* pp. 1–32, 1978.

[9] S. A. Bose. “Advances in particulate materials,” *Elsevier,* 1995.

[10] C.T. Wang.; S.C. Yen,” Theoretical Analysis of Film Uniformity in Spinning Processes,” *Chem. Eng. Science,* vol .50, pp. 989 – 999, 1995.

[11] A.G. Emslie, F.T. Bonner, L.G. Peck, “Flow of a viscous liquid on a rotating disk,” *J. Appl. Phys,* vol. 29, pp. 858, 1958.

[12] J.W. Rauscher, R.E. Kelly, J.D. Cole, “An asymptotic solution for the laminar flow of thin film on a *rotating* disk,” *J. Appl. Mech,* vol. 40,1973.

[13] G.I. Lepehin, G.V. Riabchuk, “Temperature Distribution in Film of Viscous Liquid with Heating on a Rotating Disk, Rheology in Processes and Apparatus of Chemical Technology,” *Works of Polytechnic Institute of Volgograd,* Volgograd, 1975.

[14] Y.Y. Zhao, A.L. Dowson, M.H. Jacobs, “Modeling of liquid flow after a hydraulic jump on a rotating disk prior to centrifugal atomization,” *Modell. Simul. Mater. Sci. Eng.* vol. 8, pp. 55, 2000.

[15] W.P. Woods, “The Hydrodynamics of Thin Liquid Films Flowing over a Rotating Disk (Ph.D. thesis),” the *University of Newcastle upon Tyne,* UK, 1995.

[16] J.R. Burns, C. Ramshaw, R.J. Jachuck, “Measurement of liquid film thickness and the determination of spin-up radius on a rotating disk using an electrical resistance technique,” *Chem. Eng. Science,* vol. 58, pp. 2245-2253, 2003.

[17] J. Rice, A. Faghri, B. Cetegen, "Analysis of a free-surface film from a controlled liquid impinging jet over a rotating disk including conjugate effects with and without evaporation," *Int. J. Heat Mass Transfer,* vol. 48, pp. 5192-5204, 2005.

[18] Y.H. Pan, P.J. Witt, B. Kuan, D.S. Xie, "Effect of flow and operating parameters on the spreading of a viscous liquid on a rotary disk," *Ninth International Conference on CFD in the Minerals and Process Industries CSIRO, Melbourne,* Australia, 2012.

[19] T.J. Bhatelia, R.P. Utikar, V.K. Pareek, M.O. Tade, "Characterizing liquid film thickness in rotary disk reactors," *Seventh International Conference on CFD in the Minerals and Process Industries CSIRO, Melbourne,* Australia, 2009.

[20] B. Champagne, R. Angers, "Size distribution of powders atomized by the rotating electrode process," *Modern Development in Powder Metallurgy,* vol. 12, pp. 83-104, 1980.

[21] Sescu, C. 2011," Experimental and Computational Study on Liquid Atomization by Slinger Injector," *The University of Toledo,* Spain.

[22] K. *Halada*, et al., "Parameters for centrifugal atomization of metal*," Metal Powder Report,* v. 45, pp. 784. 1990

[23] J.O. Hinze, H. Milborn, "Atomization of liquid by means of a rotating cup," *J. Appl. Mech.-T ASME,* vol. 17,pp .145-153, 1950.

[24] R. Fraser, N. Dombrowski, J. Routly, "The filming of liquids by spinning cups," *Chem. Eng. Science,* vol. 18, pp. 323-337, 1963

[25] A. Kayano, T. Kamiya, "Calculation of the mean size of droplets purged from the rotating disk," *The Proceedings of The1st International Conference on Liquid Atomization and Spray Systems,* Tokyo, pp. 133, 1978

[26] A.R.Frost, "Rotary atomization in the ligament formation mode," *J. Agr. Eng. Research,* vol. 26, pp. 63-78, 1981

[27] P. Eisenklam, "On ligament formation from spinning disks and cups," *Chem. Eng. Science.* vol. 19, pp. 693-694, 1964.

[28] Y. Kawase, A. De," Ligament-type disintegration of non-Newtonian fluid in spinning disk atomization," *Journal of Non-Newtonian Fluid Mechanics,* vol. 10, pp. 367–371, 1982

[29] M. Ahmed, M. Abou Al-Sood, A. Ali, "A one dimensional model of viscous liquid jets breakup," *J. Fluids Eng.-Trans. ASME,* vol. 133, p. 114501, 2011

[30] M. Ahmed, M. Youssef, M. Abou Al-Sood, "Two-dimensional modeling of viscous liquid jet breakup," *Acta. Mech,* vol. 224, pp. 499-512, 2013**.**

[31] Pei-Kuan Wu, Kevin A. Kirkendall, Raymond P. Fuller, and Abdollah S. Nejad. "Breakup Processes of Liquid Jets in Subsonic Crossflows," *Journal of Propulsion and Power,* vol. 13, pp. 64-73, 1997

[32] J.C. Lasheras, E.J. Hopfinger, "Liquid jet instability and atomization in a coaxial gas stream," *Ann. Rev. Fluid Mech,* vol. 32, pp. 275-308, 2000

[33] J. Shinjo, S. Matsuyama, Y. Mizobuchi, et al., "A numerical study on ligament disintegration mechanism by propagative capillary waves," *Atomization,* vol. 18, pp. 36-43, 2009

[34] J. Shinjo, A. Umemura, "Simulation of liquid jet primary breakup: dynamics of ligament and droplet formation," *Int. J. Multiphase. Flow,* vol. 36, pp. 513-532, 2010.

[35] D. J. Benson. "Computational methods in Lagrangian and Eulerian hydrocodes," *Computer Methods in Applied Mechanics and Engineering,* vol. 99, pp. 235-394, 1992.

[36] J. H. Ferziger and M. Peric. "Computational Methods for Fluid Dynamics", *Springer*, 2002.

[37] S. Mckee, M. F. Tome, V. G. Ferreira, J. A. Cuminato, A. Castelo, F. S. Sousa, et al." The MAC method", *Computers & Fluids,* vol. 37, pp. 907-930, 2008

[38] S. Osher and R. P. Fedkiw. "Level Set Methods: An Overview and Some Recent Results," *Journal of Computational Physics,* vol. 169, pp. 463-502, 2001.

[39] R. P. Fedkiw, T. Aslam, B. Merriman, and S. Osher. "A non-oscillatory Eulerian approach to interfaces in multi-material flows (the ghost fluid method)," *Journal of Computational Physics,* vol. 152, pp. 457-492, 1999.

[40] C. W. Hirt and B. D. Nichols. "Volume of Fluid (VOF) Method for the Dynamics of Free Boundaries," *Journal of Computational Physics,* vol. 39, pp. 201-225, 1981.

[41] M. Sussman and E. G. Puckett. "A coupled level set and volume-of-fluid method for computing 3D and axisymmetric incompressible two-phase flows", *Journal of Computational Physics,* vol.162, pp. 301-337, 2000.

[42] M. Sussman, K. M. Smith, M. Y. Hussaini, M. Ohta, and R. Zhi-Wei. "A sharp interface method for incompressible two-phase flows," *Journal of Computational Physics,* vol. 221, pp. 469-505, 2007.

[43] J. U. Brackbill, D. B. Kothe, and C. Zemach. "A Continuum Method for Modeling Surface-Tension," *Journal of Computational Physics,* vol. 100, pp. 335-354, 1992.

[44] G. *Cerne,* S. Petelin, and I. Tiselj. "Coupling of the interface tracking and the two-fluid models for the simulation of incompressible two-phase flow," *Journal of Computational Physics,* vol. 171, pp. 776-804, 2001.

[45] ANSYS Fluent User's Guide.

[46] S. Harmand, J. Pelle, S.Poncet, I.V.Shevchuk. "Review of fluid flow and convective heat transfer with in rotating disk cavities with impinging jet", *International Journal of Thermal Sciences,* vol.67, pp.1-30, 2013.

[47] H. K. Versteeg and W. Malalasekera. "An introduction to Computational Fluid Dynamics: The finite volume method," *Second edition, Pearson Education Ltd., England,* New York, 2007

[48] S. B. Pope. "Turbulent Flows," *Cambridge University Press, Cambridge;* New York, 2000

[49] P. A. Libby. "An Introduction to Turbulence," *Taylor & Francis,* New York, 1996.

[50] F. M. White. “Fluid Mechanics,” *Fourth Edition, McGraw-Hill*, 1999.

[51] Dongxiang Wang, Xiang Ling, HaoPeng,”Simulation of ligament mode breakup of molten slag by spinning disk in the dry granulation process,” *Applied Thermal Engineering*, vol. 84, pp. 437-447, 2015.

[52] V. R. Voller, “Modeling Solidification Processes. Technical report, Mathematical Modeling of Metals Processing Operations Conference”, *American Metallurgical Society,* Palm Desert, CA, 1987.

Vita

Sai Saran Kandati attended SSNCE and obtained Bachelor of Engineering degree in mechanical engineering in 2015.In pursuit of Master of Science degree in mechanical engineering, Sai studied computational methodologies and algorithms to solve fluid dynamic problems under Dr.Dimitris E.Nikitopoulos at LSU. He is expected to graduate in December 2018.